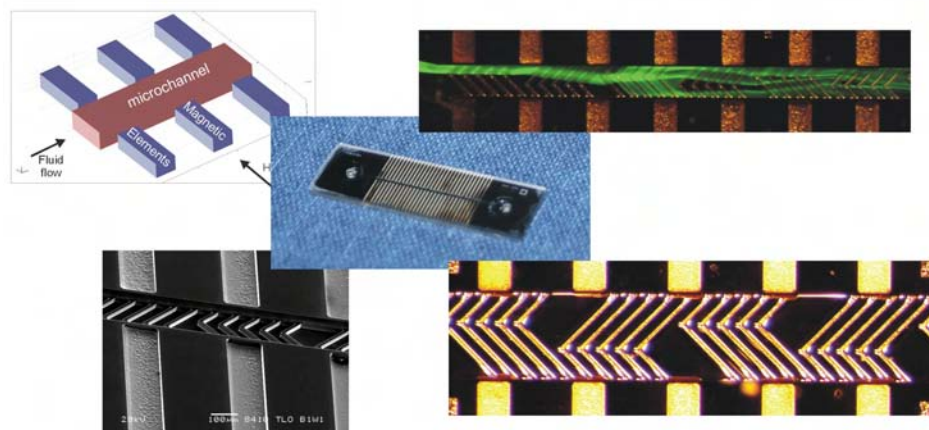M. Sc. E. Thesis

Integrated Microfluidic Mixer and Magnetic Bead Separator

Torsten Lund-Olesen (s973550)

Supervisors: Mikkel Fougt Hansen and Henrik Bruus

MIC – Department of Micro and Nanotechnology
Technical University of Denmark

1 March, 2005

Abstract

Prior to analysis of biological samples, purification is often necessary. Separation in a microsystem using magnetic beads has a great potential for this purpose.

In this thesis the modeling, fabrication, characterization, and comparison of two types of passive magnetic separators is presented.

Both types of systems have a microfluidic channel with magnetic elements, consisting of the soft magnetic material permalloy, placed outside the channel on both sides. The difference between the two types of systems is that a microfluidic staggered herringbone mixer is integrated in the channel in one design whereas the microfluidic channel is a simple rectangular channel in the other design.

The working principle is that the magnetic elements are magnetized by an external homogenous magnetic field, thus creating gradients in the magnetic field inside the microfluidic channels. Magnetic beads flowing in the channel will experience a force towards the sidewalls where the magnetic field is large. The idea of integrating a microfluidic mixer is that the beads in the middle of the channel, where only small or no magnetic force acts on the beads, are pushed out towards the sidewalls where they will be caught by the large magnetic forces.

The fluid flow in the channel has been simulated, and the influence of different parameters has been evaluated to maximize the effectiveness of the mixer.

A fabrication scheme for the chosen systems has been designed, and the fabrication of systems successfully demonstrated.

A set-up for doing the experiments has been fabricated, and a method for quantitative determinations of very small amounts of magnetic beads has been devised.

The fabricated systems have been characterized qualitatively for several flow rates, and have proven to be very effective magnetic separators.

Quantitative characterization of the systems has been performed, and it has been shown that the mixer makes the release of the magnetic beads more reliable.

Both qualitative and quantitative experiments have shown that the mixer increases capturing efficiency.

Resumé

Forud for en analyse af en biologisk prøve, er det ofte nødvendigt at gennemføre et oprensningstrin. Til dette er separation i mikrosystemer, ved hjælp af små magnetiske kugler, en metode med et stort potentiale.

I denne afhandling præsenteres modellering, fabrikation, karakterisering og sammenligning af to typer passive magnetiske separatorer.

Begge systemtyper består af mikrofluide kanaler med magnetiske elementer, bestående af det bløde magnetiske materiale permalloy, placeret udenfor kanalen på begge sider. Forskellen på de to systemtyper er at der i mikrokanalen på den ene systemtype befinder sig en integeret mikrofluid mixer. I den anden systemtype er den mikrofluide kanal en simpel rektangulær kanal.

Princippet bag systemerne er, at et eksternt homogent magnetfelt magnetiserer de magnetiske elementer, der derved laver gradienter i magnetfeltet inde i den mikrofluide kanal. De magnetiske kugler inde i kanalen vil derved blive udsat for en kraft ud mod siden af kanalen, hvor det magnetiske felt er stort. Ideen bag at integrere systemet med en mikrofluid mixer er, at de kugler der befinder sig i midten af kanalen, hvor kun små eller slet ingen magnetiske kræfter er til stede, vil blive skubbet ud mod siderne, hvor de vil blive indfanget af de store magnetiske kræfter.

Væskeflowet i kanalerne er blevet simuleret, og forskellige parametres indflydelse på mixer effektiviteten er blevet undersøgt, med henblik på optimering af mixeren.

En fremstillingsmetode til de valgte systemer er blevet udviklet, og fremstillingen af systemer demonstreret.

En forsøgsopstilling er blevet lavet, og en metode til kvantitative bestemmelser af meget små mængder af magnetiske kugler er blevet udviklet.

De fremstillede systemer er blevet karakteriserede kvalitativt for flere forskellige væskeflows, og det har vist at de er meget effektive magnetiske separatorer.

Kvantitativ karakterisering af systemerne er blevet udført, og det er blevet vist at mixeren gør frigørelsen af de magnetiske kugler mere kontrolleret.

Både kvalitativ og kvantitativ karakterisering af systemerne har vist at den integrerede mixer gør indfangningen af de magnetiske kugler mere effektiv.

Preface

This thesis is a part of the requirements for obtaining the Master of Science in Engineering degree (M. Sc. E.) at the Technical University of Denmark (DTU). The work performed in the project counts for 50 ECTS points. The project has been carried out at the Institute for Micro and Nanotechnology (MIC), within the Magnetic Microelectromechanical Systems group (MagMEMS) and the Microfluidic Theory and Simulation group (MIFTS). The project was performed under supervision of the main supervisor associate professor Mikkel F. Hansen, head of the MagMEMS group, and cosupervisor professor Henrik Bruus, head of Bio/Chemical Microsystems Section.

The title of the project is "Integrated microfluidic mixer and magnetic bead trap" and the project was started 1 February 2004 and the thesis handed in on 1 March 2005.

I would like to thank both Mikkel F. Hansen and Henrik Bruus for their guidance and participation in this project. They have complemented each other very well. Mikkel's door has always been open if I wanted to discuss progress or problems in the project with him, and he has been a great help in all aspects of the project. Henrik Bruus has been great in guiding me through the microfluidic theory, and on several occasions he has helped set things into perspective, so the right goals were pursued. Together Mikkel F. Hansen and Henrik Bruus have been able to keep me focused on the main goals of the project, like producing good scientific results, writing a good thesis, and keeping the time frame. They have also kept me from spending too much time on side affairs that, though they might be very interesting, were of less importance to the project.

I would also like to say special thanks to Ph. D. student Kristian Smistrup. During the entire project we have had many hours of discussions. Some more serious than others. He has also helped me with many aspects of the theory, and generally he has been great company.

Associate professor Peter Torben Tang is acknowledged for his guidance with the electroplating processes, and especially for the hours spent with me in front of the SEM at IPL.

I would also like to thank Ph. D. student Lauritz Højgaard Olesen. Whenever I have had a problem with FEMLAB he has been very eager to help. He has also helped me understand some of the theory behind the simulations.

Finally I would like to thank the staff from DANCHIP, who has helped me with the fabrication of my systems and generally everybody at MIC, who have made my time here a great pleasure.

Torsten Lund-Olesen
MIC – Institute of Micro and Nanotechnology
Technical University of Denmark
1 March, 2005

Contents

List of Figures

List of Tables

List of symbols

Symbol	Description	Unit
t	Time	s
L	Length	m
D	Diffusion coefficient	$m^2\ s^{-1}$
ρ	Mass density	$kg\ m^{-3}$
ρ^{el}	Charge density	$C\ m^{-3}$
$\mathbf{v}$	Velocity vector	$m\ s^{-1}$
v	Velocity	$m\ s^{-1}$
μ_0	Vacuum permeability	$N\ A^{-2}$
μ_r	Relative permeability	
χ	Magnetic susceptibility	
$\mathbf{B}$	Magnetic flux density	T
$\mathbf{H}$	Magnetic field strength	$A\ m^{-1}$
$\mathbf{M}$	Magnetization	$A\ m^{-1}$
$\mathbf{m}$	Magnetic moment	$A\ m^2$
$\mathbf{A}$	Magnetic vector potential	T m
φ_m	Magnetic scalar potential	A
$\mathbf{J}$	Total current density	$A\ m^{-2}$
$\mathbf{J}^f$	Free current density	$A\ m^{-2}$
$\mathbf{J}^b$	Bound current density	$A\ m^{-2}$
$\mathbf{f}$	Body force density	$N\ m^{-3}$
$\mathbf{g}$	Acceleration of gravity	$m\ s^2$
p	Pressure	$N\ m^{-2}$
η	Dynamic viscosity	$kg\ m^{-1}\ s^{-1}$
$\boldsymbol{\sigma}$	Cauchy stress tensor	$N\ m^{-2}$
N_d	Demagnetization tensor	
Q	Volumetric flow rate	$m^3\ s^{-1}$

Chapter 1

Introduction

The aim of this project is to design and fabricate a micro system that is able to catch and subsequently release magnetic beads. This is called a magnetic separator (or magnetic particle/bead separator). In the following I will explain what this can be used for, and why this is an interesting system. I will also present the system I have fabricated and the ideas behind the design. In the last sections an overview of the project and an overview of this thesis is presented.

1.1   Magnetic separation and magnetic beads

Magnetic beads have many different applications and one of them is bioseparation. In the classical example (see Fig. 1.1) a sample containing biological material with antigens and beads coated with the matching antibodies are mixed together in a test-tube [17]. The test-tube is then placed near a strong permanent magnet. This makes the beads migrate towards the magnet. When all magnetic beads are trapped by the magnet, the test-tube is emptied and the magnet is removed. The test tube is filled with a rinsing buffer and the beads are mixed into the liquid. The beads can then again be caught with a magnet and this step can be repeated a number of times, thus cleaning the sample for everything except the magnetic beads with the desired biological material attached.

Another method for doing a separation like this could be to have the antibodies attached to a stationary surface. The difference between these two methods is that the beads can be mixed homogenously with the sample, which means that the beads will always be close to the targets you are trying to catch. This reduces the incubation time drastically since the distance the molecules have to move by diffusion is shortened by orders of magnitude. The diffusion time can be approximated by the time it takes for one molecule to diffuse the distance required, and this can be estimated by the Einstein relation [47]

$$t_{ij} \approx \frac{L^2}{D_{ij}} \tag{1.1}$$

where L is the diffusion length, and D_{ij} is the diffusion coefficient of species i in a mixture of species i and j. It is seen that a change in diffusion length can give large changes
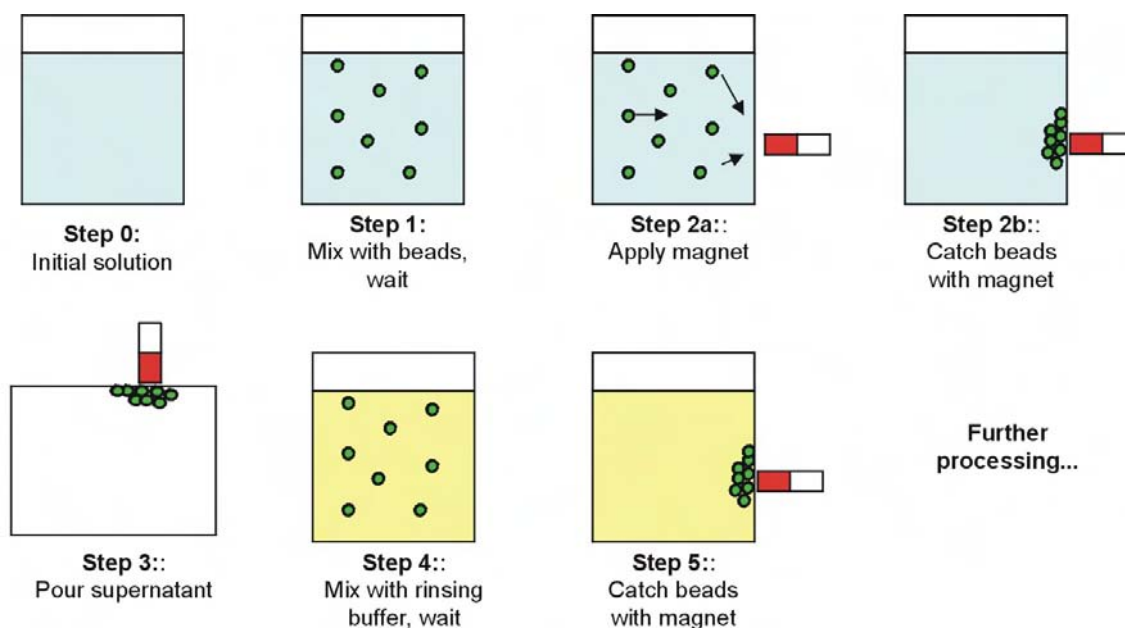
Figure 1.1: *A schematic overview of magnetic separation. The rinsing from step 3 to step 5 can be performed several times to achieve the desired amount of cleaning [1].*

in diffusion time. For large biological molecules the diffusion constant is very small and this often gives incubation times of hours or days. A reduction of the incubation time is therefore desirable.

Another good thing about using magnetic beads is that the magnetic response of biological material is much weaker than the response of the magnetic beads. It is hence possible after incubation to capture and manipulate the beads with the attached target without affecting the rest of the biological material. This is an advantage compared to electrophoresis where all biological entities are affected.

In this M. Sc. project the aim has been to fabricate a microsystem for magnetic separation. This is because the method mentioned above might work, but it is not optimal for fast handling of small volumes of sample. Furthermore the idea in this project is to combine a passive magnetic separator with a microfluidic mixer to increase capturing efficiency. At the same time an additional functionality is introduced to the system, which is mixing of fluid. The basic design and the ideas behind it will be explained in Sec. 1.2.

To demonstrate that the idea of integrating the magnetic separator with a microfluidic mixer works, devices with and without mixers have been fabricated, followed by characterization and comparison of the capturing efficiency and other characteristics of the systems.

This is supplemented by theoretical investigation of the magnetic and the fluidic parts of the system, to better understand the working principle of the systems, and to optimize different parameters.

1.2   Basic design of magnetic separator

The magnetic separator design chosen in this project is a passive separator. I wanted an effective magnetic separator which should be simple to fabricate. Furthermore it should have the potential for being integrated with many other functionalities in a microfluidic network.

In Fig. 1.2 a schematic drawing of the magnetic separator is shown. The working principle of the magnetic separator is similar to the system presented in [17]. Magnetic elements are magnetized by an external magnetic field and introduces magnetic gradients in the channel, thus capturing the magnetic beads. In this design it has been chosen to place the magnetic elements along the side of the channel and not in contact with it. This enables me to fabricate long elements that are easy to magnetize. That the elements are not in contact with the channel gives a number of advantages. One of them is that the Beads do not come in direct contact with the beads. Even at low remanent magnetization the magnetic force on beads in direct contact with the magnetic elements is considerable, and this can make it difficult to release the beads. This should make it easier to release the beads after removal of the magnetic field. It also prevents the material of magnetic elements from being dissolved or in any other way interacting with the sample flowing through the channel. It has also been chosen to fabricate the magnetic elements of permalloy which is easily magnetizable and has a low remanent magnetization [11].
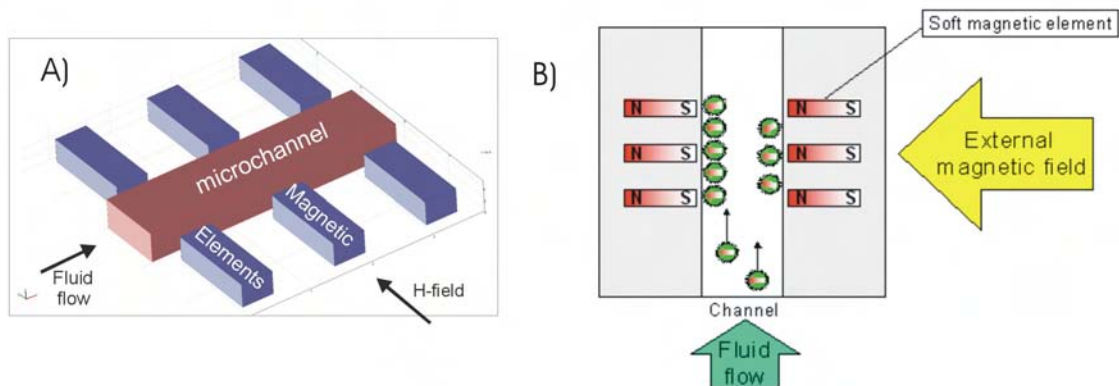
Figure 1.2: *A) A 3D schematic illustration of the basic passive magnetic separator fabricated in this project. B) A 2D schematic drawing of the passive magnetic separator with magnetic beads caught in the channel [1].*

There is also a problem with this design. In the middle of the channel no or very small magnetic forces on the magnetic beads are present. It was therefore decided to combine the magnetic separator with a microfluidic mixer. This should improve the effectiveness of the magnetic separator because all the beads are forced close to the sides of the channel where the beads are trapped by the large magnetic gradients. The extra functionality a microfluidic mixer introduces can also find use in the systems in the long term. By pumping a solution of functionalized beads into the system through one inlet and sample

through another, this will enable the mixing of sample and beads to be carried out in the microfluidic system. The time limiting factor in the incubation time is diffusion. Since the beads and the targets are forced close together, shortening diffusion time drastically, this should give much shorter incubation times as a consequence. Examples of two different passive microfluidic mixers are shown in Fig. 1.3. In the systems in this project the staggered herringbone mixer has been used.
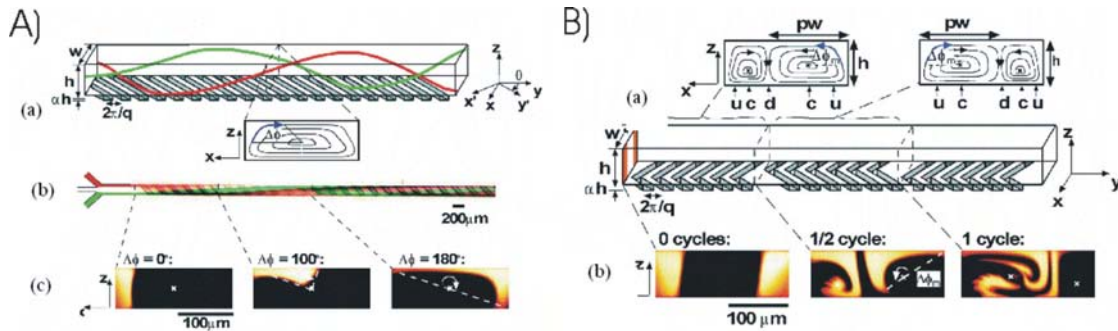
Figure 1.3: *Two different kinds of mixers A) A diagonal mixer (DM). (a) A schematic diagram of channel with ridges and the 3D twisting flow. (b) Optical micrograph showing a top view of a red stream and a green stream flowing on either side of a clear stream. (c) Fluorescent confocal micrographs of vertical cross sections. B) A staggered herringbone mixer (SHM). (a) Schematic diagram of one-and-a-half cycles of the SHM. A mixing cycle is composed of two sequential regions of ridges; the direction of asymmetry of the herringbones switches with respect to the centerline of the channel from one region to the next. The streamlines of the flow in the cross section are shown schematically above the channel. (b) Confocal micrographs of vertical cross sections of channel. Two streams of fluorescent solution were injected on either side of a stream of clear solution. Both figures from [45].*

1.3   Project goals and challenges

The main goals of this project are the following.
- Theoretical investigation of magnetic and fluidic aspects of the system
- Fabricate magnetic separators with and without integrated microfluidic mixer
- Perform experiments to show the fabricated systems work
- Compare capturing efficiency and other characteristics of systems with and without integrated microfluidic mixer
- The previous work done on microsystems for magnetic separation has almost only been proof of concept. A goal is to characterize the systems thoroughly, keeping track on bead concentrations, sample volumes, flow rates etc.

To achieve these goals many challenges have to be addressed. Some of these are:
- A fabrication sequence and masks for the fabrication have to be designed

- Critical steps in the fabrication have to be identified and solutions found.
- A set-up for experiments has to be fabricated and characterized, including development of chipholder, and detection and minimization of problems with the set-up
- A method for quantitative measurements of very small amounts of magnetic beads has to be found

1.4 Overview of the project

I started the project in February 2004, and the first months of the project were used to understand the theory behind the microfluidic mixer and the passive magnetic separator. This meant understanding the basics of fluid dynamics and magnetostatics, and performing simulations in FEMLAB to get a feeling for the influence of different parameters on the characteristics of the system. Since my background is in chemistry I had to start from scratch with the theory behind both fluid dynamics and magnetostatics.

I started out with the fluidic part since Mikkel F. Hansen was on leave the first 3 months of the project. This work was supervised by Henrik Bruus. The simulations were to be performed in FEMLAB. Performing simulations on the fluid flow turned out to be a problem, since the version of FEMLAB available at that time (FEMLAB2.3a) could not perform the 3D simulations I tried to set up. A later version FEMLAB3.0a solved some of the problems, and it is even better with the latest version FEMLAB3.1 After the return from leave of Mikkel F. Hansen, work on the magnetic part of the system commenced. Shortly thereafter it was decided to start on the fabrication of the actual systems, to be sure there would be time to fabricate systems, and also to do a thorough characterization of them.

Two different fabrication sequences were tested. One based on SU8 processing and the other based on silicon processing. The fabrication sequence based on silicon processing turned out to be the most promising and hence this was the fabrication sequence chosen. Work on this fabrication sequence was continued, to detect critical steps in the fabrication sequence and to see if changes in the mask design could relieve some of the problems.

The first mask I worked with was designed for a three week course by Kristian Smistrup to test the fabrication sequence. This mask did not include microfluidic mixers, so the fabrication sequence was modified to include an extra mask. New masks for the process sequence were designed using L-edit 11.13. While I waited for the new masks I continued working with the old mask to get more experience with especially electroplating of magnetic elements and bonding of a lid to the wafer. At the end of August I received the new masks and at the same time I managed to fabricate some working microsystems using the old mask. It was decided to go straight to the fabrication using the new masks instead of doing experiments with the fabricated systems. This was because the most important aspect of this project was to fabricate working systems with and without microfluidic mixer that could be compared directly. This meant that the systems had to be alike (except for the mixer of course) and preferably also from the same wafer.

In the end of September I started having working systems, and work on the experiments started. At the same time fabrication and improvement of chip-holders and set-up

commenced. In October I started doing some measurements on the properties of the magnetic parts of the system, and in November and December the experiments used for characterization of the systems were performed. At the same time I was working on a way to do quantitative measurements on very small amounts of magnetic beads. Two different methods seemed possible. Either counting the magnetic beads using a special glass plate and a microscope or using a vibrating sample Magnetometer (VSM) to measure the magnetic moment of a sample of beads. The method I started working on was using the VSM. It turned out being possible to do it this way though not particularly easy.

After new year a little time was spent working on the fluidic simulations again, and the remaining time of the project was spent writing this thesis.

1.5   Overview of thesis

Chapter 1 - Introduction

In this chapter I have presented the basic idea behind the magnetic separations. I have also explained the design I use, and what I want to accomplish in the project.

Chapter 2 - Background

The background of this project. An overview of the properties of magnetic beads is given, together with an overview of research areas in which they are used. This is followed by an overview of magnetic separations and a thorough review of the work done on micro scale magnetic separation systems. A review of the literature on microfluidic mixers using grooves or ridges is given in the last part of the chapter.

Chapter 3 - Microfluidics theory

In this chapter the theory behind microfluidics is explained. Concepts and parameters are presented, together with their relevance for the system.

Chapter 4 - Mixing in microchannels

This chapter is about the microfluidic simulations and experiments performed. I start by giving a simplified model for the working principle of the microfluidic mixers used. Then the parameters defining the mixers are presented together with the parameters chosen for evaluation of mixer performance. In the next section some of the simulations are presented. The simulations are used to establish some guidelines for designing the mixers. The results from the simulation together with information from the literature is used to decide on a mixer and its parameters. In the end of the chapter the microfluidic experiments are presented, and compared to simulations.

Chapter 5 - Magnetic field from soft magnetic elements

In this chapter the theory behind the magnetic parts of the system is explained. The theory of magnetostatics is applied to the systems and the equation needed to be solved

is deduced. The influence of magnetic fields on different kinds of materials is presented (especially for ferromagnetic materials), and it is discussed what this means for the choice of magnetic material. The last subject presented is the effect of geometry on the magnetic properties of objects.

Chapter 6 - Design of fabrication masks

This chapter is about the design of the fabrication masks. I present the design and discuss the relevance of the test structures added to the design.

Chapter 7 - Fabrication of systems

This is the chapter about the fabrication of the systems. I start by giving a short outline of the fabrication sequence. This is followed by a more thorough explanation of each step, together with schematic pictures to enhance the understanding of the processes. In the last part of the chapter the problems and solutions to critical steps in the fabrication are presented.

Chapter 8 - Characterization of systems

In this chapter the experiments performed are presented. In the first part of this chapter the measured properties of the fabricated systems are presented. In the next part of the chapter the set-up is presented. This includes chipholders, electromagnet, and sample introduction system.

The rest of the chapter is dedicated to the experiments. I start by presenting the method developed for quantifying the experiments. This is followed by the actual experiments of capturing and releasing beads, and the characterization of the systems based on these experiments. The characterization of the systems is both qualitative and quantitative. A short description of some initial biological experiments performed is also given.

Chapter 10 - Conclusion

Final conclusions.

Chapter 9 - Outlook

What future work can be done based on this project, and what is the most important?

Chapter 2

Background

In this chapter the background for this project is presented.

First I will write about magnetic beads. What are they, and what can they be used for? Then I will focus on magnetic separation and especially on magnetic separation in microsystems. A thorough review on work performed in this research area will be given, to provide a background knowledge of possibilities and challenges. This is followed by a discussion of the most important points.

Then I will switch to microfluidic mixers. Explain why they are interesting and the types of mixers chosen for investigation in this project. An overview is given of the work performed on this kind of microfluidic mixers. Based on this the choice of mixers for further investigation is motivated.

2.1 Magnetic beads

Magnetic beads and particles are commercially available from companies like Dynal and Bangs Laboratories [2]. They are small spheres with sizes from the nanometer range to the micrometer range (around 50 nm to 10 μm). They consist of a magnetic material and for beads in the micrometer range this is usually embedded in a polymer. The beads can be coated with different kinds of probe molecules including biocompatible molecules (e.g., antibodies, DNA, RNA,....) that will specifically target certain biological entities.

The beads can have different properties. Some have a hysteretic ferromagnetic response which means that the magnetization, when measuring a hysteresis curve, has a remanence when the external magnetic field is turned off. This is not the case for beads with superparamagnetic response, that demagnetize when the external field is turned off. In Fig. 2.1 hysteresis curves for beads with the two different kinds of magnetic response can be seen. The properties of magnetic beads can be used in many different applications.

Magnetic beads and nanoparticles are used in a number of research areas including therapeutic drug, gene and radionuclide delivery, radio frequency methods for the catabolism of tumors via hyperthermia, contrast enhancement agents for magnetic resonance imaging (MRI), and magnetic separation. For a review see Ref. [38].

In most of these research areas one of the properties being used is that a magnetic
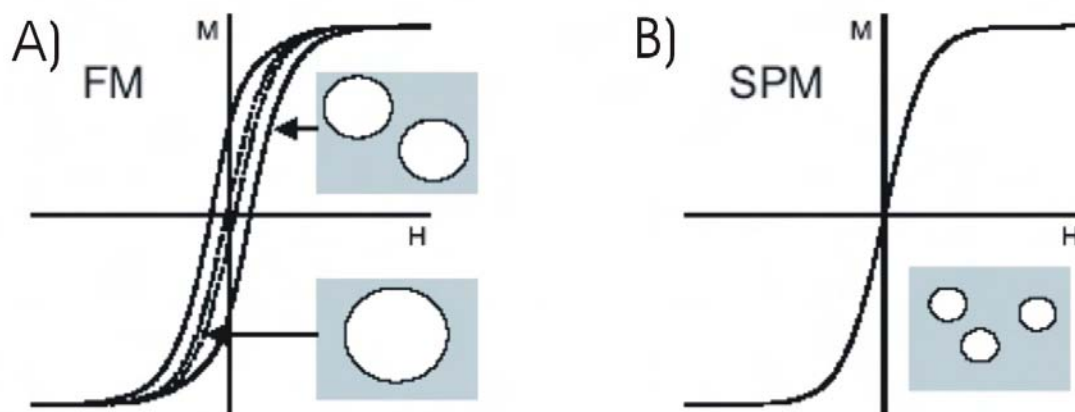
Figure 2.1: *A) Hysteresis curves for ferromagnetic beads. B) Hysteresis curve for super-paramagnetic beads. Both graphs are from [38].*

bead, with a magnetic susceptibility larger than that of its surroundings, in a spatially varying magnetic field will feel a force towards the region of higher magnetic field.

For drug, gene, and radionuclide delivery this property is used to target the beads at a specific place in the body. The beads are used as carriers for the species that are wanted introduced at a specific point in the body. The beads are then forced to concentrate at a specific region, and this is often done by placing a permanent magnet in vicinity of the area where the beads are wanted. Then the species is activated or released. The advantage of this is that smaller amounts of drugs can be used, because they are concentrated at the point where they are wanted instead of all over the body. This reduces side effects drastically and also increases the efficiency of the drugs.

Catabolism of tumors via hyperthermia uses the same method to target the magnetic beads to the site of a tumor. Then large AC magnetic fields are applied, and this makes the beads heat up. If the heat development is large enough it will kill the tumor cells. The trick is to maintain a temperature high enough and long enough to kill the tumor cells (at least $42\,^\circ\text{C}$ for around 30 min) without doing significant harm to the surrounding tissue.

MRI contrast enhancement agents using magnetic beads are commercially available. The beads affect the measurements of changes in the magnetization of the protons from ^{1}H in a magnetic field. The different types of tissue take up the beads with different speed. This then makes the measurements different for different kinds of tissue.

Magnetic separation is the research area in which I am working. In biochemistry samples containing species other than the desired are often encountered. Biochemists have to be able to isolate the desired parts of the sample, and one way to do this is by magnetic separation. In short the desired species is tagged with magnetic beads that are captured and separated from the rest of the sample. This can be done both in large scale and micro scale. The method could also be a way to separate chemical species from each other, not just biological molecules. In the next section magnetic separation will be

explained in more detail.

Another research area is one in which the beads are used as markers [19]. Usually fluorescent markers are used, but this means that the detection usually has to be performed in expensive machines with fluorescence filters. Also the sensitivity is of an order that usually requires an amplification of, e.g., the DNA material. With magnetic beads as markers the detection is magnetic. This means that detectors can be made in which detection results in a simple electrical signal from a magnetic sensor and hence an expensive optical detector is not necessary. Also the sensitivity can be pushed down to the limit of single beads which means that DNA amplification may be avoided.

As can be seen the research areas in which magnetic beads are being used are very diverse, and in this section only a few are mentioned.

2.2 Review of literature on magnetic separation

As explained in Chap. 1 biological separation using magnetic beads can be performed in test-tubes. This method is simple but has several drawbacks. Compared to microsystems it uses considerable amounts of sample. In microsystems it is also possible to perform faster separations [20] and to integrate the systems with other functionalities like mixing, polymerase chain reaction (PCR), and capture and detection of the separated species. In the other extreme when compared to systems of larger dimensions, the handling capability per time is much smaller for the test-tube method. A way to perform magnetic separation in systems of varying size can be as follows:

The first few steps are the same as the simple test-tube method, but after the beads and the sample are mixed and reaction has occurred, the sample is forced to flow through a channel in which magnetic field gradients are present. This will make the beads migrate towards areas of larger magnetic field, and if the forces acting on the beads are large enough, the beads will be captured while the rest of the sample flows through the channel. After all unwanted elements are flushed out of the channel the magnetic field is removed, and the beads are released.

The above mentioned magnetic separation sequence is only one way to do magnetic separation though. Many things can be varied. For example the order in which the different steps are carried out can be changed (e.g., mixing the sample and the beads in the channel, or eluding the captured parts before releasing the beads). Also one or more species that are to be removed from the sample can be captured. This means that the species caught on the beads is discarded whereas the rest of the sample is used.

In the following I will give a few examples of magnetic separation in larger systems and then give a thorough review of research within the area of microsystems for magnetic separation. This should give the reader an idea of the range of designs and applications possible, but also an idea of what has been done and not done so far. I will finish this part with a summary of the most important characteristics of the different kinds of systems, and also of the kind of research performed and what could be future goals.

2.2.1   Larger magnetic separation systems

In systems from millimeters and up, the conventional way to do the separation used to be forcing the sample through a pipe with a matrix of loosely packed steel wool or beads in an external magnetic field (see Fig. 2.2) [38]. This method is called High Gradient Magnetic Separation (HGMS) and it can give problems with magnetic beads sticking to the matrix [38]. Another design in which the magnetic beads do not flow through a matrix is a quadrupole magnetic flow sorter [38, 35]. This method can be applied for continuous separation (also called flow sorting) of beads from a sample. The principle is shown in Fig. 2.2. Flow sorting was also performed in a system similar to designs applicable in microsystems (see Fig. 2.3) [22]. The system is used to measure magnetic susceptibilities of beads.

For even larger systems in pipes with diameters of several cm, solenoid magnets of superconductors have been used [23]. An example of this is seen in Fig. 2.2.
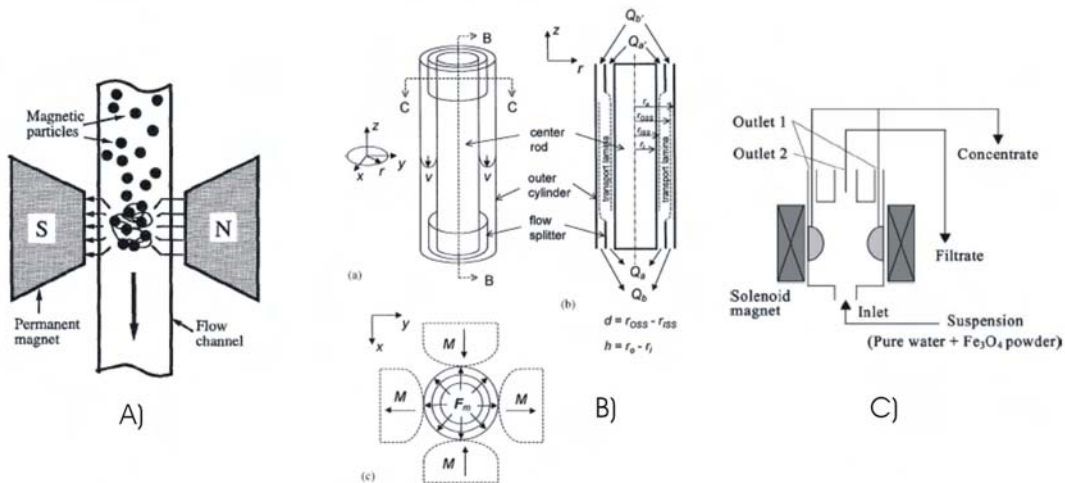
Figure 2.2:   *A) A conventional magnetic separator. A pipe filled with steel wool in an external magnetic field. The external magnetic field magnetizes the steel wool thus introducing magnetic gradients in the pipe and capturing the magnetic beads [8]. B) A quadrupole magnetic separator. Four magnets are placed around the pipe as seen in (c). This gives rise to magnetic forces on the magnetic beads from the center to the sides. Near the center of the pipe the forces are small and the this area is filled by a cylinder where no fluid flows (center rod in (a) and (b)). A flow splitter ((a) and (b)) splits the flow in an outer flow with the magnetic beads and an inner flow with the rest of the sample when continuous flow sorting is performed [35]. C) a magnetic separator using superconducting solenoid magnets [23].*
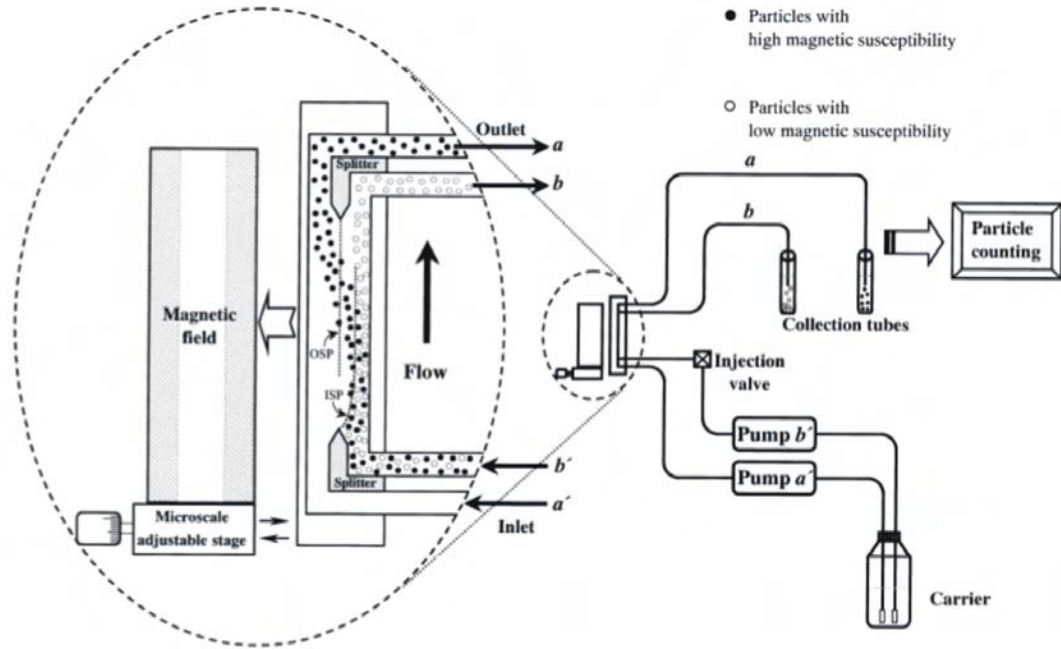
Figure 2.3: *Schematic of the magnetic flow sorter [22].*

2.2.2 Active and passive microsystems for magnetic separation

The magnetic separators I am going to fabricate are for handling very small amounts of sample (microliters). Many different designs of magnetic separators have been proposed in this research area. They can be divided into two different areas: Active systems and passive systems. In active systems electrical contact is made to integrated electromagnetic structures that can be turned on and off locally. In passive systems no electrical contact is made to the microsystem. First an account of the work that has been done on active system is given followed by an account of the work done on passive systems.

Active microsystems for magnetic separation

The first microsystems for magnetic particle separation were active separators. In 1994 the first system of this type was proposed in the literature using four on chip meander type electromagnets [7]. The cores of the electromagnets were extended and brought close to the channel, where they induced a varying magnetic field. See a schematic drawing of the system from a later article in Fig. 2.4. This is a quadrupole magnetic separator which, as mentioned before, is known from larger systems. Capturing capability and subsequent release when the current was turned off was demonstrated. The experiments were performed with magnetic beads from Bangs labs containing 60% solid magnetite. Beads were seen concentrating at the poles within seconds. No information on bead concentration or flow rates were given. The beads used were bought as an aqueous solution

with 10% solids [32]. In Ref. [8] a few further measurements on the same system were presented.
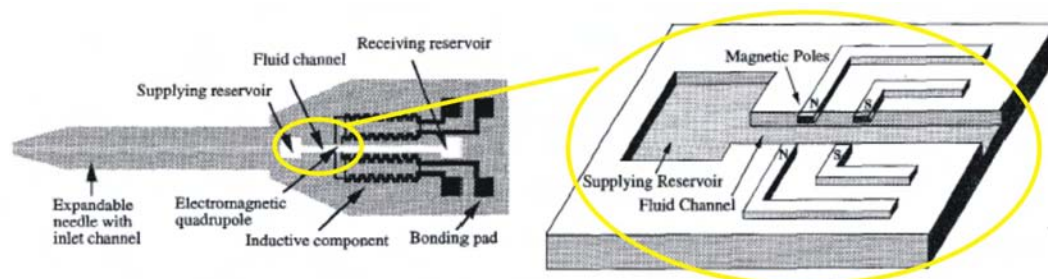
Figure 2.4: *Sketch of the micromachined magnetic separator. The site of separation is magnified [8].*

A magnetic particle separator with planar electromagnets fabricated underneath a fluid channel was presented in [50]. See illustration of design in Fig. 2.5. Capturing capability and subsequent release of the beads was shown. No concentration and flow rates are mentioned. After having the current turned on for 5 seconds, beads would collect at the poles of the electromagnets. The beads used were the same as in [7].

Simulations of the magnetic field and inductive measurements from experiments on the same system were presented in 1997 [32]. Solutions of respectively 10% beads 5% beads and no beads were used. No information on flow rates were given. In [14] theoretical calculations for the system are used to deduce to approximate number of beads on the electromagnets, from inductive measurements. These measurements are done over time to show that the number of beads trapped increases with time. The same beads were used, and no information on flow rates is given.
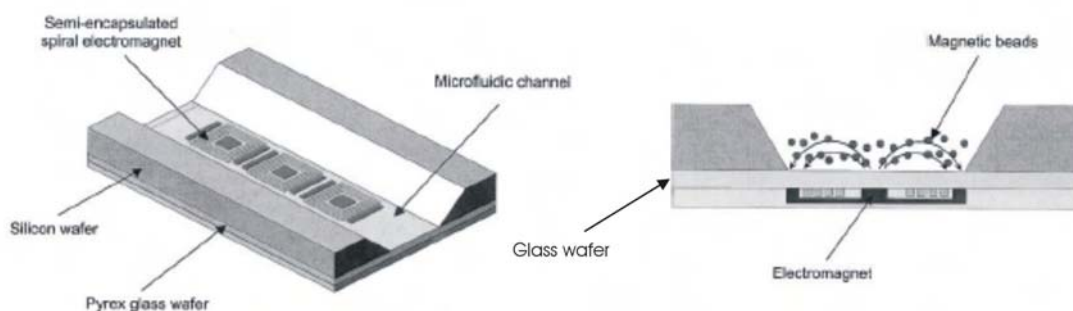
Figure 2.5:   *Sketch of magnetic separator using spiral electromagnets [14].*

A system using serpentine electromagnets for magnetic separation was presented in [13]. The principle is sketched in Fig. 2.6. A sensor was included for measuring the inductance, which should change due to captured magnetic beads. The ability to catch and subsequently release beads was shown both visibly and by inductance measurements.

It was proposed to integrate the design with an electrochemical cell or photo detector.

In Ref. [15] the same type of system was fully integrated with a biochemical detection system, in a microfluidic network containing microvalves, an electrochemical cell, and a flow detector (see Fig. 2.7). Detection of biological molecules with this portable system was demonstrated. They could run an immunoassay, clean, and then run another immunoassay. One run with subsequent cleaning took around 40 min to carry out. Flow rates used between incubation steps was 20 μL/min. In a later article the system was simplified and optimized. It took around 20 min to run an immunoassay [16]. The beads used were Dynabeads M-280 from Dynal [2] and the solution concentration was 1.02×10^7 beads/mL.
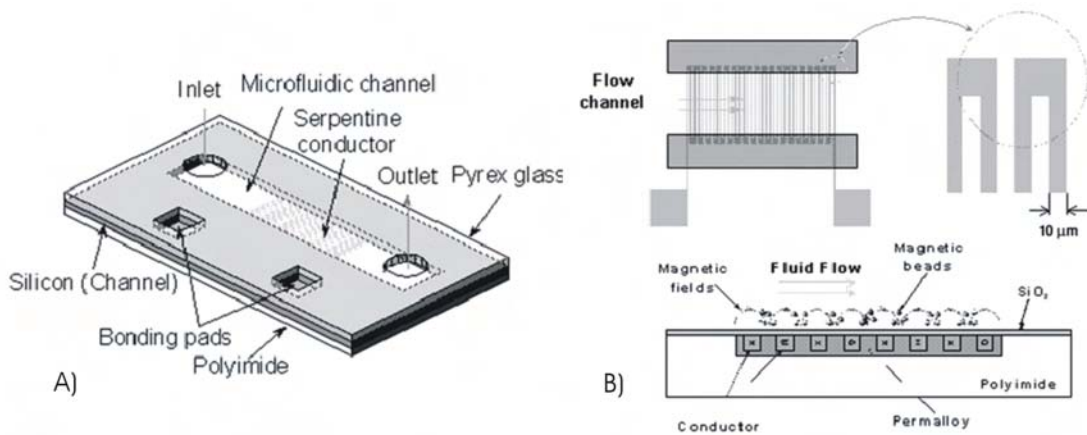
Figure 2.6: *A) Sketch of the magnet particle separator chip. B) Schematic of the working principle of the magnetic particle separator. Both figures from [15].*
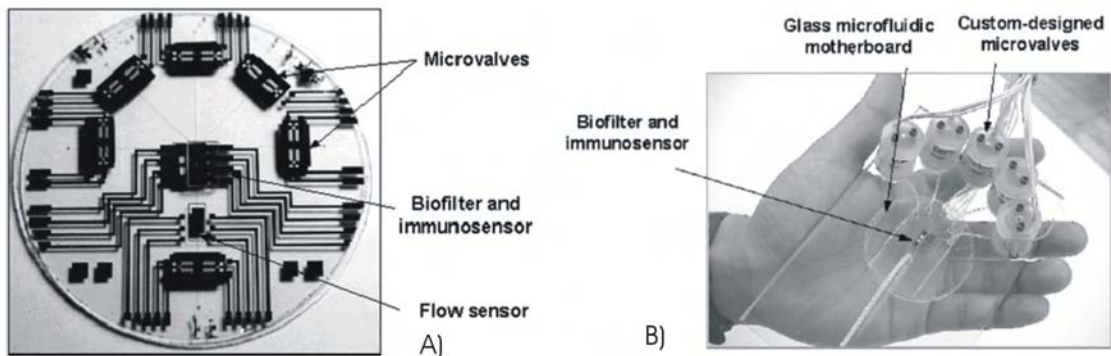
Figure 2.7: *A) Picture of the integrated microfluidic biochemical detection system [15]. B) Picture of simplified and optimized integrated microfluidic Biochemical detection system in the palm of a hand [16].*

A microfluidic magnetic bead sorter was presented in [49]. Two current lines with currents in opposite directions were fabricated beneath the channel. This was combined with a homogenous external magnetic field of 20 kA/m to magnetize the beads (see schematic

in Fig. 2.8). The width of the channel was 12 μm and the depth 4 μm. A plug of beads was allowed to come to rest above the current lines, and depending on the direction of the current or the polarity of the magnetic field, the beads were moved from one side of the channel to the other. The beads used were 0.46 μm in diameter with a content of 11-12% ferrite.
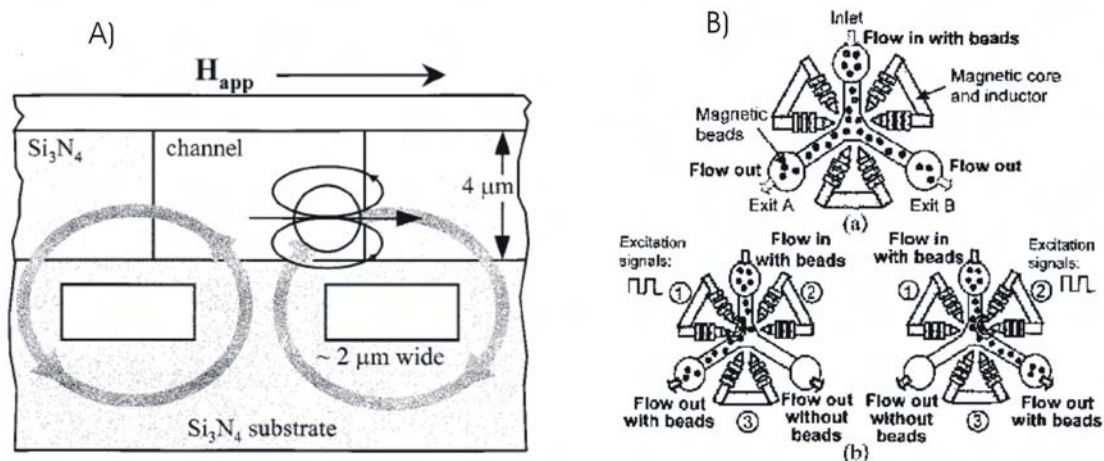
Figure 2.8: *A) Schematic principle of magnetic sorter produced by Tondra et al [49]. B) Schematic principle of magnetic sorter produced by Rong et al (a) before a driving signal is applied (b) after a driving signal is applied to either the right or the left pair of electromagnets [41].*

Another microfluidic magnetic sorter was presented in Ref. [41]. The principle can be seen in Fig. 2.8. The electromagnets seen in the figure were fabricated on the backside of the wafer, and permalloy was used as magnetic interconnections between the back side electromagnets and the front side magnetic tips. The width of the flow channel was 60 μm and the depth was 100 μm. The magnetic beads used in the experiments were SpheroTM [3] with a diameter of 8.8 μm. The current used to drive the electromagnets was 500 mA. No information on the concentration of the bead solution is given. They were able to make the beads flow through either the left or the right outlet using a flow rate of 1 μL/min .

In Ref. [40] four types of planar electromagnets were compared. Three types of meander type electromagnets and a spiral electromagnet. The different designs can be seen in Fig. 2.9. The three meander type electromagnets were both studied theoretically and fabricated followed by squid measurements. The spiral electromagnet was only studied theoretically. The theoretical comparison between the meander type electromagnets suggests that the mesh shaped electromagnet is the most efficient. This is also the result of the measurements. The spiral electromagnets in comparison generated a magnetic field that is up to five times larger than the one created by the best meander type. However the spiral electromagnets are much more complicated to fabricate.
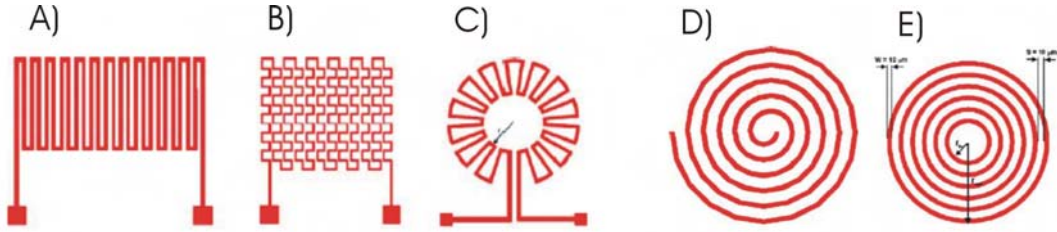
Figure 2.9: *Schematic drawings of the micro-electromagnets investigated in the work A) Straight conductors meander. B) Mesh-shaped meander. C) Rosette-shaped meander. D) Spiral electromagnet. E) Simplified geometry of the spiral electromagnet. This was the geometry used in the calculations. All figures from [40].*

Passive microsystems for magnetic separation

The work on passive magnetic separators is much less extensive than that on active magnetic separators.

The first work performed on passive separators was done by having a permanent magnet close to a channel or pipe. In 1999 a microfluidic system with eight parallel channels was fabricated [20]. In each channel different magnetic beads could be introduced and caught by an external permanent magnet, forming a an array of 8 different targets. The sample could be pushed simultaneously through the channels thus reacting with the different targets (see Fig. 2.10). The system was fabricated so that all channels were equal in length and the width and height of the channels were 120 μm and 40 μm respectively. They were able to introduce different beads to the channels, catch them and subsequently flush sample through for DNA-hybridization. They were also able to perform denaturization using heaters, so the same array could be reused with another sample. It was shown that DNA-hybridization time is greatly reduced using this method, partly because 10 times as many probes in the sample as the amount of targets on the beads was used. No information on flow-rates or the amount of beads used for each experiment is given. Problems with dead volumes in the set-up were experienced. In Fig. 2.10 pictures of beads in a channel before and after hybridization can be seen.

In 2002 a system consisting of cylindrical nickel posts in a microfluidic channel was presented [17]. An external magnetic field, produced by permanent neodynium-iron-boron magnets, magnetized the nickel posts. This introduced magnetic field gradients in the fluidic channel thus capturing the magnetic beads. Once the external magnetic field was removed the nickel posts were partially demagnetized and some of the magnetic beads were released as can be seen on the pictures in Fig. 2.11. The channel was about 150 μm in width and 50 μm in height. The nickel posts were about 7 μm in height and 15 μm in diameter. The beads used were M-450 from Dynal that are $\sim$ 4.5 μm in diameter, in a concentration of $\sim 10^4$ beads/mL. The solution also contained 1% Triton X-100 to prevent aggregation of the beads. The flowrate used in the experiments was $\sim 2\mu$L/min. In the experiments performed an effective separation of magnetic and nonmagnetic beads was carried out. Each post could capture up to $\sim$ 50 beads and when the external magnetic
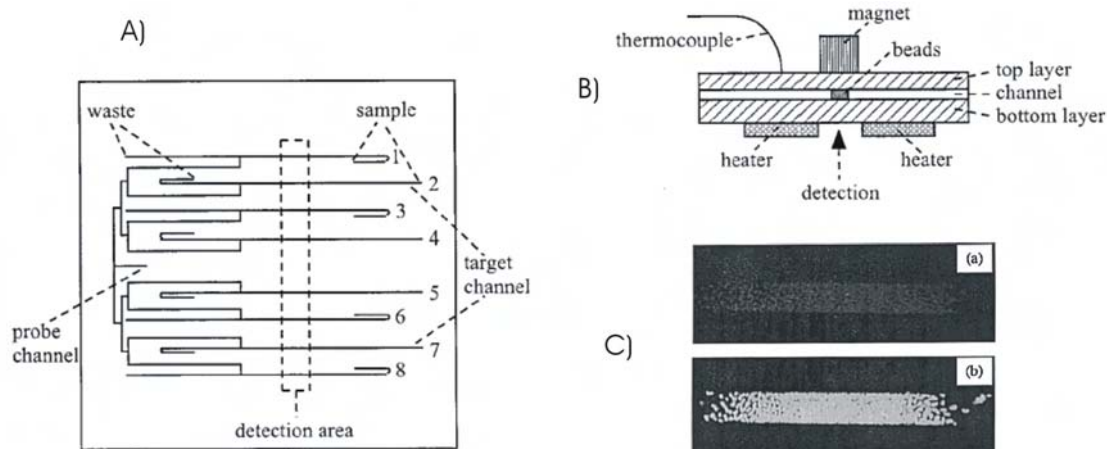
Figure 2.10: *A) Layout of the microfluidic network. B) A schematic cross sectional view of the system with beads introduced. C) Fluorescent images of beads in a microfabricated device. Beads are localized in a channel by a magnet: (a) M-280 beads conjugated with mActin target. (b) The same beads after hybridization with mActin probe. All figures from [20].*

field was removed most, but not all, beads were released.
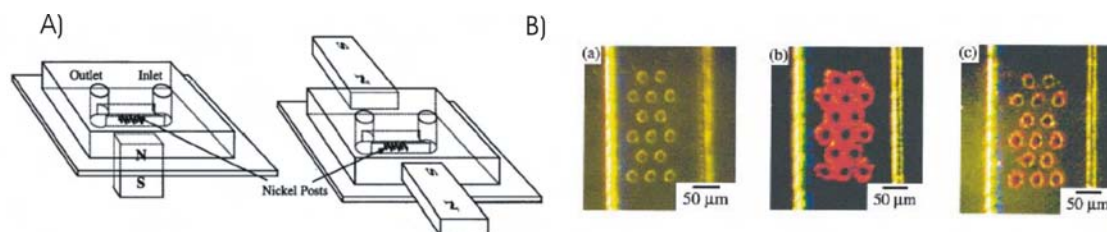
Figure 2.11: *A) A schematic drawing of the magnetic separator. B) Optical micrographs of the magnetic filtration system: nickel posts in a 150 mm wide channel: (a) before catching beads; (b) after applying an external magnetic field, beads caught; (c) releasing beads after removing the external magnetic field. All figures from [17].*

A passive magnetic chaotic mixer similar to the active microfluidic magnetic sorter from [41] is presented in [42]. In this design the electromagnets are external as can be seen in Fig. 2.12. The design could be used for magnetic sorting the same way that the active device was used, but not the other way around. The magnetic tips were connected two and two in the active version while each tip is separate in the passive version. The beads used in the experiments were the spheroTM [3] with a diameter of ~ 8 μm. No bead concentrations are given. The driving current was a sequential signal of 300 mA and a frequency of 0.3 Hz. The channel was 60 μm wide and 100 μm deep.

A magnetic separator based on polymer technology was presented in [18]. It is called a
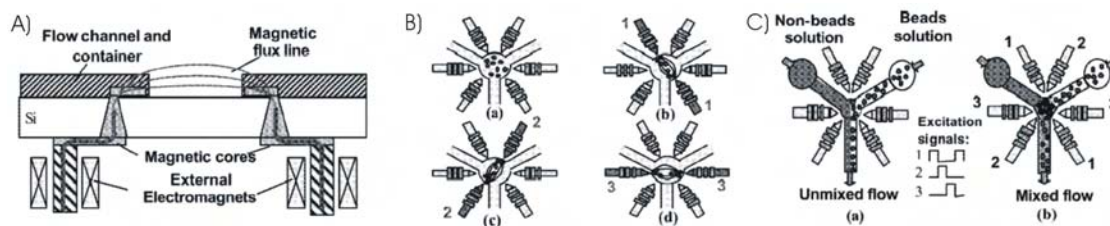
Figure 2.12: *A) A schematic diagram of the magnetic mixer. B) Working principle of magnetic mixer. (a) before excitation; (b); (c); and (d) excitation sequentially to three pairs of tips. C) Mixing action of the mixer. (a) before and (b) after applying drive signal to the three pair tips. All figures from [42].*

disposable magnetic interdigitated array (mIDA). A schematic illustration of the separator is seen in Fig. 2.13. In short it is fabricated by electroplating permalloy elements onto a COC wafer. These elements are embossed into the wafer, and a lid with a channel is bonded to the substrate. Capturing of three different kinds of beads from Spherotech (CM-20-10, CM-40-10, and CM-80-10) was shown. The channel was 2000 μm wide and 70 μm deep. Flow rates were $3-7$ μL/min and driving current of the electromagnets was up to 400 mA. No information on bead concentrations is given.
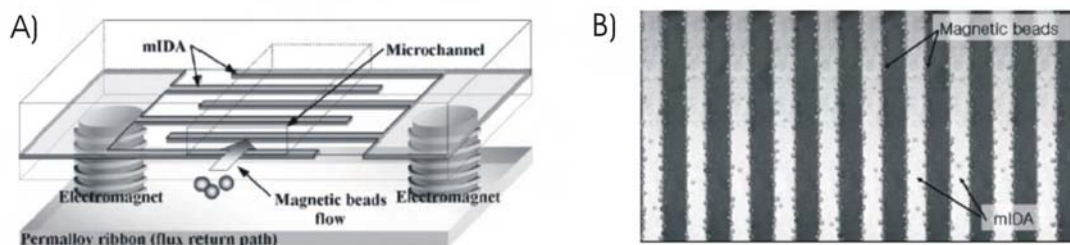
Figure 2.13: *A) Schematic illustration of disposable mIDA. B) Microphotograph showing magnetic bead capture and separation on mIDA. All figures from [18].*

2.3 The different systems and challenges

In the previous section a review of articles was given. What can this be used for? First of all it provides a background knowledge of what is possible and what has already been done. But more importantly it provides an idea of what challenges have not yet been solved by others. There is not much fun in doing exactly the same as others before you.

Essentially two different kinds of systems were presented. Active and passive separators. Both types of course have advantages and disadvantages.

2.3.1 Active separators

Active separators have the potential for being integrated into very small systems. It is also possible to turn the magnetic field on and off locally in active magnetic separators. This makes it possible to produce addressable arrays where beads can be caught and released at different points independently of each other [44].

These systems, however, are usually complicated to fabricate. This also means that it is expensive and time consuming. The capturing efficiency of active systems is usually not so good. In the articles mentioned almost no information on bead solutions and flow rates are given. In Ref. [40], however, it is found that the spiral electromagnet is much more effective than many of the other designs of electromagnets used. A spiral electromagnet is the type of electromagnet used in [14]. In [43] an improved version of this design was produced and characterized. In this work it was shown that very low flow rates were necessary to obtain capturing ($\sim 1 - 2\mu$L/min). Capturing efficiency of active separators can be increased by combining active structures and external magnetic fields. This however ruins the concept of integrating the separators into very small systems.

2.3.2 Passive separators

Passive separators can be very simple to fabricate (but also very complicated as in Ref. [42]). In this type of system it is also possible to obtain high capturing efficiency (again hard to see, but in Ref. [17] they actually state the flow rate and solution concentration used).

Passive systems, however, have to be placed in a magnetic field created by some kind of external device. Also all capturing sites are turned either on or off at the same time, unless a very complicated structure and external magnetic field generator is fabricated (as in [42]).

2.3.3 Challenges

From the review it is obvious that one of the things I found, was that no one has performed a thorough characterization of the systems. Neither qualitative nor quantitative. In a few articles ([17] and [16]) information on both bead concentrations and flow rates are supplied. But even here the flow rates have not been varied, and only in Ref. [17] do they offer proof that almost all beads were caught. This was the main challenge I wanted to address in this project. To characterize systems at different flow rates, offer proof that most beads were captured, and if possible do quantitative measurements of capturing efficiency.

2.4 Review of literature on microfluidic mixers

In microchannels the mixing of liquids is a problem often encountered. This comes from the fact that the Reynolds number is proportional to the size of the system (see Eq. (3.10)). When the Reynolds number is low the flow becomes laminar. This makes mixing difficult because it has to rely on diffusion. Since the Reynolds number is also proportional to the

velocity of the flow, it is possible to make the Reynolds number higher, by making the average velocity higher. This of course is not always convenient.

Different ways to obtain mixing in microsystems have been proposed [36]. The one I am focusing on, is obtaining rotations in the cross-sectional plane of the channel, by having ridges/grooves at the top or the bottom of the channel. In this section an overview of the work done in this area is given.

2.4.1 Microfluidic mixers using grooves or ridges

The first time this type of mixer was proposed in the literature was in 2001 [9]. In this article a theoretical investigation was used to propose that grooves/ridges can be used to create transverse velocities in the fluid flow. It was suggested that this might be used to design mixers.

In 2002 channels with grooves were fabricated, and it was shown that the mixing was greatly enhanced compared to a similar channel without grooves [29]. In Fig. 2.14 sketches and micrographs of a channel with grooves and a channel without grooves are seen. They represent experiments in which a stream of water with Rhodamine B and a stream of buffer enters the channel. It is seen that the grooves enhance mixing. Simulations were also performed, and used for a comparison to the experiments. Later in 2002 another article about the same system was published. Here simulations with varying groove depth and angle were performed [28].

In Ref. [45] two different microfluidic mixers were fabricated (a diagonal mixer (DM) and a staggered herringbone mixer (SHM). See illustrations in Fig. 2.15) and the mixing efficiency of the two mixers was compared. A comparison of the mixing efficiency for the two mixers and a channel without grooves was also presented. Schematics and micrographs of the two different mixers can be seen in Fig. 2.15). It was concluded that the SHM is by far the better mixer, but also that both mixers are a lot better than a channel without mixer.

A more thorough investigation of the DM followed [46]. In this article an approximated analytical description of the fluid flow was developed, and this was used to derive an equation for the angle between the velocity vector and the longitudinal axis of the channel, just below the top surface. This angle can be used as a measure of the magnitude of the cross sectional rotations created in the flow. They also compare this to experiments in which they measure this angle for different parameters for the channels and grooves (see Fig. 2.16). In the experiments a narrow strip of dyed water enters the channel next to a buffer stream. The helical flow forces the dyed water to the other side of the channel under the top surface, and the angle of the velocity of the dyed water can be measured (see Fig. 2.16).

In 2004 it was shown that the mixing efficiency of the DM could be improved by incorporating barriers under the top surface, parallel to the channel (see Fig. 2.17) [31]. This is called a barrier embedded micromixer (BEM). The fabrication sequence for this kind of mixer, however, is more complicated than for the DM and the SHM.

In Ref. [30], theoretical simulations for a DM, SHM, and BEM were performed and the mixing efficiency compared, using a so called colored particle tracking method. This
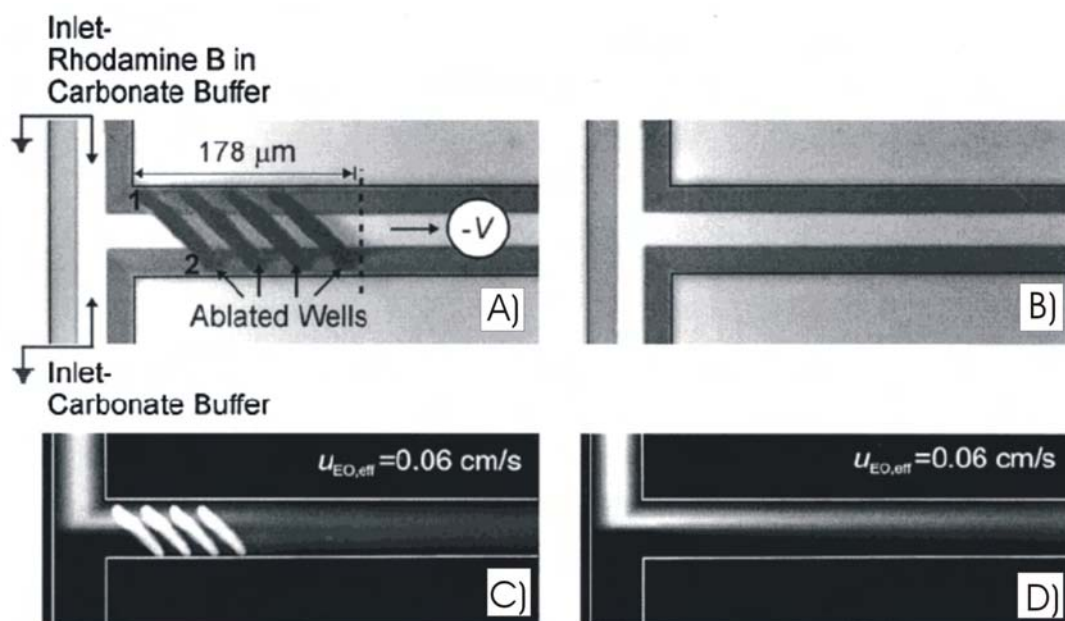
Figure 2.14: *A) Configuration of the experimental set-up and white light microscopy image of an imprinted T-channel with a series of ablated wells. B) White light image of a T-channel without the ablated wells. C) and D) Fluorescence images of electroosmotic flow at a flow rate of 0.06 cm/s. All figures from [29].*

is a variation of the particle tracking method presented in [10], where the fluid flow is calculated and then used to calculate particle trajectories. It is assumed that the particles are massless and without influence on the fluid flow. In [30] two different colors of particles are used and cross sectional plots of where they are in the channel are made. It was found that the SHM is the best mixer followed by the BEM. They also found that both the BEM and the SHM are far better mixers than the DM.

2.4.2 Choice of mixers and challenges

From the review it is seen that of this kind of mixer three main types have been proposed. The staggered herringbone mixer (SHM), the diagonal mixer (DM), and the barrier embedded mixer (BEM). The SHM is shown to be the best mixer closely followed by the BEM. However, the BEM is more complicated to fabricate. The DM is not as effective a mixer, but the main purpose of the mixer in my systems is not to mix fluid, but to bring the magnetic beads close to the sides of the channel. Also the driving mechanism of the SHM and the DM is the same, and therefore one system might tell something about the other system.

As with the magnetic separators some work on these microfluidic mixers has been performed, but many challenges still exist. Comparisons between the mixers have been performed, but general design rules of how to maximize the mixing efficiency of one type
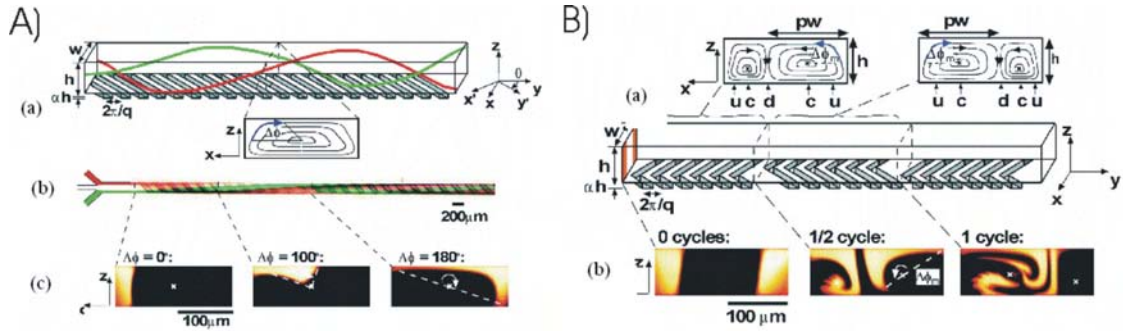
Figure 2.15: *Two different kinds of mixers A) a diagonal mixer (DM). (a) A schematic diagram of channel with ridges and the 3D twisting flow. (b) Optical micrograph showing a top view of a red stream and a green stream flowing on either side of a clear stream. (c) Fluorescent confocal micrographs of vertical cross sections. B) a staggered herringbone mixer (SHM). (a) Schematic diagram of one-and-a-half cycles of the SHM. A mixing cycle is composed of two sequential regions of ridges; the direction of asymmetry of the herringbones switches with respect to the centerline of the channel from one region to the next. The streamlines of the flow in the cross section are shown schematically above the channel. (b) Confocal micrographs of vertical cross sections of channel. Two streams of fluorescent solution were injected on either side of a stream of clear solution. Both figures from [45].*

Figure 2.16: *Predicted and measured values of the angle of the velocity below the top surface (tan Ω) in a channel with square grooves on the floor. In all cases $w = 200\mu m$, hc is given in micrometers, and the grooves are oriented at an angle $\pi/4$ with respect to the principal axis of the channel. Also shown is a micrograph taken from above of a stream of black dye flowing in a microchannel with $pr = 140$ μm, $hc = 106$ μm, and $rc = 0.51$. The drawing on the left shows schematically the Y junction at the entrance of the channel; a narrow stream of black dye in water is injected alongside a broad stream of clear water (flow rate of the clear stream 20 times that of the dyed one). The average flow speed in the channel is 1 cm/s (Reynolds number ~ 1) [46].*

of mixer do not exist. In the following chapter the DM and the SHM are investigated further and during this, I try to formulate some general rules on how to maximize their mixing efficiency.
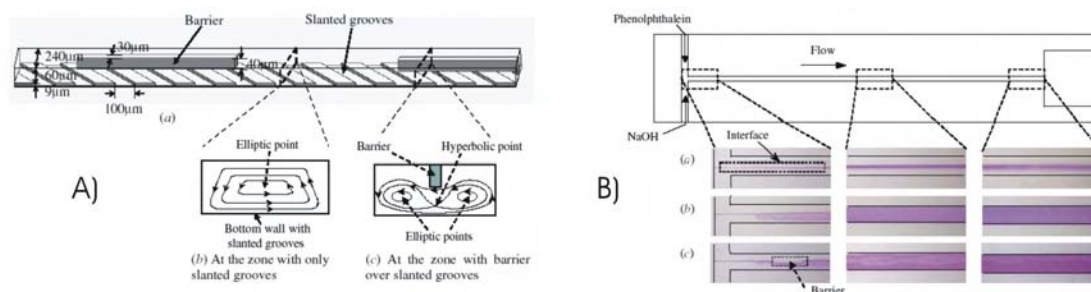
Figure 2.17: *A) Barrier embedded micromixer: (a) schematic view, (b) and (c) cross-sectional velocity fields at two typical locations. Slanted grooves patterned on the bottom wall cause helical flow the cross-sectional velocity field of which is schematically represented by (b) while the cross-sectional velocity field of (c) is obtained due to the existence of a barrier inserted on the top wall. B) Mixing experiment results of: (a) T-channel, (b) DM and (c) BEM, at the indicated positions, at the flow rate of 10.0 μL/min (Re ∼ 0.5). In this case, the BEM has a barrier per two grooves and no barrier per the next two grooves in a periodic manner. Only the reacted phenolphthalein at the interface between the phenolphthalein and NaOH streams shows as a red color. Both figures from [31].*

Chapter 3

Microfluidic theory

The systems fabricated in this project consist of microfluidic channels and magnetic elements. Therefore basic knowledge of fluid dynamics and magnetism is necessary to understand the physics of the system. This chapter will present the basic hydrodynamic equations and simplifications of these due to the systems I am working on. I will also present some concepts and parameters related to the systems and give the analytical result for the flow in an infinitely long rectangular channel.

3.1 Fluid particles

Before starting to work with the equations of fluid dynamics I need to introduce the concept of a fluid particle, and see if it is applicable for my systems. The discussion of Ref. [12] is followed. The equations of fluid dynamics are based on the assumption that physical properties like pressure, temperature and velocity vary continuously from point to point throughout the sample. This means that it has to be defined what a point in a fluid sample is so that these requirements are met. If a point is seen as a particle of fluid with a volume, and a large volume of fluid as an aggregate of many such particles. Then the physical properties of bulk fluid can be ascribed to each fluid particle.

Fluid consists of molecules that move around randomly. This means that if a fluid particle is defined as only being the size of a few molecules then local measurements on a particle would fluctuate. On the other hand, if the volume of a fluid particle becomes large, variations from one place in the particle to another, due to external forces, can be present. This means that a fluid particle needs to be defined as a volume of fluid large enough for fluctuations in measurements to become negligibly small, but too small for large variations across the particle to be present.

The average distance between molecules in a fluid is around 0.3 nm. A cubic fluid particle with a side length of 10 nm contains around 4×10^4 molecules and this makes, e.g., the relative fluctuation in the particle number N to be of the order $\frac{1}{\sqrt{N}} \sim 0.5\%$.

This means that the fluid particle concept holds for fluid particles in the size of tens of nm. For the concept to work, however, this length has to be much smaller than the smallest size of the system. The microfluidic part of the systems has dimensions between

20 μm and 2 mm. This means that the smallest feature in the system is $\sim 10^3$ times larger than a fluid particle. In that case the fluid particle model is valid.

3.2   The continuity equation

The continuity equation is the equation of conservation of mass, for fluid dynamics, and the first fundamental equation of fluid dynamics [12].

$$\partial_t \rho + \boldsymbol{\nabla} \cdot (\rho \mathbf{v}) = 0 \tag{3.1}$$

Where ρ is the mass density, and $\mathbf{v}(\mathbf{r}, t)$ is the velocity vector for the fluid. In this work it is assumed that the fluid density is independent of time and place. This is called an incompressible fluid and with this assumption the continuity equation reduces to

$$\boldsymbol{\nabla} \cdot \mathbf{v} = 0 \tag{3.2}$$

This assumption is reasonable for fluid velocities much smaller than the velocity of sound in the fluid.

3.3   Navier-Stokes equation

The Navier-Stokes equation is the equation of motion for fluid dynamics, and as such is derived from Newton's second law. It is the second fundamental equation of fluid dynamics [12].

$$\rho(\partial_t \mathbf{v} + \mathbf{v} \cdot \boldsymbol{\nabla})\mathbf{v} = \boldsymbol{\nabla} \cdot \sigma + \rho \mathbf{g} + \mathbf{f} \tag{3.3}$$

Where σ is the Caucy stress tensor describing the pressure forces and the viscous forces, $\mathbf{g}$ is the gravity acceleration, and $\mathbf{f}$ are the remaining forces acting on the fluid, e.g., magnetic forces. As before a number of simplifications can be made to this equation. The systems I am trying to describe are in a stationary regime, which means that all time derivatives are zero. In the experiments the channel length is perpendicular to the gravity. This means that the force from the gravity is compensated by the normal force from the bottom of the channel. The incompressible fluid assumption means that the stress tensor is reduced considerably and I can switch from tensor to vector calculations, and no other forces do work on the fluid in my system. The reduced Navier-Stokes equation I use in my calculations becomes

$$\rho(\mathbf{v} \cdot \boldsymbol{\nabla})\mathbf{v} = -\boldsymbol{\nabla} p + \eta \boldsymbol{\nabla}^2 \mathbf{v} \tag{3.4}$$

where η is the dynamic viscosity of the fluid, and p is the pressure. Both coming from the reduced stress tensor. It is seen that there is a linear and a nonlinear part. The nonlinear part ($\rho(\mathbf{v} \cdot \boldsymbol{\nabla})\mathbf{v}$) represents inertia forces, and the linear part ($-\boldsymbol{\nabla} p + \eta \boldsymbol{\nabla}^2 \mathbf{v}$) represents the pressure and viscous forces.

3.4 No-slip boundary condition

The no-slip boundary condition means that the velocity of the fluid is zero at the solid fluid interface. This seems generally to agree with macroscopic experiments, but evidence exists that a slip velocity is present at the boundary and that this becomes more important for smaller systems [51]. The effect, however, becomes smaller with increasing surface roughness, and the roughness of the surfaces in my systems is large (at least of the side walls). Furthermore the purpose of this project is not to investigate slip/no-slip conditions which is a research area in itself. It was therefore chosen to adopt the no-slip boundary condition, which will be used for the rest of this project.

3.5 Flow in simple rectangular channel

In my systems the fluid is driven through a long channel by applying a constant pressure drop from one end of the channel to the other end of the channel. In the case of systems without an integrated microfluidic mixer the channel is translationally invariant along the channel (the x-direction). This gives a Poiseuille flow. For this type of flow an analytical solution can be found.

The height of the channel (h) is in the z direction and the width w is in the y direction. The boundaries are found at $z = 0, h$, and $y = -\frac{w}{2}, \frac{w}{2}$, and I have that $\frac{w}{h} > 1$. Since the geometry is translationally invariant in the x direction the velocity can only depend on y and z. Also the driving force (the pressure gradient) points in the x direction and therefore only the x component of the velocity is non-zero. If I look at the nonlinear part of the Navier-Stokes equation this gives

$$(\mathbf{v} \cdot \boldsymbol{\nabla})\mathbf{v} = (v_x(y, z)\mathbf{e}_x \cdot \boldsymbol{\nabla})v_x(y, z)\mathbf{e}_x = v_x(y, z)\partial_x v_x(y, z) = 0 \qquad (3.5)$$

since the velocity does not vary in the x direction. The equation to be solved is

$$\eta \boldsymbol{\nabla}^2 v_x = \boldsymbol{\nabla} p \qquad \Leftrightarrow \qquad (\partial_y^2 + \partial_z^2)v_x = \frac{1}{\eta}\partial_x p \qquad (3.6)$$

I see that since $v_x(y, z)$ is independent of x the pressure gradient must also be constant. From this I get $\partial_x p = -\frac{\Delta p}{L}$. Since I assume that the no-slip boundary condition is valid, the boundary conditions are

$$v_x\left(-\frac{w}{2}, z\right) = v_x\left(\frac{w}{2}, z\right) = v_x(y, 0) = v_x(y, h) = 0 \qquad (3.7)$$

The solution to this problem is found by expanding both sides of the equation as Fourier series in the short z direction. This is combined with an unknown function of y and, when solved, the solution becomes [12]

$$v_x(y, z) = \frac{4h^2 \Delta p}{\pi^3 \eta L} \sum_{n,\text{odd}}^{\infty} \frac{1}{n^3}\left[1 - \frac{\cosh(n\pi\frac{y}{h})}{\cosh(n\pi\frac{w}{2h})}\right]\sin(n\pi\frac{z}{h}) \qquad (3.8)$$

This equation is used in Sec. 3.7 and it is also used as a comparison to a simulation for validation of the calculational method in Chap. 4.

3.6   Reynolds number

The Reynolds number is a number that says something about which forces dominate the flow. Inertia forces or viscous forces. If the ratio of the size of the inertia forces over the size of the viscous forces is taken I get

$$\frac{|\rho(\mathbf{v} \cdot \boldsymbol{\nabla})\mathbf{v}|}{|\eta \boldsymbol{\nabla}^2 \mathbf{v}|} \tag{3.9}$$

Looking at this expression in an approximate way, I can say that $|\mathbf{v}| \sim v_0$ and $|\boldsymbol{\nabla}| \sim \frac{1}{L_0}$, where v_0 is a velocity, and L_0 is a length, characteristic for the system. This gives the Reynolds number

$$Re \equiv \frac{\rho v_0 L_0}{\eta} \tag{3.10}$$

This of course is a very simple and not mathematically correct way to come to this result. In stead I can describe the velocity as $\mathbf{v} = v_0 \tilde{\mathbf{v}}$ and the coordinate by $\mathbf{r} = L_0 \tilde{\mathbf{r}}$ where tilde implies that the vector is dimensionless. From this it follows that $\boldsymbol{\nabla} = L_0 \tilde{\boldsymbol{\nabla}}$. The pressure is measured in units of either $p_0 = \frac{\eta v_0}{L_0}$ or ρv_0^2, where the former is the appropriate way for flows dominated by viscous forces [12]. If this is inserted to Eq. (3.4) I get

$$\rho(v_0 \tilde{\mathbf{v}} \cdot \frac{p_0}{L_0} \tilde{\boldsymbol{\nabla}}) \cdot v_0 \tilde{\mathbf{v}} = -\frac{1}{L_0} \tilde{\boldsymbol{\nabla}} \tilde{p} + \eta (\frac{1}{L_0^2}) \tilde{\boldsymbol{\nabla}}^2 v_0 \tilde{\mathbf{v}} \qquad \Leftrightarrow \qquad Re(\tilde{\mathbf{v}} \cdot \tilde{\boldsymbol{\nabla}}) \cdot \tilde{\mathbf{v}} = -\tilde{\boldsymbol{\nabla}} \tilde{p} + \tilde{\boldsymbol{\nabla}}^2 \tilde{\mathbf{v}} \tag{3.11}$$

From this it is seen that the viscous forces dominate when $Re \ll 1$ and the inertia forces dominate when when $Re \gg 1$. If I try to enter typical values for water in a microsystem into Eq. (3.10) I get

$$Re = \frac{\rho v_0 L_0}{\eta} = \frac{10^3 \text{ kg m}^{-3} \times 10^{-3} \text{ m s}^{-1} \times 10^{-4} \text{ m}}{10^{-3} \text{ kg s}^{-1}\text{m}^{-1}} = 0.1 \tag{3.12}$$

It is seen that microsystems are in the region where it might be possible to omit the nonlinear term, even though there is no translational invariance in the direction of the pressure gradient.

If the nonlinear term is omitted,the inertia term from the Navier-Stokes equation the resulting equation is called the Stokes equation. This describes a linear flow, which means that the velocities change direction immediately when the driving force $(-\boldsymbol{\nabla} p)$ changes direction. This means that the flow will be the exact opposite if the the pressure drop is negated. This also means that no turbulence can be present, since it is a nonlinear effect that would change if the driving force was negated. Microfluidic flows therefore tend to be completely laminar.

3.7   Hydraulic resistance

The last concept I will present here is hydraulic resistance. This is a very important concept in microfluidic networks. I only work with one channel, however the concept of

hydraulic resistance is used in a model in Chap. 4. I therefore introduce the concept here.

From the fluid flow in a rectangular channel it is seen that a constant pressure gradient along the channel gives velocities that are independent of x. If the velocity field is integrated in the y and z directions it gives the flow rate (Q) [12].

$$Q = \frac{h^3 w \delta p}{12 \eta L} \left[1 - \sum_{n,\text{odd}}^{\infty} \frac{1}{n^5} \frac{192}{\pi^5} \frac{h}{w} \tanh(n\pi \frac{w}{2h}) \right] \tag{3.13}$$

For a given channel it is seen that the flow rate depends only on the pressure gradient (the driving force) and a constant for the channel, given by the channel dimensions and the fluid used, that governs the drag on the fluid. It is seen that this constant is highly dependant on the channel cross section (approximately proportional to $h^3 w$). This is very similar to Ohm's law $(\Delta U = RI)$ where δU (the electrical potential drop) is the driving force, I is the electrical current that flows in the wire, and R is the resistance of the wire given by the dimensions and material of the wire. If a hydraulic resistance (R_{hyd}) is defined as the relationship of Q and Δp and this is written similar to Ohm's law I get

$$\Delta p = R_{hyd} Q \tag{3.14}$$

The great thing about the hydraulic resistance is that it is possible to work with it in the same way that you work with electrical resistance. If two channels have hydraulic resistances $R_{hyd,1}$ and $R_{hyd,2}$ the resulting hydraulic resistance for a system (R_{hyd}) becomes in the serial and parallel case

$$R_{hyd,1} + R_{hyd,2} = R_{hyd}, \qquad \text{and} \qquad \frac{1}{R_{hyd,1}} + \frac{1}{R_{hyd,2}} = \frac{1}{R_{hyd}} \tag{3.15}$$

This makes it possible to predict the flow rate in all channels in a fluidic network, just by knowing the dimensions of all the channels, and the pressure drop over the microfluidic network. This only works, however, for low Reynolds numbers. Hence its relation to microfluidics.

Chapter 4

Mixing in microchannels

In this chapter I will start by explaining the working principle of the diagonal mixer and the staggered herringbone mixer. After that the parameters used for describing the mixers will be defined and the way the effectiveness of the mixers is evaluated will be presented. Then I will go through some of the simulations performed and what this means for the design of this type of micromixers in general. I will also present what systems I ended up choosing. The last part of this chapter will be dedicated to the experiments performed and the comparison to simulations.

4.1   Working principle of the mixers

In this section I try to explain the working principle of mixers using grooves or ridges by the use of two simple models. With the models I try to explain how cross sectional rotations in the fluid flow are created. In the following I refer to the illustrations presented in Fig. 4.1.

The first model presented is an intuitive model based on the illustrations A) to C). A) shows a fluidic channel. In the channel a fluid flow is driven by a pressure drop. When the fluid reaches the bend in the channel, the direction of the flow is bent. In this case it is the only direction in which the fluid can move, but the direction of a fluid flow will always be diverted when it hits a rigid obstacle. B) and C) show a channel with a DM. As in A) a fluid flow is coming into the channel, but in this case the "bend" of the channel only fills part of the channel. Still some of the fluid near the bottom of the channel will be diverted out towards the sidewall. If many ridges are coming after each other this will still happen. Because if a pressure drop from a to d is present there will also be a pressure drop from b to c. This gives a flow along the channel between the ridges which will reach the next ridge and be diverted out towards the side wall. This gives a net flux of fluid towards one sidewall near the bottom of the channel, and gives a built up pressure at that sidewall. This pressure difference between the two sides of the channel drives a recirculation of the fluid under the top surface, as can be seen in G). Since I am working with incompressible fluids it is clear that this has to happen. The fluid cannot be pressed together at the sidewall, so the flux at the lower part of the channel, has to be compensated by an equally
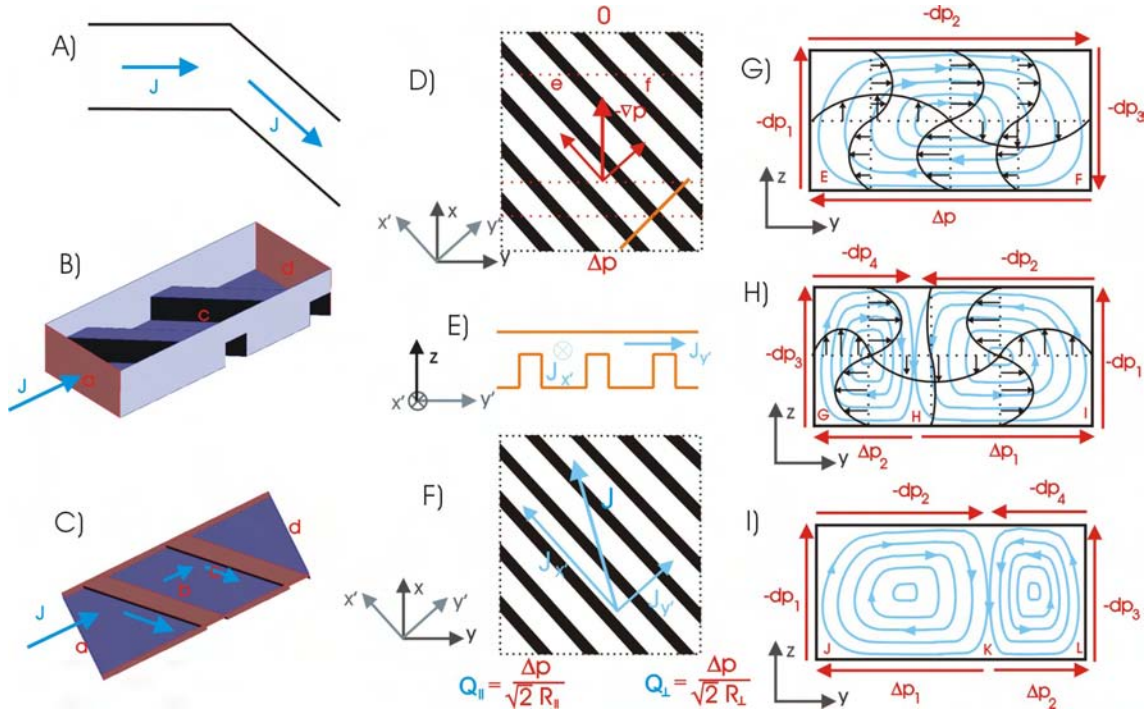
Figure 4.1: *Illustrations of the working principle of the mixers. A), B), and C) are used for an intuitive model, D), E) and F) are used for a model based on Ref. [46], and H), I), and J) is the result of both models. A) shows a fluidic channel seen from above. B) and C) shows the same channel with a DM from two different points of view. In both cases the view is down into the channel through a transparent channel top surface. In C) the channel is almost seen from straight above and in B) the brown surfaces are the inlet and outlet surfaces. D) and F) shows a slab geometry seen from above. The bottom plate has ridges (the black parts) and the top plate is flat (and transparent in this picture). The plates are infinitely wide. E) shows a cross section of this structure indicated by the orange line in D). G) shows a simplified (the ridges have been removed) channel cross section of a DM. The black curves and vectors are the fluid velocities in the y and z directions. It is the gradients in the fluid velocities that generate energy dispersion. The larger the gradients the larger the resistance encountered. H) and I) are similar cross section for a SHM with the small rotation in the left and right side respectively. When comparing G) and H) it is seen that the energy dispersion due to the gradients of v_z in the y direction are larger for the SHM than for the DM and vice versa for the energy dispersion due to the gradients of v_y in the z direction.*

large flux in the other direction in the upper part of the channel. When looking at the case of the herringbone mixer, the fluid is pushed from the middle of the channel out towards both sidewalls. This means that a build-up in pressure is found at both walls and that drives a recirculation of the fluid towards the middle of the channel as seen in H) and I). The rotations are made asymmetric by making the herringbones asymmetric. Then the

principle is that the side in which the large/small rotation is present switches after a few herringbones. This gives an effective stretching and folding of the fluid.

The second model (using illustrations D) to F) is primarily based on an analytic investigation from Ref. [46]. The drawings show a slab geometry (infinitely wide) with ridges at the bottom surface. The two end surfaces are held at constant pressures with a pressure drop Δp from one surface to the other. In D) two points have been marked by e and f. Because the channel is infinitely wide it has a periodically perturbed translational invariance in the y direction the pressure at these points must be the same. This gives an average pressure gradient in the x direction. This pressure gradient can be divided into gradients along x' (parallel to the ridges) and y' (perpendicular to the ridges). The ridges are placed at an angle of 45° to the pressure gradient for the sake of simplicity. The total flux in these two directions is controlled by the hydraulic resistance in each direction. From E) it is clear that the hydraulic resistance along y' is larger than the hydraulic resistance along x'. It can be brought to the limit where the ridges actually block the channel in the y' direction. In this case the total flux will be in the x' direction. When the ridges do not block the channel in the y' direction the total flux will have a direction between the x' and the x direction, as is seen in F). In Ref. [46] an analytical description of a similar system is presented. The system is a slab geometry where the ridges are represented by a sinusoidal perturbation of the bottom plate. The flow is solved in the x' and y' direction by perturbation of the parabolic flow profile present between two parallel infinitely wide plates. They find that the average flow in the two directions found from the analytical result can be approximated as perturbations to the fluid flow without the sinusoidal bottom as either; 1) a slip velocity at the bottom plate in the opposite direction of the flow, or 2) as an effective lowering of the channel height. It is also found that this effect is more pronounced along y' than along x' which again brings me back to the situation sketched in F). If sidewalls are put on this geometry it is the same case as in the intuitive model, where fluid is pushed to one side of the channel resulting in a pressure build-up and recirculation of the fluid as seen in G).

G) to I) are representations of the distribution of transverse velocities in a DM and an SHM. The models are simplified in that they do not include the ridges, but only the average result of a fluid being pressed from one side of a simple channel to the other side near the bottom (or from the middle of the channel towards the sides). The black curves and vectors are representations of the velocity distribution in either the y or z direction along characteristic lines. It is seen that only one node is present in the case of the DM whereas two nodes are present in the case of the SHM. This makes the energy dispersion due to gradients of v_z in the y direction larger for the SHM. The energy dispersion due to gradients of v_y in the z direction, however, is lowered for the SHM. This is because where the rotations meet no gradients of v_y in the z direction are present. These two effects pull in opposite directions, and this makes it difficult to predict which mixer can create the largest ratio between transverse and longitudinal velocities in the channel. It also shows that the dependence of the rotations on the ratio between width and height of the channel should be different for the two types of mixers. If the mixer should be effective for our purpose, however, the flux should be large close to the sidewalls where the large magnetic forces are present. Due to the larger gradients of the velocity in the y direction the flux

will be larger close to the sidewall for the SHM than for the DM if the rotations for the two mixers are of the same magnitude.

From H) it is possible to make another prediction for the herringbone mixers. If there is a difference in size of the two rotations, the transverse velocities of the small rotation will be lower than the velocities in the large rotation. This can be seen from H) where the gradients of v_z in the y direction are larger for the small rotation than for the large rotation if the transverse velocities in the two rotations have the same size. This difference will go towards zero as the channel gets wider, since for an infinitely wide channel the energy dispersion due to gradient of v_z in the y direction becomes negligible, and the energy dispersion is governed by the gradients of v_y in the z direction which are equivalent for the two rotations since the height of the two rotations is the same.

4.2   Choice and evaluation of mixers

In this work I have chosen to investigate the DM and SHM. As mentioned in Chap. 1 the primary purpose of the mixer is not to mix the fluid but to bring the magnetic beads close to the sides of the channel. This means that it is not obvious which mixer is the best to use. If a DM is compared to an SHM, the best mixing is achieved with the SHM. This, however, is not necessarily the same as bringing as many beads close to the sides of the channel as possible.

In Table. 4.1 The parameters used to describe the mixers are defined. In Fig. 4.2 the parameters are illustrated on sketches of the two types of micromixers.

SHM/DM		**SHM**	
Parameter	**Description**	**Parameter**	**Description**
w	Width of channel	w_s	Width of small rotation
h_c	Height of channel	w_l	Width of large rotation
h_r	Height of ridges	a_s	w_s/w
r_c	h_r/h_c	s_p	Staggering period
p_r	Period of ridges		
w_r	Width of ridges		
r_p	w_r/p_r		

Table 4.1: *Table defining parameters used to describe the mixers.*

The simplest of the two kinds of micromixers is the DM, and therefore that is the system on which the simulation work was started. The results from the analysis of the DM's should also say a lot about the influence of different parameters on the SHM's, since essentially it is the same mechanism that drives the two different micromixers.

To be able to evaluate the effectiveness of the micromixers, a way to quantify this effectiveness had to be found. Since the purpose of the mixer is to bring as many beads as possible close to the sides of the channel, one way to evaluate the effectiveness of the mixer (and the magnitude of the rotations) is to find the flux through a plane close to the side of the channel. Another way to evaluate the magnitude of the rotations is the
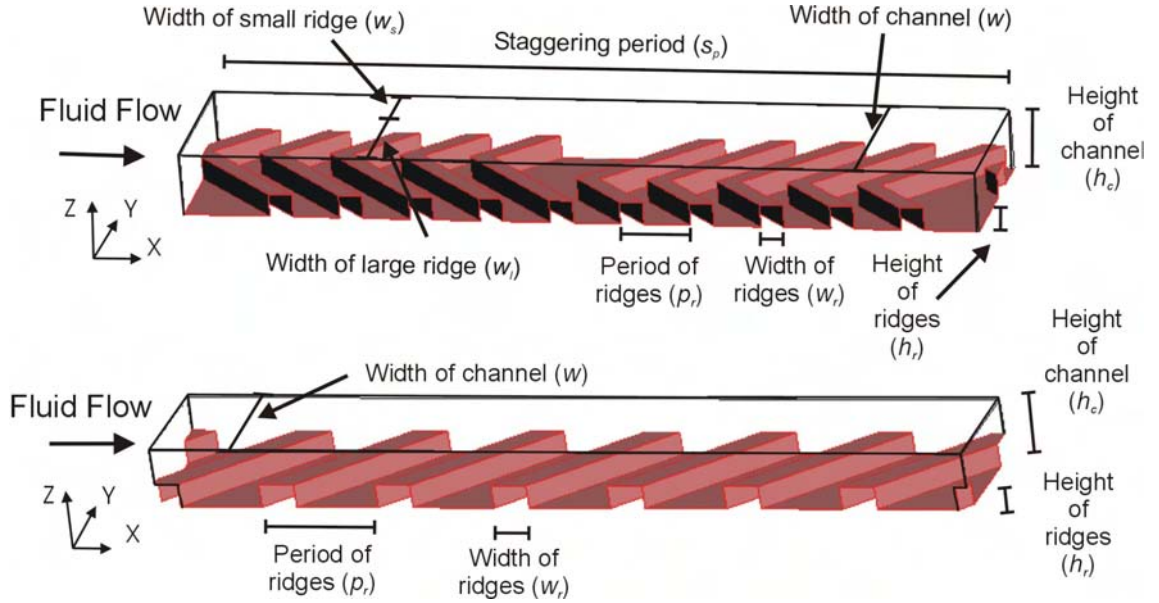
Figure 4.2: *Illustrations of staggered herringbone mixer (top) and diagonal mixer (bottom) with the different characteristic parameters for the systems sketched.*

angle of the velocity as used in [46]. In the simulations this number can be extracted by integrating the ratio of the velocities in a line just below the top surface (see Fig. 4.3). For SHM's two rotations are present, and this means that two planes and two lines have to be used, to evaluate both rotations (see Fig. 4.3).

4.3 Evaluation of calculational method

The simulations performed for the mixers were calculations of the fluid flow field in the channels. The simulations were performed using FEMLAB 2.3a, FEMLAB 3.0a and FEM-LAB 3.1. Some of the simulations were performed using periodic boundary conditions, which means that the flow profile output at one boundary is used as flow profile input for the opposite boundary. This means that the flow profiles at the two boundaries are identical when the simulation has converged, resulting in a simulation of a periodic infinitely long channel. In these simulations the flow rate was controlled by applying a pressure drop from the inlet to the outlet boundary. For the simulations without periodic boundary conditions a flow was given at the inlet boundary of the channel. For both types of simulations all boundaries except the inlet and outlet boundaries were set as no-slip boundaries.

I will start by presenting a few plots from the simulations of the flow in a diagonal mixer and a staggered herringbone mixer. This is to see what the flow field looks like, and whether rotations are present in the simulations, as has been shown in the literature (see Sec. 2.4). In Fig. 4.4 plots with vectors for the cross-sectional velocities can be seen. In these plots it is easy to see that one cross-sectional rotation is present in the flow field
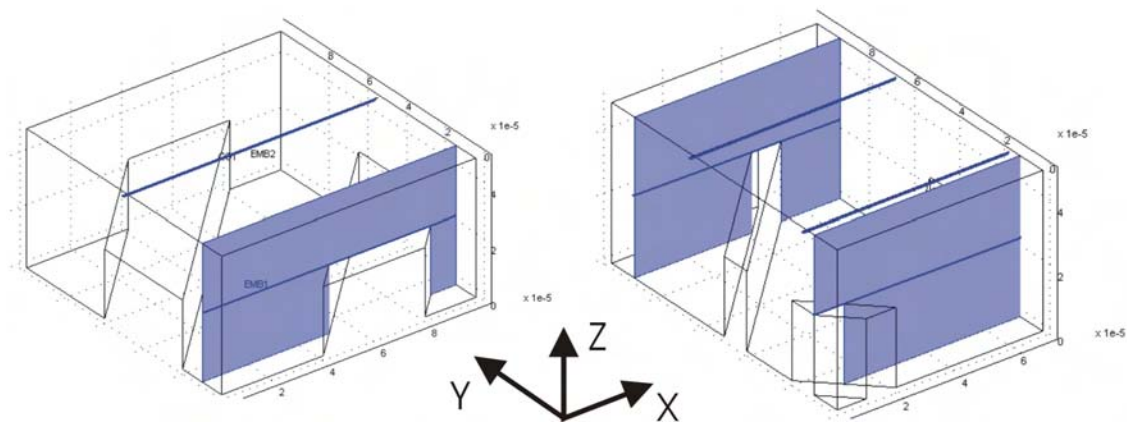
Figure 4.3: *In this figure planes and lines for evaluation of the magnitude of the cross-sectional rotations are shown. The lines are used for integrating (v_y/v_x) which should give me $\tan(\Omega)$ as used in [46]. They are placed 2% down in the channel. The planes are used for measuring the flux. They are divided into two, and two different methods have been used. Integrating $abs(v_y)$ over the whole plane or half the plane, and integrating (v_y) over half the plane. Both methods should give a flux through the plane, and the amount of water going in and out of this plane should be an indicator of the magnitude of the rotations. The planes are placed 10 μm into the channels that usually are 100 μm wide.*

for the DM. For the SHM two counterrotating rotations are seen. In Fig. 4.5 plots are presented that show that the distribution of the flow is greatly influenced by the period of the ridges.
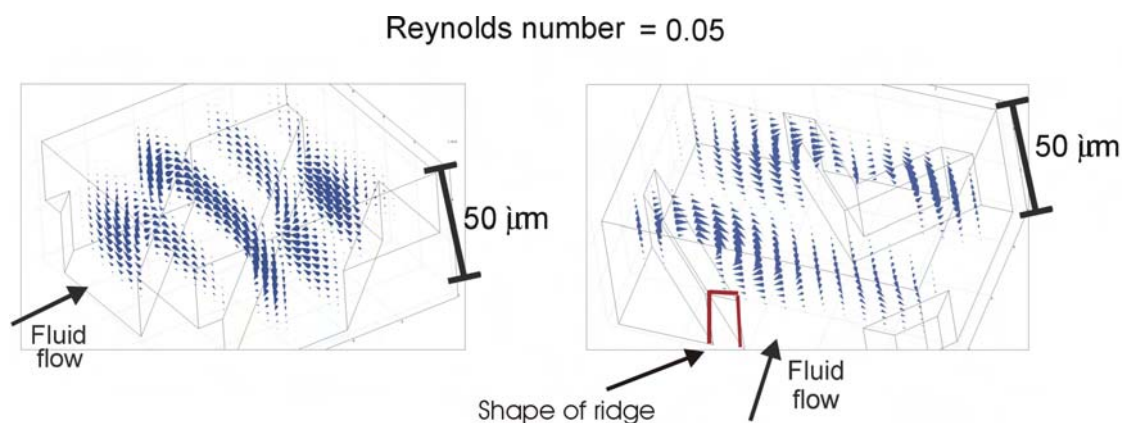
Figure 4.4: *Plots of the cross sectional parts of the velocity vectors (v_y and v_z). In these plots it is seen that one rotation is present in the DM (left) and two counterrotating rotations in the SHM (right). Both simulations were performed using periodic boundary conditions.*

To be able to trust the simulations, it is necessary to show, that they are comparable to

Reynolds number = 0.05

Figure 4.5: *Plots of the of the size of the velocity $(v_x^2 + v_y^2 + v_z^2)^{1/2}$ for two different simulations. Both channels are 50 μm high and 100 μm wide. For the left channel $p_r = 100 \ \mu m$ and for the right $p_r = 300 \ \mu m$. It is easy to see that for the left channel the flow is mainly in the top of the channel, whereas in the right channel the flow is distributed over the whole channel between the ridges.*
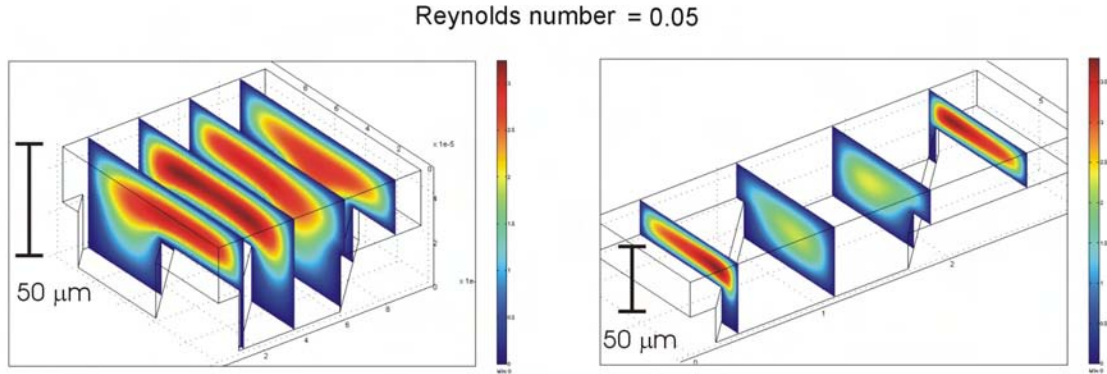
known results. Furthermore I want to make sure and that the mesh used is sufficiently fine to make the numbers extracted from the simulations independent of further refinement of the mesh. Also the different solvers used should have no influence on the result. Finally I needed to know whether the results are different for linear solving (Stokes) and nonlinear solving (Navier-Stokes) of the system.

The simplest simulation comparable to my system is that of a simple channel. A simulation with periodic boundary conditions was performed, and the velocity profile exported and compared to a plot of the analytical result for this geometry (see Eq. (3.8)). This comparison can be seen in Fig. 4.6. No exact analytical results are available for the flow field of DM's or SHM's but in the mask design structures were included to facilitate a comparison between simulations and actual experiments. This will be presented later in this chapter.

The next step was to make sure that the mesh was fine enough. This meant that refining the mesh further should not change the numbers extracted from the simulations. For this a number of simulations were performed. At the same time it was also tested whether the solver chosen affected the results. In Table. 4.2 extracted numbers from different calculations are presented. From the numbers I conclude that the mesh used is sufficient and that the solver type does not influence the results. The last row of numbers change a little bit, but only on the order of 1% which is far below the differences I am looking for. I also tried to vary the position of the line used to extract $\tan(\Omega)$. These results can be found in Table. 4.3. Both of these tests have been performed on several systems.
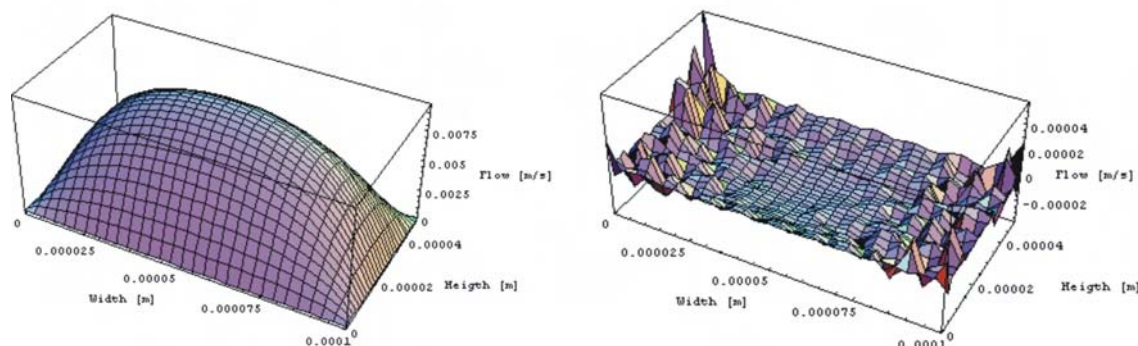
Figure 4.6: *To the left a graph of the flow profile in a simple rectangular channel. The dimensions are $w = 100$ μm and $h_c = 50$ μm and the flow rate is 1.44 $\mu L/min$. In the graph to the right the flow from a FEMLAB simulation is subtracted from the result from the analytical expression using Mathematica 5. As is seen the error is generally around three orders of magnitude smaller than the average velocity.*

FEMLAB solver	Number of elements	$\tan(\Omega)$	Flux through plane in m/s
UMFPACK nonlinear	5729	0.188	8.06×10^{-5}
SPOOLES nonlinear	5729	0.188	8.06×10^{-5}
SPOOLES nonlinear	9439	0.188	8.10×10^{-5}
SPOOLES linear	9439	0.188	8.10×10^{-5}
GMRES linear	12884	0.188	8.15×10^{-5}

Table 4.2: *Table showing the extracted numbers from simulations using different FEMLAB solvers and varying mesh fineness. The system was a DM with the parameter: $w = 100$ μm, $h = 50$ μm, $p_r = 85$ μm, $r_c = 0.5$, and $Re = 0.05$.*

Distance to top [μm]	0.2	0.5	1	2	5	10
$\tan(\Omega)$	0.189	0.189	0.188	0.187	0.181	0.167

Table 4.3: *Table showing the extracted numbers from the SPOOLES nonlinear simulation with 9439 elements from Table. 4.2. It is seen that the difference between 0.2 μm and 2 μm is very small.*

4.4   Diagonal mixers

Many different parameters have been investigated, but here I will only give a few important results from the simulations. These results can be seen as design rules for maximizing the magnitude of the rotations in the mixers.

The shape of the ridges is influenced by the fabricational method chosen. I therefore tested whether the shape of the ridges (see Fig. 4.4 for a sketch of what is meant by the

shape) has an influence on the magnitude of the rotations. If it turned out to play a major role it might be possible to choose a fabricational method to get close to the optimal shape whereas if the shape of the ridges only has a small influence the most convenient fabricational method could be chosen. In Fig. 4.7 graphs of the extracted numbers from the simulations are shown, together with drawings of the ridge shapes. From the graphs it is seen that the difference in the magnitude is small for most shapes, and that it is acceptable for the ridges to be a little tapered and the edges a little rounded. Triangular ridges, however, are not desirable.

A parameter that is easily controlled is the height of the ridges (h_r) compared to the height of the channel(h_c) $r_c = h_r/h_c$. This parameter has the largest influence on the magnitude of the rotations (see Fig. 4.7). This parameter, however, also changes many other characteristics for channel. Higher ridges greatly increase the hydraulic resistance as can be seen on the graph in Fig. 4.7 and objects like dust and other things tend to wrap around the ridges or getting caught in between them, making it difficult to keep the channel clean.
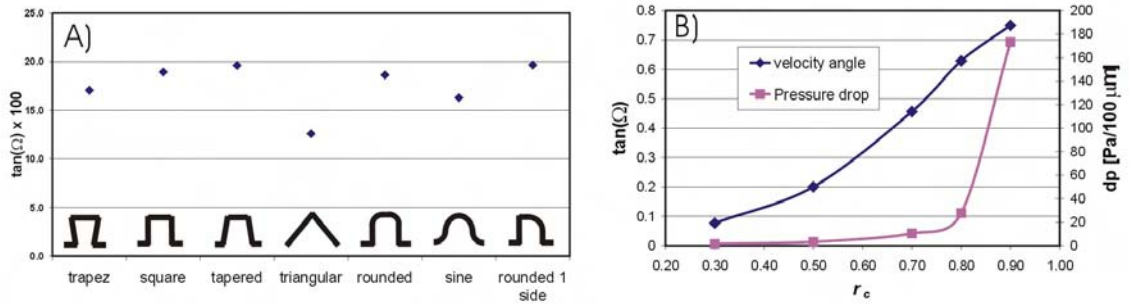
Figure 4.7: *Graphs of extracted numbers from two different series of simulations. In both cases $w = 100~\mu m$, $h_c = 50~\mu m$ and $Re = 0.05$. A) Here the shape of the ridges is varied and $p_r = 85~\mu m$. B) Here the height of the ridges is varied and $p_r = 100~\mu m$. This graph shows that the height of the ridges plays a very large role in the magnitude of the rotations, but also that the hydraulic resistance is changed even more than the magnitude of the rotations.*

The ratio between the width and height of the channel has also been investigated. This turned out to be an important parameter. Width:height ratios of 1:1, 2:1, and 4:1 were investigated. From Fig. 4.8 it is seen that for a ratio of 1:1 the magnitude of the rotation is less than half that for a ratio of 2:1. The magnitude of the rotation is almost the same for the ratios 2:1 and 4:1. In all these simulations the plane used to extract numbers has been placed 10 μm into the channel. This is because it is difficult to know which parameter should decide the placement of the plane. Height, width, or both. In the same figure a graph where $\tan(\Omega)$ is used as a measure is shown. This is a more simple way to evaluate the magnitude of the rotations. It is seen that using this method we reach the same conclusion as before. It is important that the channel is wider than it is high,

but making it more than twice as wide does not change the magnitude of the rotation noticeably.
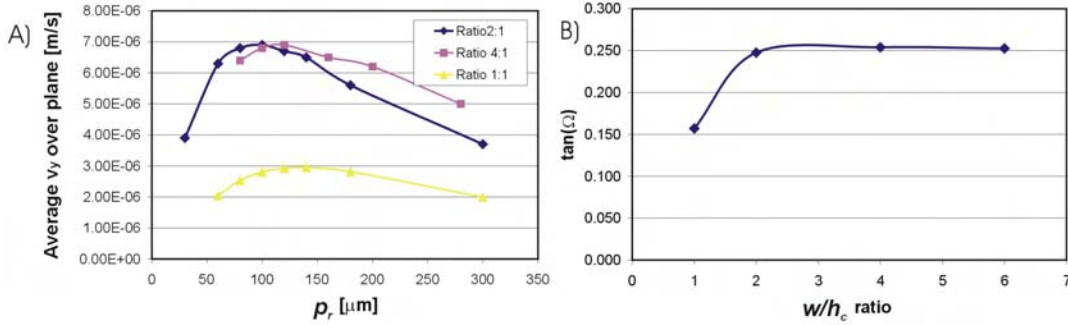
Figure 4.8: *Graphs of extracted numbers from simulations. $r_c = 0.5$ for all simulations. A) Ratio 1:1. $w = 100 \ \mu m$, $h_c = 100 \ \mu m$ and $Re = 0.01$. Ratio 2:1 $w = 100 \ \mu m$, $h_c = 50 \ \mu m$ and $Re = 0.005$. Ratio 4:1 $w = 200 \ \mu m$, $h_c = 50 \ \mu m$ and $Re = 0.005$. B) $h_c = 50 \ \mu m$, $p_r = 50 \ \mu m$, $w_r = 10 \ \mu m$, and $Re = 0.05$.*

In Fig. 4.9 a graph for three series of simulations is seen. For each series of simulations p_r is constant while w_r and hence $r_p = w_r/p_r$ is varied. From the graphs it is possible to see that the period of the ridges (p_r) can be optimized. It is also seen that the width of the ridges (w_r) should be chosen to be as narrow as is allowed by the fabrication sequence and the strength of the materials used. When w_r has been chosen a series of simulations should be performed to optimize p_r.
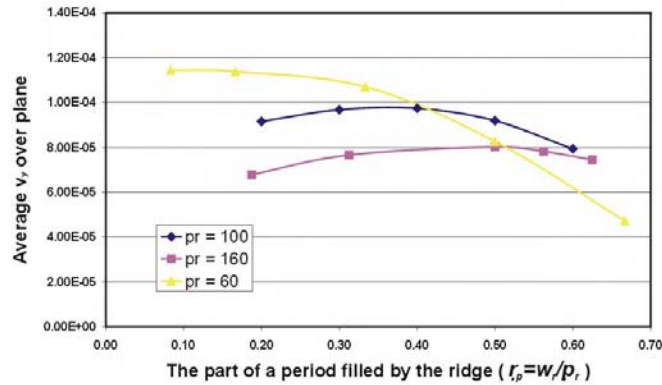
Figure 4.9: *A Graph with extracted numbers from three different series of simulations. $r_c = 0.5$, $w = 100 \ \mu m$, $h_c = 50 \ \mu m$, $Re = 0.05$ and $w_r = 10 \ \mu m$ for all simulations. It is seen that the magnitude of the rotations is significantly larger for short periods p_r and small w_r. Thus the optimum w_r is limited by the resolution of the fabrication technique.*

Figure 4.10: *Two graphs with extracted numbers from different series of simulations. $r_c = 0.5$, $w = 100$ μm, $h_c = 50$ μm and $Re = 0.05$ for all simulations. A) A series of simulations for a DM compared to two different series of simulations for SHM's. It is seen that for $a_s = 0.5$ the magnitude of the rotations is almost identical. For $a_s = 0.4$ the magnitude of the large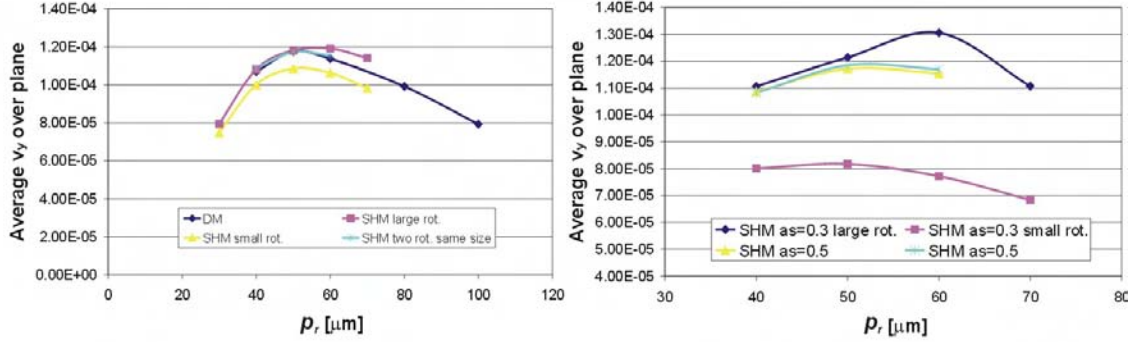 and the small rotation differs slightly, but is still very close to the magnitude of the rotation for the DM. B) Two series of simulations for SHM's compared. One for $a_s = 0.5$ and one for $a_s = 0.3$. It is seen that for for $a_s = 0.5$ the magnitude of the two rotations is the same (as it should be). For $a_s = 0.3$ the difference in magnitude between the two rotations becomes fairly large. The small rotation becomes a lot weaker while the large rotation only becomes a little bit stronger. It is also seen that optimum p_r is not the same for the large and small rotations.*

4.5 Staggered herringbone mixers

Some simulations performed for SHM's have been designed to be comparable to some of the simulations performed for DM's. In Fig. 4.10 two series of simulations for SHM's are compared to a series of simulations for DM's. The difference between the two SHM simulations is a parameter I call the asymmetry parameter (a_s) which is a parameter describing how large a part of the channel is filled by the small rotation ($a_s = w_s/w$). When a_s has a value of 0.5 the two rotations are equally wide, and the smaller a_s is, the larger the difference in size of the two rotations. In Fig. 4.10 it is seen that for $a_s = 0.5$ the magnitude of the rotations are almost identical to the magnitude of the rotation for the DM, and they have an optimum for the same parameters. This indicates that the influence of the different parameters are the same for DM's and SHM's and hence that the design rules for the DM's also apply for the SHM's. The model presented in Sec. 4.1, however, showed that the two kinds of mixers could not depend on the width height ratio in the same way. I will get back to that shortly. In Fig. 4.10 it is also seen that when the difference in size of the two rotations becomes large, the small rotation becomes weaker and the large rotation becomes a little stronger. The optimum p_r also becomes different for the small and large rotation. This agrees very well with the model presented in Sec. 4.1, and means that for mixing to be effective the difference in size must not be too large.

The initial assumption was that the influence of different parameters on the magnitude

of the rotations would be comparable for DM's and SHM's, and this is supported by Fig. 4.10. This would mean that the extensive investigation of the DM's would not have to be repeated. One could speculate though that wider channels would be necessary since two rotations are present, and hence the width to height ratio is smaller for each rotation than if only one rotation was present. It was not possible to conclude that this was the case from the model presented in Sec. 4.1. However, this is the effect seen from the graph in Fig. 4.11.

In Fig. 4.10, however, very similar results are seen for the SHM and DM mixer with a w/h_c ratio of 2. This is in contrast with Fig. 4.11. The reason for this is that two different evaluation methods are used. In Fig. 4.11 the magnitude of each rotation at its center is evaluated whereas the flux close to the sidewalls is evaluated in Fig. 4.10. As presented in Sec. 4.1 the flux close to the sidewalls will be larger for the SHM than for the DM if the rotations are of the same magnitude. This actually means that even though the overall rotations achievable are of the same magnitude, a greater flux close to the sidewalls of the channel can be created with the SHM.
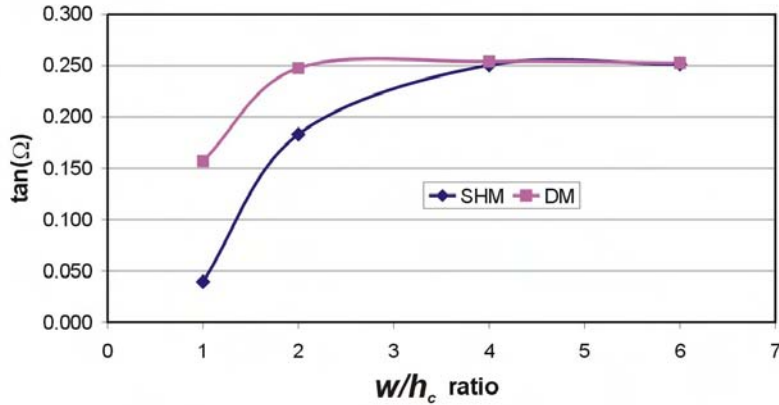
Figure 4.11: *A graph with extracted numbers from a series of simulations for an SHM and a DM. For both $r_c = 0.5$, $h_c = 50$ μm, $w_r = 10$ μm, $p_r = 50$ μm and Re $= 0.05$. For the SHM $a_s = 0.5$. In the simulations only the width of the channel is varied.*

4.6   Choice of mixer

A choice of mixer for the systems had to be made. To make this choice I needed to keep in mind the purpose of the mixer. I wanted the mixer to bring as many beads as possible close to the sides of the channel where the beads are caught. From the above examples it is easy to see that this goal is best reached with an SHM as long as the channel is at least twice as wide as it is high. Furthermore the secondary functionality that the mixer introduces to my system, which is mixing of fluid is far more effective for the SHM than for the DM [46]. My choice fell on an SHM.

In the theoretical investigation of the mixers I have only investigated the magnitude of the rotations. I have not had a way to asses the mixing efficiency and therefore there are some parameters I have not investigated that influence the mixing efficiency and hence cannot optimize. This is the staggering period (s_p) and the asymmetry of the rotations (a_s). a_s has been investigated, but only with respect to the magnitude of the rotations and not with respect to the mixing efficiency. In the literature the only choice for a_s has been 0.33, which means that the small rotation is exactly half the size of the large rotation. In my simulations, however, I saw that the small rotation becomes a bit weaker than the large rotation. I chose to use a value of 0.35, partly for practical reasons and partly for the reason mentioned above. For s_p I chose that corresponding to 10 ridges (5+5).

On the wafer I decided on having three different channel widths (100, 200 and 400 μm). At the time of mask designing I had not yet decided which heights of channels and ridges I would use, so it was not possible to optimize the magnitude of the rotations. The other parameters chosen for the mixers were $w_r = 30$ μm, and $p_r = 90$ μm. h_c and h_r can be varied without designing new masks. In the systems fabricated in this project the parameters are $h_c \approx 80$ μm, and $h_r \approx 30$ μm.

4.7 Flow field experiments

As mentioned earlier, simulations and experiments were performed that were directly comparable. This was to show that the mixer works and to facilitate a comparison. The experiments were performed on the systems with two inlets. Through one inlet water with fluorescein was introduced, and through the other inlet a buffer was introduced. Experiments were performed for a system with and a system without integrated microfluidic mixer, and for a range of flow rates in both cases. For all the experiments shown the ratio between dyed and clean water was 3:10.

4.7.1 Flow without mixer

In Fig. 4.12 micrographs for experiments on a system without integrated mixer are seen. The experiments show that the mixing is very limited. At a flow rate of 8.67 μL/min and 17.3 μL/min the interface is a little fuzzy due to diffusion, but at 65 to 87 μL/min it becomes quite sharp. Around a flow rate of 1300 μL/min, which roughly translates to a Reynolds number of 100, it is seen that some sort of rotations in the fluid flow must appear, since the florescent dye spreads out into the channel. This is due to the inertia term becoming larger with larger Reynolds number.

4.7.2 Flow with mixer

Micrographs from similar experiments on a system with integrated mixer are seen in Fig. 4.13. From these micrographs it is easy to see that the mixing of the two fluids is much more effective. It is also seen that at low Reynolds numbers the micrographs do not change significantly with the flow rate. This means that the nonlinear term of the Navier-Stokes equation, which is dependant on the inertia of the fluid, is negligible. Around a
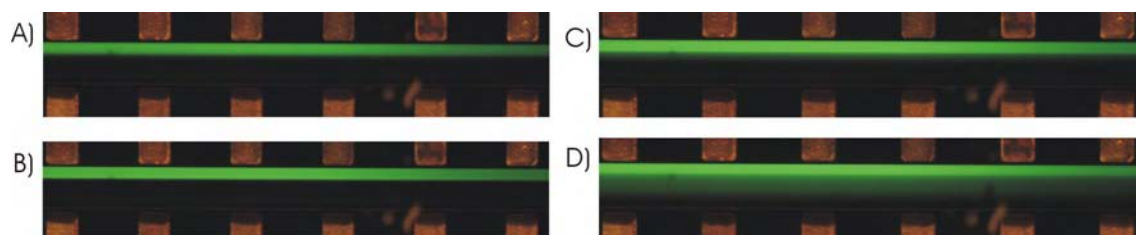
Figure 4.12: *Micrographs from experiments with different flow rates on 200 µm wide system without mixer. The ratio between dyed water and buffer is 3:10. Micrographs are taken from magnetic element 14 to 19, which means it is a little further than halfway down the channel. A) Flow rate= 17.3 µL/min. B) Flow rate= 86.7 µL/min. C) Flow rate= 1730 µL/min. D) Flow rate= 3460 µL/min. In A) the interface is a little fuzzy because of diffusion whereas the interface seems quite sharp in B). In C) the first signs of a spreading of the green shine in the channel is seen and in D) it is even more evident.*

flow rate of 170 µL/min, which roughly translates to a Reynolds number of around 15, the micrographs start changing which means that the nonlinear term starts to play a role. At a flow rate of around 800 to 1700 µL/min (Re=70 to 140) the inertia term is so large that rotations in the fluid flow enhances the mixing.
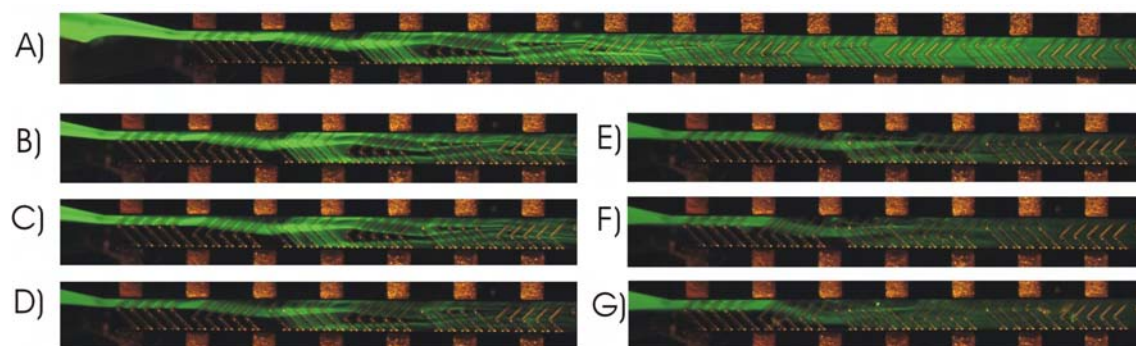
Figure 4.13: *Micrographs from experiments with different flow rates on 200 µm wide system with mixer. The ratio between dyed water and buffer is 1:3.33. The micrograph in A) shows the first 14 elements of the channel, which means the first half of the channel, while B)-G) shows the first 7 elements (1/4 of the channel). A) Flow rate= 8.67 µL/min. B) Flow rate= 17.3 µL/min. C) Flow rate= 86.7 µL/min. D) Flow rate= 260 µL/min. E) Flow rate= 866 µL/min. F) Flow rate= 1730 µL/min. G) Flow rate= 2600 µL/min. When comparing A) to the micrographs in Fig. 4.12 it is seen that the SHM greatly enhances mixing. B) and C) are almost identical, and a small change can be seen in D) indicating the influence of the nonlinear term in the Navier-Stokes equation. The change is much more evident in E) and in F) and G) signs of turbulence can be seen.*
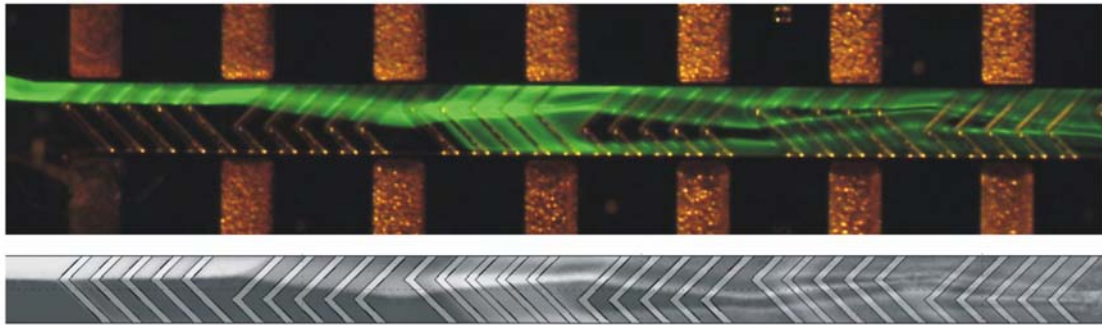
Figure 4.14: *Micrograph (top) and simulation (bottom) of the fluid flow in a system with a microfluidic mixer. The flow rate in the experiment was = 8.67 µL/min and the ratio between dyed water and buffer is 1:3.33. The plot from the simulation is a little blurry in places because it is made up of several plots put together and on top of each other.*

4.7.3 Comparison to simulation

In Fig. 4.14 micrographs from the experiment is compared to plots from a simulation of a matching channel. In the simulation the flow was solved using the Navier-Stokes equation. This solution was stored and used for a convection-diffusion problem where dyed water (water with a concentration of some chemical) and clean water were introduced to the channel. As is seen when comparing the plots with the micrograph the simulation and the experiment are almost identical. This means that the simulations are in at least qualitative agreement with the experiments.

4.8 Summary

In this chapter a simplified model for the working principle of the mixers was presented. This was used to explain results from the simulations.

Simulations were performed, and different ways to verify the simulations were applied. These included comparison to an analytical result and an experiment.

From the simulations some general design rules were deduced for optimizing the magnitude of the rotations, when designing DM and SHM mixers. It was concluded that:

• By far the most important factor was the height of the ridges compared to the height of the channel. High ridges however gave an even larger increase in hydraulic resistance, and this should be taken into account when designing the mixer.

• The width of the channel should be be around two or more times the channel height

• The width of the ridges should be chosen as narrow as possible. This maximizes the transverse velocities and minimizes R_{hyd}.

• An optimization of the period should be performed with the width of the ridges and the height and width of the channel chosen.

4.9   Discussion

The fluidic simulations presented in this chapter were only compared to one experiment. To prove that the simulations show the actual influence of the parameters further experiments are necessary. For this purpose a range of diagonal mixers, varying a parameter I have varied in the simulations, should be fabricated. A measurement of the angle of a dyed fluid being pressed from one side of the channel to the other under the top surface could be measured ([46]). This can be compared directly to my simulations.

The simulations performed were used only for maximizing the magnitude of the rotations. A point was reached, though, where it would be possible to asses the influence of parameters like the staggering period or the asymmetry of the herringbones on the mixing efficiency. This could be done using either colored particle tracking ([30]) or the convection/diffusion simulations performed in this project using FEMLAB. These simulations could be compared to experiments like the one performed in this project. Another way to to asses the mixing efficiency experimentally is to use a chemical reaction creating a fluorescent or colored product (as in [31]).

Chapter 5

Magnetic field from soft magnetic elements

When designing systems like the magnetic separation systems presented in this project, it is important to understand the physics behind the system. As the name indicates the working principle of the system depends on magnetism, and since all currents and fields are constant, the theory behind it is magnetostatics.

In this chapter I will present the magnetostatics theory and apply it to my systems. I will also write about different magnetic materials and in particular the ferromagnetic materials used for the magnetic elements. The last subject I present is the influence of geometry on the magnetic properties of an object. The topics presented determine the magnetic properties of objects, and I relate them to my system, to asses the influence.

Simulations on magnetic systems were also performed but as I write in the last section, what decided the magnetic structure in the end was a practical issue.

5.1 Magnetostatics

The magnetic separation in my systems depend on magnetic elements being magnetized by a homogeneous external magnetic field. This creates gradients in the magnetic field, and the magnetic beads are attracted towards the regions of high magnetic field. There are many different aspects to this kind of system. I need to understand the theory behind it and to do so I start out with Maxwell's equations. In the following subsections I will introduce magnetic materials and use this to discuss the materials used for the magnetic elements and the magnetic beads. Also I will consider geometrical effects affecting the magnetization of the magnetic elements.

5.1.1 Magnetostatic Maxwell's equations

In the case of magnetostatics all currents and fields are constant, which means that all time derivatives are zero. With this assumption the magnetic field is independent of electrical fields, and the magnetostatic Maxwell equations are given as:

$$\boldsymbol{\nabla} \times \mathbf{B} = \mu_0 \mathbf{J} \tag{5.1}$$

$$\boldsymbol{\nabla} \cdot \mathbf{B} = 0 \tag{5.2}$$

where $\mathbf{B}$ is the magnetic flux density, μ_0 is the vacuum permeability, and $\mathbf{J}$ is the total current density. It is possible to introduce a vector potential such that $\mathbf{B} = \boldsymbol{\nabla} \times \mathbf{A}$. This means that Eq. (5.2) is automatically fulfilled since the divergence of a curl is always zero, and then Eq. (5.1) could be used for calculating $\mathbf{B}$ [24]. In my special case, however, the problem can be reduced. I will get back to that later.

From Eq. (5.1) it is seen that the magnetic field is created by currents represented by $\mathbf{J}$. A current again is created by moving charges which usually are electrons. A current of electrons running in a conductor or a beam of electrons is called a free current and it is represented by the free current density ($\mathbf{J}^f$). Most electrons in materials move around a specific nucleus (to which it is bound) and hence do not cause a net flux of electrons. This is what is called a bound current and it is represented by the bound electrical current density ($\mathbf{J}^b$). This means that

$$\mathbf{J} = \mathbf{J}^f + \mathbf{J}^b \Rightarrow \boldsymbol{\nabla} \times \mathbf{B} = \mu_0(\mathbf{J}^f + \mathbf{J}^b) \tag{5.3}$$

Then the two contributions to $\mathbf{B}$ are defined as the magnetic field strength ($\mathbf{H}$) coming from the free currents and the magnetization ($\mathbf{M}$) coming from the bound currents. That gives

$$\boldsymbol{\nabla} \times \mathbf{H} = \mathbf{J}^f \ , \ \boldsymbol{\nabla} \times \mathbf{M} = \mathbf{J}^b \qquad \Rightarrow \qquad \mathbf{B} = \mu_0(\mathbf{H} + \mathbf{M}) \tag{5.4}$$

Using the relationship between $\mathbf{H}$ and $\mathbf{M}$ two new parameters are defined. They are both dimensionless.

$$\chi \mathbf{H} = \mathbf{M} \qquad \text{and} \qquad \mu_r = 1 + \chi \tag{5.5}$$

The magnetic susceptibility (χ) is usually a tensor, and therefore also the relative permeability (μ_r) is a tensor. However, if $\mathbf{M}$ always is parallel or antiparallel to $\mathbf{H}$, χ can be treated as a scalar variable, and the material is called a linear material. The materials used in this project were all linear materials. For this case I can rewrite Eq. (5.4) to

$$\mathbf{B} = \mu_0(\mathbf{H} + \chi \mathbf{H}) = \mu_0(1 + \chi)\mathbf{H} = \mu_0 \mu_r \mathbf{H} \tag{5.6}$$

This gives me a simple relation between $\mathbf{B}$ and $\mathbf{H}$ if χ, and hence μ_r, is known. Generally χ depends on $\mathbf{H}$, but it is usually constant for low magnetic fields. It is a measure of how strongly a material responds to an applied magnetic field. Below I will suppress the dependance of χ on $\mathbf{H}$ in the notation.

In my case this relationship makes the calculations much easier. As no free currents are present in my system $\boldsymbol{\nabla} \times \mathbf{H} = 0$, and I can define a scalar magnetic potential, φ_m, fulfilling

$$\mathbf{H} = -\boldsymbol{\nabla}\varphi_m \tag{5.7}$$

If Eq. (5.2), Eq. (5.6), and Eq. (5.7) are combined, I get the following equation to be solved:

$$-\mu_0 \boldsymbol{\nabla} \cdot (\mu_r \boldsymbol{\nabla}\varphi_m) = 0 \tag{5.8}$$

5.1.2   Magnetic materials

In the previous subsection I mentioned that magnetic fields are created by currents, and that electrons move around the nucleus of atoms, thus creating a magnetic moment ($\mathbf{m}$).

$$\mathbf{M} = \frac{\mathbf{m}}{\mathrm{V}} \tag{5.9}$$

where V is the volume. Also the presence of a magnetic field affects moving electrons, and since all materials contain atoms this means that all materials have some kind of magnetic behavior.

Diamagnetism and paramagnetism

Most of the electrons in an atom move in such a way as to cancel out each others magnetic moments. If no unpaired electrons are present the result is what is called a diamagnetic material. In Fig. 5.1 a schematic curve for the magnetic behavior of a diamagnetic material in a magnetic field is shown. From this curve it is seen that the magnetization of a diamagnetic material is oppositely directed to the magnetic field. This is a quantum effect, but can also be explained with a simplified model of the interaction between a magnetic field and an electron moving in a circle perpendicular to the direction of the magnetic field (this represents the orbital spin of the electrons). If the motion is one way round the magnetic force the electron will make the radius of the circle smaller and if it moves the other way round it will make the radius larger. This gives a small change in the magnetic moment created by the two electrons resulting in an effective magnetic moment pointing in the opposite direction of the magnetic field [24]. This effect is experienced by all materials, but is very small with χ typically around -10^{-5} [27].

If unpaired electrons are present in the material they each give a permanent magnetic moment. In the presence of an external magnetic field the amount of small magnetic moments aligned with the magnetic field becomes larger than the amount aligned opposite to the magnetic field, and thus the magnetic field is enhanced [24]. A schematic curve for the magnetic behavior of a paramagnetic material in a magnetic field is shown in Fig. 5.1. This effect too is very small with typical values of χ around 10^{-5} to 10^{-3} [27].

Ferromagnetism

The two kinds of magnetic behavior explained are weak effects and the magnetization disappears when no external magnetic field is present. Materials showing stronger magnetic effects that can also exist independently of an external magnetic field however. There are
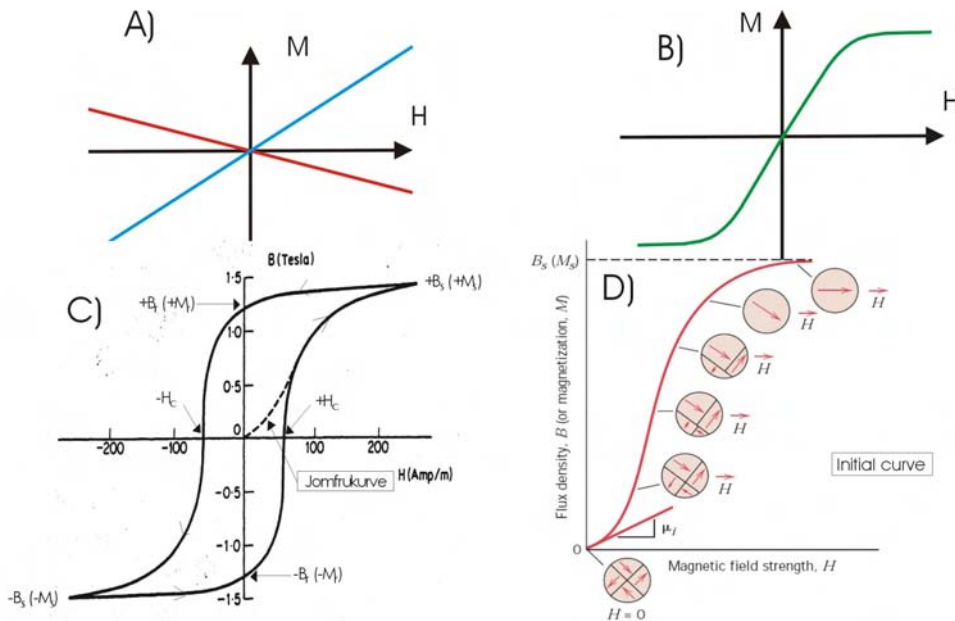
Figure 5.1: *A) A schematic of the magnetic behavior of diamagnetic (red), paramagnetic (blue) materials in an external magnetic field. B) Schematic representation of superparamagnetic material in an external magnetic field. B) Schematic of the initial magnetization curve for a typical ferromagnetic material. Domain sizes and orientations are sketched and the slope of the curve at the beginning describes the initial permeability. C) An example of a hysteresis curve for a ferromagnetic material. the maximum permeability is the slope of the curve at $\pm H_c$.*

different behaviors but here I will concentrate on the magnetic behavior called ferromagnetism.

The reason why paramagnetism is a weak effect is that even though some of the magnetic moments align to the external magnetic field it is far from all. They are independent of each other. In ferromagnetic materials the small magnetic moments interact so strongly that locally nearly 100% are aligned [24]. A ferromagnetic body below its Curie temperature will tend to be divided into magnetic domains. In each domain all the atomic moments are parallel, but the domains will be magnetized in different directions, to minimize the magnetization of the body. If placed in a magnetic field the domains aligned with the magnetic field will start growing at the expense of other domains, and an effective magnetic moment of the object is the result (an illustration of this effect can be seen in Fig. 5.1). If the magnetic field is strong enough the domains will all be aligned, and the material is said to be saturated. If the magnetic field is turned off some of the domains will return to random orientation, but not all (the ratio of domains that stay aligned depend upon the material and the geometry of the object). This means that a magnetization of the object is sustained independently of the magnetic field. This is called the remanent magnetization (M_R) or remanence (B_R). This remanence can be removed by applying a magnetic field

in the opposite direction. The magnetic field strength necessary to remove the remanence is called the coercive field (H_c). A schematic of a hysteresis curve, where a ferromagnetic material is magnetized to saturation in first one direction, then the other direction, and back to the first direction again, is shown in Fig. 5.1. A few more parameters are also presented. The loop created by this curve is called a hysteresis loop. The ferromagnetic effect is much stronger than the diamagnetic and the paramagnetic effect typically having values of χ around 50-10000. [27]
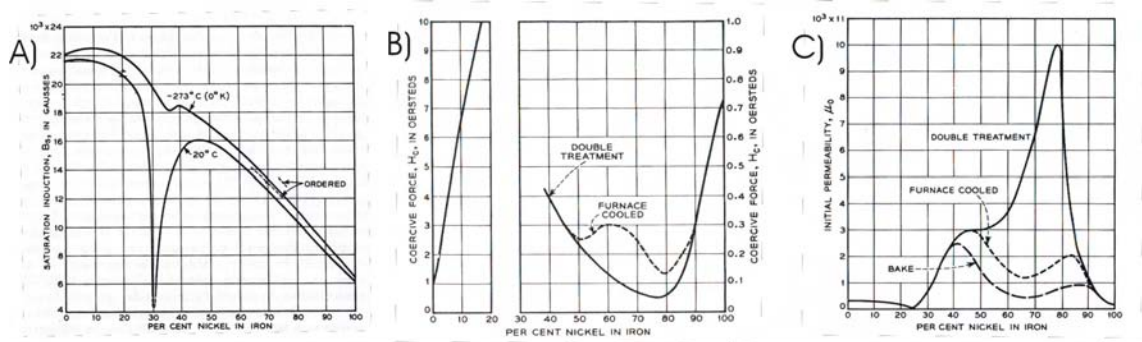

Figure 5.2: *Parameters for permalloy as a function of composition [11].*

The parameters described vary from material to material, and in my systems I want magnetic elements that are easy to magnetize, and once the external magnetic field is turned of they should demagnetize. This means that I want the remanent magnetization and the coercive field to be low, and the magnetic susceptibility and the saturation magnetization to be high. Materials with a coercive field off less than 1000 A/m are called soft ferromagnetic materials, so this is the group of magnetic materials I should be looking at. The material I am working with is called permalloy. Permalloy is an alloy of nickel and iron. In Fig. 5.2 measurements of initial and maximum permeability, coercive force, and saturation magnetization are presented as a function of composition [11]. These parameters however are not only a function of the composition but also of other parameters like the amount and nature of defects in the crystal structure. For me this means that electroplating conditions could have an effect on the properties of the electroplated material other than the composition.

From the graphs it is seen that the properties I want from the material are best reached with a composition of around 20% iron and 80% nickel.

Superparamagnetism

When the size of an, e.g., ferromagnetic object is reduced, at one point it will become so small that it can sustain only one domain. This is because magnetic domains are separated by domain walls, and domain walls cost energy to sustain. On the other hand large domains also cost energy to sustain, and the size of magnetic domains is governed by these two effects.

If a single domain magnetic particle has a preferred magnetization axis, it can be

magnetized in both directions along this axis. These two states are separated by an energy barrier since for all intermediate states the net magnetization is not along the preferred axis and hence have higher in energy. As the particle size is reduced this energy barrier becomes smaller. this is since the particle only has a single domain and hence all the small magnetic moments have to be turned at the same time. The smaller the particle the fewer small magnetic moments giving a lower barrier. At some point the energy barrier reaches a size where it is comparable to the thermal energy, and at this point it becomes what is called superparamagnetic. The diameter at which a particle becomes superparamagnetic is usually in the order 5 to 10 nm [25].

A superparamagnetic particle has no magnetic remanence, since the thermal energy is enough to flip the magnetization of the particle. This means that as the external magnetic field is removed, thermal energy will make the magnetic moment of the particle flip around, and the average magnetic moment will be zero. While the superparamagnetic particles are in an external magnetic field their magnetic moments will tend to align to the external field resulting in a large magnetic response. In Fig. 5.1 a sketch of superparamagnetic response in an external magnetic field.

5.1.3   Geometry effects

It is not only the choice of magnetic material that is important for the magnetic properties of an object. The geometry of the created structures also plays a major role on how easily a structure is magnetized, and on the size of the remanent magnetization. This is due to an effect called the demagnetization effect.

I start by presenting a sketch of a magnetized body (see Fig. 5.3).

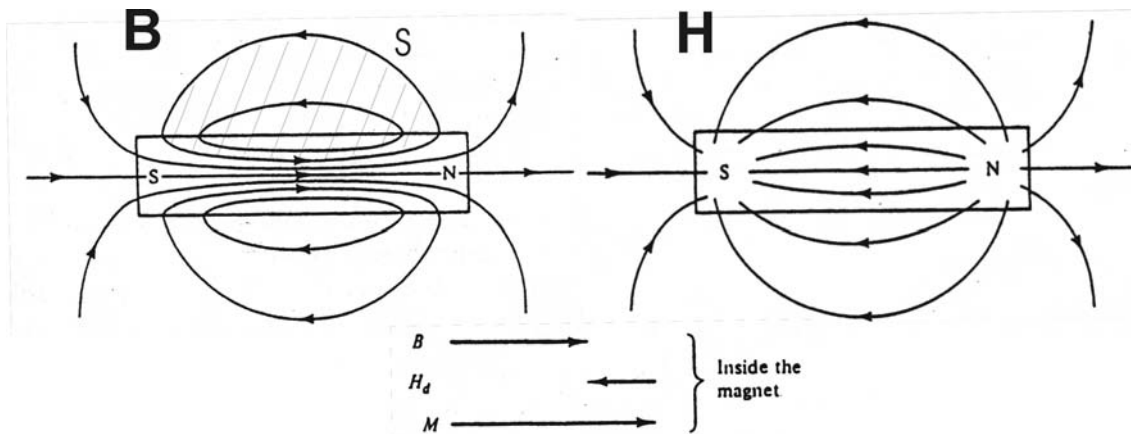Figure 5.3: **B**-*field and* **H**-*field inside and outside a permanently magnetized object [37]. A surface S is marked as a hatched area*

It is seen that the field lines from the magnetic field strength and the magnetic flux density have the same direction outside of the magnet, but not inside [27]. It comes readily from Eq. (5.4) that since no magnetized material is present outside the magnetized

body, the magnetic flux density and the magnetic field strength are pointing in the same direction.

Since no free currents are present $\boldsymbol{\nabla} \times \mathbf{H} = 0$. If I use the curl theorem on this equation I get

$$\int_S \boldsymbol{\nabla} \times \mathbf{H} \cdot d\mathbf{a} = \oint_P \mathbf{H} \cdot d\mathbf{l} = 0 \tag{5.10}$$

Where S is the hatched surface in Fig. 5.3. P is the perimeter of S. The integral along P outside the material gives a positive contribution. Thus in order to satisfy Eq. (5.10) the integral along P inside the material must be negative. This shows that $\mathbf{H}$ has a composant in the opposite direction to $\mathbf{M}$ inside the material. The field inside the material is called the demagnetization field and is given as [27]

$$\mathbf{H}_d = -N_d \mathbf{M} \tag{5.11}$$

Where N_d is a tensor called the demagnetization tensor. From Fig. 5.3 it is seen that the field lines between the two poles are not limited to be inside the magnet. The longer and thinner the magnet on the picture would be, the smaller the demagnetizing field inside the magnet would be. In the extreme cases we have an infinitely long rod that a demagnetizing factor of zero in the long direction and an infinite plate that has a demagnetization factor of one in the direction normal to the plate. From this it follows that the demagnetizing field must depend on both the Magnetization and the geometry of an object.

N_d is only well defined for uniformly magnetized geometries like ellipsoids, infinite rods, and infinite plates. For these geometries it can be shown that the trace of the demagnetization tensor is one. For other geometries approximated values of the demagnetization tensor can be obtained [37]. In Table. 5.1 I have listed some demagnetizing factors. It is seen that for large dimensional ratios the demagnetization factor is small along the long axis.

In my systems I have magnetic elements that are magnetized by an external field, so I want to know what the demagnetizing field means in this case. I apply an external magnetic field with magnetic field strength $\mathbf{H}_{app}$. This gives rise to a magnetization in the same direction as the applied field. The induced magnetization in return gives rise to a demagnetizing field in the opposite direction inside the magnetic element, with magnetic field strength $\mathbf{H}_d$. The magnetic field strength inside the magnetic element ($\mathbf{H}_{in}$) becomes

$$\mathbf{H}_{in} = \mathbf{H}_{app} + \mathbf{H}_d = \mathbf{H}_{app} - N_d \mathbf{M} \tag{5.12}$$

The magnetization is related to the magnetic field strength, and the magnetic field strength inside the magnetic element is large if the demagnetization factor is small. Inserting Eq. (5.12) into $\mathbf{M} = \chi \mathbf{H}$ and rewriting a little, I get

$$\mathbf{M} = \chi(\mathbf{H}_{app} - N_d \mathbf{M}) = \frac{\mathbf{H}_{app}}{\frac{1}{\chi} + N_d} \tag{5.13}$$

From this equation it is seen that as long as $N_d \gg \frac{1}{\chi}$ the demagnetization factor and not the susceptibility of the material controls the magnetic response of an object and hence

how easy it is to magnetize. In Table. 5.1 a number of demagnetization factors are listed. If the demagnetization factor for a structure with a dimensional ratio of around 50 is used in Eq. (5.13) it is seen that the difference in how easily the object is magnetized for a material with $\chi = 5000$ and $\chi = 10000$ is very small. In Fig. 5.4 the effect of demagnetization on a hysteresis curve is shown. From these graphs it is seen that the remanent magnetization becomes lower when the demagnetization effect starts to play a role. This means that since I want the magnetic elements to demagnetize when the external field is turned off, it might be advantageous to create structures with demagnetization factors only so low that I am almost able to saturate the magnetic elements. In our case

$$N_d \approx \frac{H_{app}}{M} \approx \frac{50 \text{ mT}}{1 \text{ T}} = 0.050 \tag{5.14}$$

This would give almost saturated magnetic elements with low remanence.

Dimensional ratio (**Length/Diameter**)	0	1	2	10	50	200	500
N_d **rod**	1	0.27	0.14	0.017	0.0013	0.000090	0.000014
N_d **prolate ellipsoid**	1	0.33	0.17	0.02	0.0014	0.00013	0.000024
N_d **oblate ellipsoid**	1	0.33	0.24	0.07	0.015	0.0039	0.0016

Table 5.1: *Table of demagnetization factors for different shapes and dimensional ratios [11].*

Eq. (5.13) has implications for magnetic measurements. If I believe that χ of a material I want to measure is around 10000 and look in Table. 5.1, it is seen that I need a structure with a dimensional ratio of at least around 500 for $\frac{1}{\chi}$ to be much larger than N_d and hence control the magnetization.

5.2   Summary

In this chapter the theory of magnetostatics was used to investigate the magnetic part of the systems. Many issues were raised, but when I decided on the magnetic structure to use, it was based on experience. I was working with a test mask, and during this time problems with the electroplating of magnetic elements were experienced. I therefore chose the structure that gave fewer problems.

However, the theory in this chapter has given me an understanding of the issues involved and I will be able to use this when new masks are to be designed. Also some of the theory has been used to design test structures.

 • when a material for the magnetic elements is chosen, a material with very low coercivity, and a high magnetic susceptibility is wanted. Here permalloy was chosen which is an alloy of Ni and Fe. The best composition of this alloy for my purpose is around 20% Fe and 80%Ni.
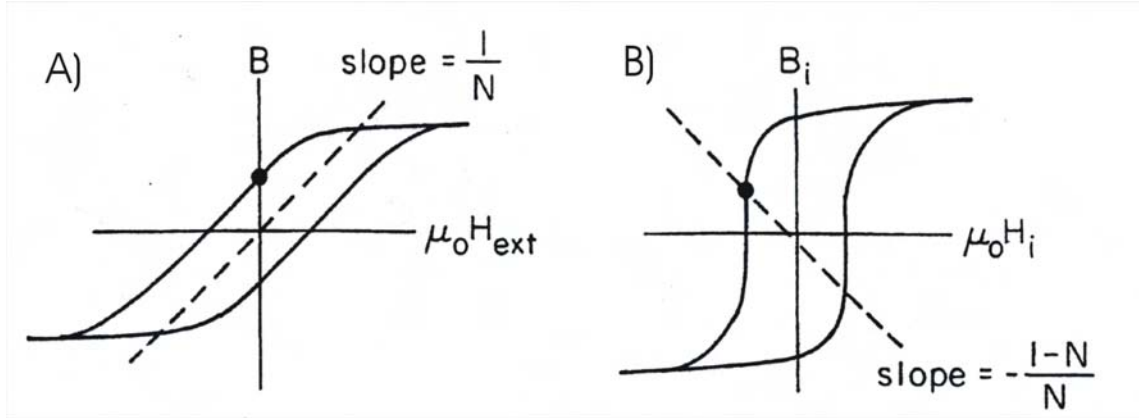
Figure 5.4: *Schematic representation of demagnetization effect on A)* **B-H**$_{app}$ *loops and B)* **B-H**$_{in}$ *loops. The dashed line lines rotated into the into the vertical axis in each case relate one loop to the other. It is seen that the demagnetization effect lessens the remanence [37].*

• When designing the magnetic structures the demagnetization factor should not just be minimized carelessly. A larger demagnetization factor gives a lower remanent magnetization but makes it harder to magnetize the object (see Fig. 5.4). A compromise should be found as described.

• For measurements of magnetic susceptibility of a material long thin elements are needed.

• For measurements of the saturation magnetization a thin square can be used. From this an approximate composition and a thickness of the film can be deduced.

5.3   Discussion and choice of structure

Magnetic simulations were performed, but the design of the magnetic structures was decided before I had finished the simulations. Hence the simulations did not influence the design of the magnetic structures much. A point has been reached, however, where realistic simulations of the magnetic parts of the system can be performed. In the future this can be used for maximizing the effectiveness of the systems.

The structure chosen consists of 150 μm wide elements with a period of 500 μm (300 μm between them). They are placed 20 μm from the channel.

Chapter 6

Design of fabrication masks

To be able to fabricate devices, masks have to be designed. As presented in Chap. 1 I want to produce a system with microfluidic channels and magnetic elements at the sides. In Fig. 6.1 sketches of the system I want to produce are shown. One 3D sketch and one as a top view looking down into the channel. In the next chapter the fabrication sequence is explained in detail, but here it suffices to know that the structures are produced in a silicon wafer using two etch steps. It is necessary to use two etch steps because of the integrated microfluidic mixer, in which the ridges have to be etched to a different height than the bottom of the channel. The two masks designed are for producing etch masks for these two steps. The masks were designed in L-Edit v11, and the designs were send to Delta Mask [4] who fabricated the masks.
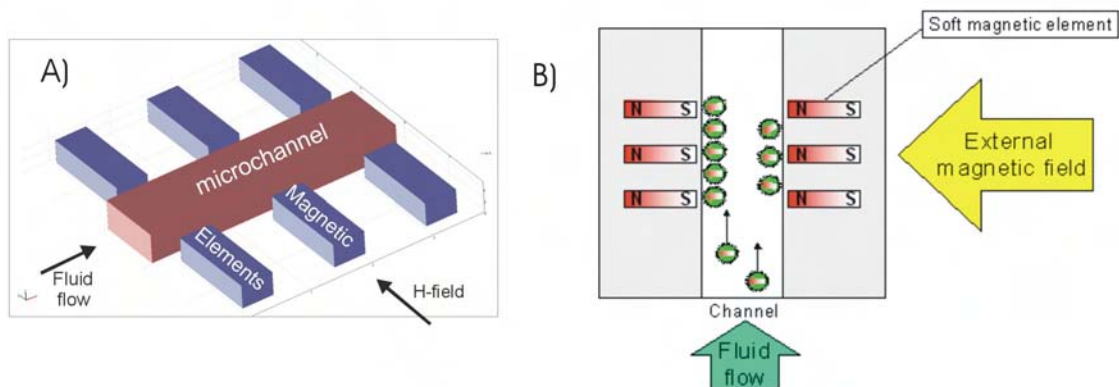

Figure 6.1: *A) A 3D schematic illustration of the basic passive magnetic separator we decided to fabricate in this project. B) A 2D schematic drawing of the passive magnetic separator with magnetic beads caught in the channel [1].*

In Fig. 6.2 the etch mask without the mixer part (mask1) is presented. Mask2 is almost identical to mask1 except for the ridges for the mixers and a few differences in the test structures and some identifying marks that are not present on both masks. Most of these small features cannot be seen when presenting the entire mask, and the important

differences can be seen in Fig. 6.3 and Fig. 6.4. The masks consist of 8 chips and a number of test structures. All the colored areas are the ones that are going to be etched. The 8 chips are all different and the parameters are listed in Table. 6.1.

Chip nr.	1	1M	2	2M	3	3M	4	4M
Channel width [μm]	100	100	200	200	400	400	200	200
Mixer	no	yes	no	yes	no	yes	no	yes
Number of inlets	1	1	1	1	1	1	2	2

Table 6.1: *Table giving parameters for the different chips on the wafer.*

Fig. 6.3 shows a close-up of the mask layout for both masks of a chip with a mixer. It is seen that the only difference between the two masks are the herringbones, an the two markers.

There are a number of different test structures on the mask, all of which can be seen in Fig. 6.4. For each channel width a similar magnetic structure is present for magnetic measurements. Squares are present for measurement of saturation magnetization. There is also a test structure which tests how close to the channel it is possible to place the elements and a structure which tests how narrow the ridges can be made. The last test structure is a number of long narrow magnetic elements, which should be used for magnetic susceptibility measurements.

The masks were designed after having worked with an older mask designed by Kristian Smistrup, which is seen in Fig. 6.5. This mask gave me a lot of problems with overplated structures and generally large differences in electroplating height and composition in different places on the wafer. In Fig. 6.5 arrows point to some of the places where overplating was a large problem. It seemed that overplating was worst at 90° corners and generally in places bordering to large areas where electroplating is not performed. In the new design all 90° corners have been changed to two 45° corners by cutting away a triangle, and the part of the chips not being electroplated is reduced and the chips with only one inlet have been narrowed (this was also to make room for eight chips). We also increased the electroplating area out to the edges, to make the electric field more uniform.

Figure 6.2: *Drawing of mask1 which is the mask for the step without microfluidic mixer structures. The green areas are the places where etching will be performed. During electroplating of magnetic elements electrical contact will be made near the rim of the wafer, and all etched areas in direct contact with these will be electroplated. If no direct contact is present between the etched areas no electroplating will happen. The barrier isolating the channels from the elements can be seen in the close-up in Fig. 6.3*
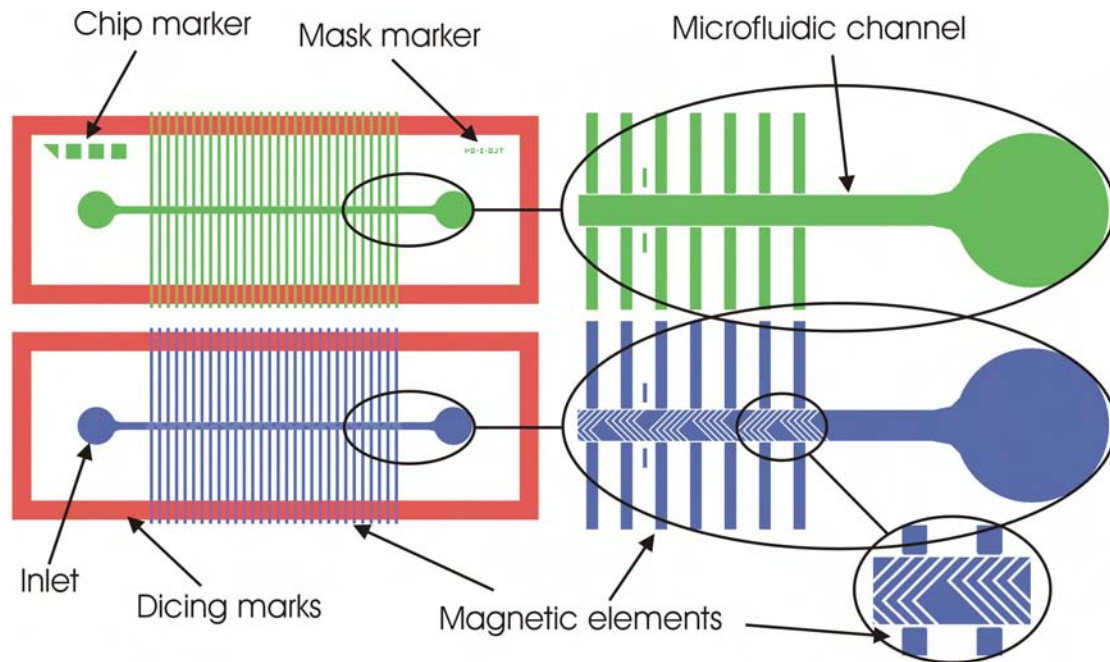
Figure 6.3: *Mask drawings of a chip with a 400 μm wide channel and an integrated microfluidic mixer. The green and the blue areas are the places where etching will be performed in the second and first etch step respectively (green: mask1, blue: mask2). The permalloy will be electroplated in the magnetic elements that are in electrical contact with the rim of the wafer, but not in the microfluidic channel that is insulated by a non etched area between elements and channel with a length of 20 μm. The elements are 150 μm wide and the distance between them is 300 μm. The diameter of the inlet and outlet holes is 2 mm. The red dicing marks are not present in the actual masks as can be seen in Fig. 6.2, but were used to define the outer limits of the chips. The chip marker can be used to identify which chip you are holding in your hand, and the mask marker is to see which set of masks was used, if masks with similar chips were to be designed.*
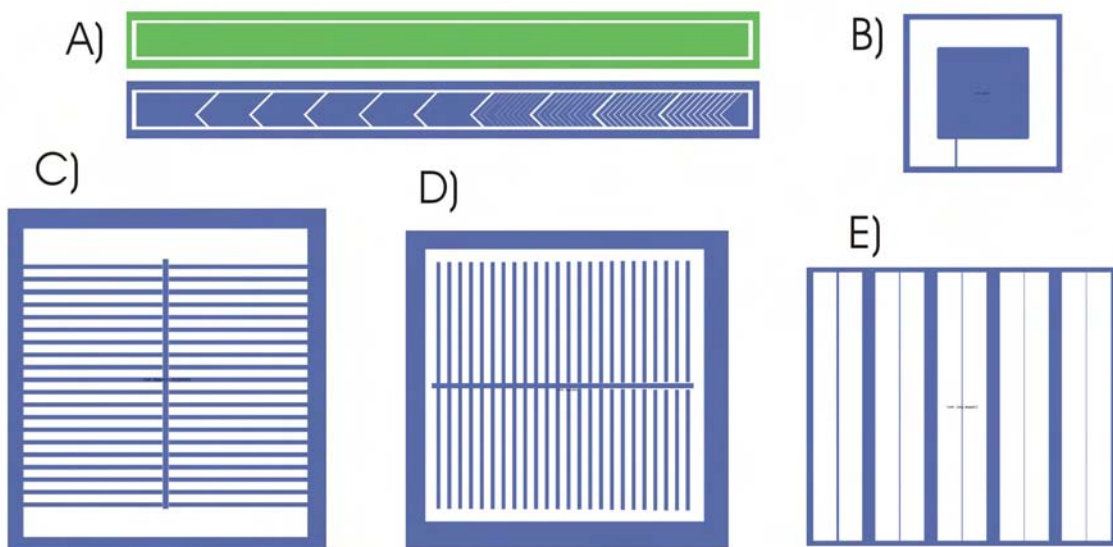
Figure 6.4: *A) Herringbone test structure. Used to test how narrow the ridges can be made. There are ten series of ridges with wr ranging from 1 to 50 µm, separated by a single ridge with wr = 100 µm. Only the widest ridges can be seen in the drawing at this magnification level. B) A square which can be used to determine the saturation magnetization. This can tell me the volume of the sample (and hence the thickness), and be related to the composition of the permalloy. C) A magnetic structure similar to the one for a system with a 200 µm wide channel. This can be used for measuring coercivity of the system, and the external field at which the magnetic elements saturate. The measurements on such a system can also be used to compare to simulations. D) A test structure for testing the minimal distance possible between elements and channels. The distances range from 3 to 60 µm and again only for the widest distances a separation can be seen at this magnification level. E) Long thin magnetic elements for measuring the intrinsic magnetic susceptibility of the electroplated permalloy.*
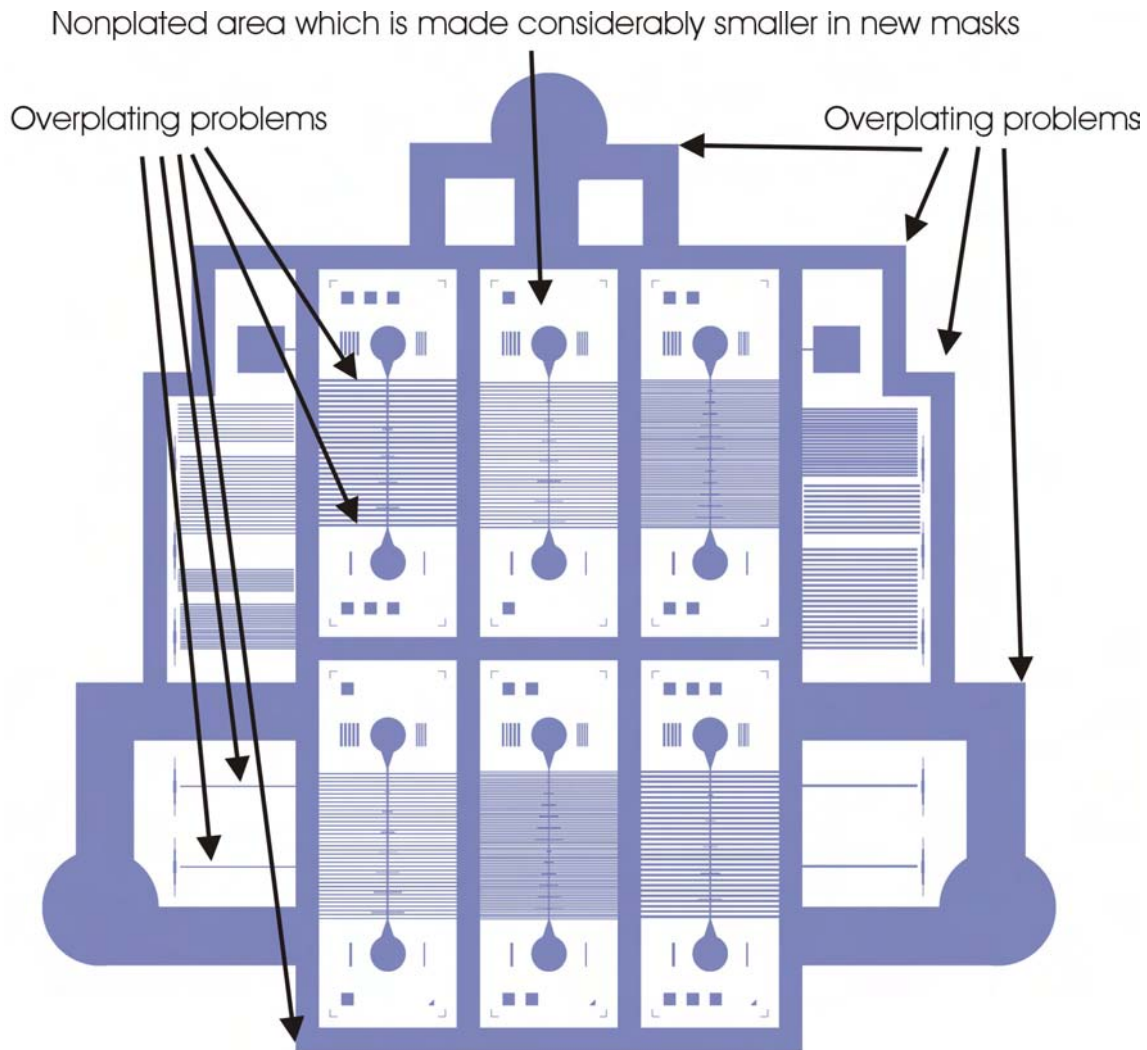
Figure 6.5: *Drawing of the mask used in the first tests of the fabrication sequence. If compared to Fig. 6.2 it is seen that all the outer corners where overplating was present have been removed on the new design. Also no test structures are present as the indicated one in the lower left corner, where two long elements in a large area of nonelectroplated silicon. The area around the inlet and outlet holes have been made a lot smaller to reduce overplating in the outer magnetic elements, and with the fluid connections used now they could become even smaller in new designs.*

Chapter 7

Fabrication of systems

In the following the process sequence will be shortly outlined. This is followed by a more detailed description of the process steps. In this description figures will be included to illustrate what happens to the wafer during the processes. For detailed information about the machines, recipes and times used, the reader is referred to appendix A. In the last part of the chapter critical process steps and their solutions are discussed. This is followed by a short summary of results.

7.1   Process sequence

7.2   Process steps

In this section figures are included. The figures have two drawings. The left drawing is a cross-section of part of the wafer, and the right drawing is a part of the wafer seen from the top. The drawings are not drawn to scale. In Fig. 7.1 the color of the different materials is illustrated, so that it is easy to see what is on the drawings.

Titanium   Silicon   Perm-alloy   Copper   Gold   Silicon Oxide   Photo resist   Pyrex

Figure 7.1: *Colors of the different materials in the drawings.*

7.2.1   SiO$_2$ mask for DRIE

In these process steps, an oxide mask for etching elements, and channels is fabricated.

The first step in this process is to grow a thermal oxide in a furnace. This is done twice in the process sequence, and I will explain both the procedures here.

When using the furnaces it is important that the wafers are clean. If new wafers are taken straight from the box, they are considered clean, but other wafers have to go through an RCA-clean before entering an oven. An RCA-clean consists in short of 10 min. in a mixture of H$_2$O, HNO$_3$, and H$_2$O$_2$ in the ratios 5:1:1 at 70°C. This step oxidizes organic

- Starting wafer: single polished
- Thermal growth of around 1.2 μm oxide in wet atmosphere at 1100°C
- Deposition, exposure, and development of 1.5 μm AZ5214 positive resist followed by hardbake
- Etching of oxide in BHF
- Resist strip
- Deposition and exposure of 6.2 μm AZ4562 positive resist
- Deep reactive ion etching followed by resist strip
- Deep reactive ion etching followed by oxide etch
- RCA clean and growth of around 0.1 μm oxide in wet atmosphere at 1050°C
- Deposition of 5 nm Ti and 200 nm Au
- Short Au etch in Entreat
- Electroplating of $2.5 - 3.0$ μm Cu
- Etching of Au in Entreat
- Electroplating of permalloy
- Dicing of wafer
- Cleaning of pyrex wafers with soap and water followed by piranha or 7-up clean
- Cleaning of silicon wafer with water and soap followed by oxide etch in BHF
- Anodic bonding of silicon wafer and pyrex wafer
- Dicing of chips

Table 7.1: Steps in the process sequence.

Figure 7.2: *The starting wafers are polished on one side.*

materials (eg. photo resist) into CO_2 and H_2O, and complexes IB and IIB metals (Ag, Au, Zn etc.) and other metals like Co and Cr [39]. This is followed by 10 min. in a mixture of H_2O, HCl, and H_2O_2 at 70°C 6:1:1. In this step hydroxides of alkali ions and other cations, formed in the basic solution of the first step, are complexed and removed from the wafer [39].

Growing a thermal oxide is typically done at temperatures between 1000 and 1200°C. It is possible to grow either a dry oxide (in an atmosphere containing O_2) or a wet oxide (in an atmosphere containing H_2O). The dry oxide takes longer to grow but the quality is higher. In the present case however it is not necessary to use anything but wet oxides. A higher temperature also results in faster oxidation [34].

In this process sequence growth of a thermal oxide is involved in two steps. The first oxide is used as a mask in a deep reactive ion etch (DRIE) and has a thickness of ≈ 1 μm. This means that a high temperature should be used to keep fabrication time low. This

step is performed with new wafers and hence no RCA cleaning is necessary. The second oxide is used to insulate the seed-layer from the wafer which is slightly conducting. For this a thin oxide is used, and therefore it is only necessary to use a low temperature. At this point in the process the wafers need to go through an RCA cleaning before the oxidation.

Figure 7.3: *1.2 μm of thermal oxide is grown. This is done in a wet atmosphere at $1100^\circ C$.*

The next step in the process is application of photo resist. To ensure good adhesion of the photo resist onto the wafer an HMDS-treatment is performed before the photo resist is applied. An HMDS-treatment is a process in which a thin layer of hexamethyldisilizane is formed on the wafer. The process is especially used when the top layer of the wafer is an oxide, since the oxide is hydrophilic and the photo resist is hydrophobic.

Then a 1.5 μm layer of AZ5214 positive photo resist is applied to the wafer, followed by exposure to ultraviolet light through mask1 and development. The photo resist mask is then hard baked.

Figure 7.4: *A 1.5 μm AZ5214 positive resist is applied. This is then exposed and developed (mask1) followed by a hardbake.*

The oxide etch is performed in buffered HF. After stripping the photo resist in an acetone bath the wafers are left with a mask of oxide.

Figure 7.5: *The oxide is etched in BHF and then the resist is stripped.*

7.2.2   Photo resist mask for DRIE

In these process steps a resist mask is fabricated for etching elements and channels with mixers.

First step is an HMDS treatment (see previous subsection) since most of the area, where the photo resist isn't removed, is covered by oxide.

Then a 6.2 μm AZ4562 positive photo resist is applied followed by exposure using mask2 and development.

The result after this step is a mask of oxide underneath a mask of photo resist. The oxide is covered by the photo resist everywhere, but the photo resist also covers areas not covered by the oxide (eg. the grooves)

Figure 7.6: *A 6.2 μm AZ4562 positive resist is applied. This is then exposed and developed (mask2).*

7.2.3   DRIE of structured channels and elements

In these steps the structures in the wafer are etched using the previously fabricated masks and Deep Reactive Ion Etching.
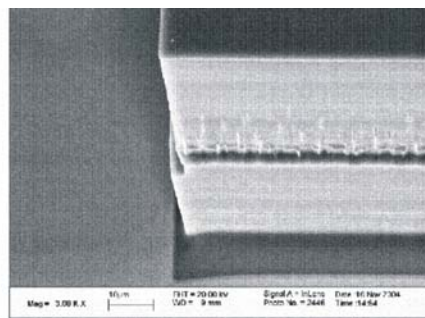

Figure 7.7: *SEM image of a corner that is etched with DRIE. The step seen comes from different sizes in the openings of the SiO_2 etch mask and the photoresist etch mask. It is seen that the sidewall is almost vertical. The height of the wall is 80 μm.*

Etching of the silicon to create channels, grooves, and conducting paths is performed by Deep Reactive Ion Etching. It is a process in which it is possible to make large aspact ratio vertical sidewalls. The etch is performed in cycles of etching and then passivation with a teflon-like layer, and it is a combined chemical and physical etch [26]. The chemical etchant does not etch through the passivating layer which instead is removed by physical

sputtering with ions. This means that the passivating layer is only removed on surfaces normal to the velocity of the ions which is at the bottom of the etched hole and not at the side walls. The holes in the passivating layer are thus approximately the same width as the hole in the mask and this creates vertical walls (see Fig. 7.7). An important thing to notice is that the etching rate is dependent on the area which is etched both locally and globally. This means that even though you use the same recipe it is necessary to tune the number of etch cycles needed to reach a specific etch depth, when a new mask is used.

The structures are created in two etching steps. In the first step the photo resist is used as a mask. The photo resist is then stripped by immersing the wafers into acetone. The second etching step is performed using the oxide as a mask. The etching time in this step plus the etching time in the first step determines the total channel depth, whereas the etching time in the first step determines the height of the ridges in the channels.

Figure 7.8: *Elements, channels, and grooves are etched and the resist is stripped.*

Figure 7.9: *Elements and channels are etched, and the oxide is stripped in BHF.*

7.2.4 Thermal oxide for electrical insulation

In these steps a thin thermal oxide of around 0.1 μm is grown, to act as electrical insulation between the electroplating base and the wafer. For further details of the process of growing an oxide see subsection "SiO$_2$ mask for DRIE".

Figure 7.10: *An RCA-clean is performed and then* 0.1 μm *thermal oxide is grown (wet at* 1000°*C).*

7.2.5 Deposition of electroplating base

In these steps electrically conducting layers are deposited to the wafer, and then removed from the surfaces where electrochemical deposition is unwanted.

First step in creating the electrically conducting structures is to deposit metals. This is done by e-beam deposition in static mode (the wafer is held in the same position at right angles to the direction of the metal). This should mean that no gold is deposited on the vertical sidewalls, and hence there should be no electrical contact between the top and the bottom of the structures on the wafer. The metals deposited are 5 nm of Ti and 200 nm of Au. The 5 nm of Ti is to ensure good adhesion of the gold onto the wafer. It has turned out that a little metal might be present on the vertical sidewalls and therefore a short Au etch is performed before the electroplating processes are started (the Au etchant used in this project is a cyanide based etchant called "Entreat").

Figure 7.11: *A seed layer of 5 nm Ti and 200 nm Au is deposited by e-beam evaporation.*

Electroplating is an electrochemical process in which it is possible to deposit thick layers of metal. In Fig. 7.12 a schematic of the basic setup for electroplating is shown, in this case it is for Cu, which is one of the metals I am plating onto the wafers. The same figure also contains a photograph of a wafer mounted in the waferholder with three contact points. In Fig. 7.17 a photograph shows the electroplating bath for permalloy.
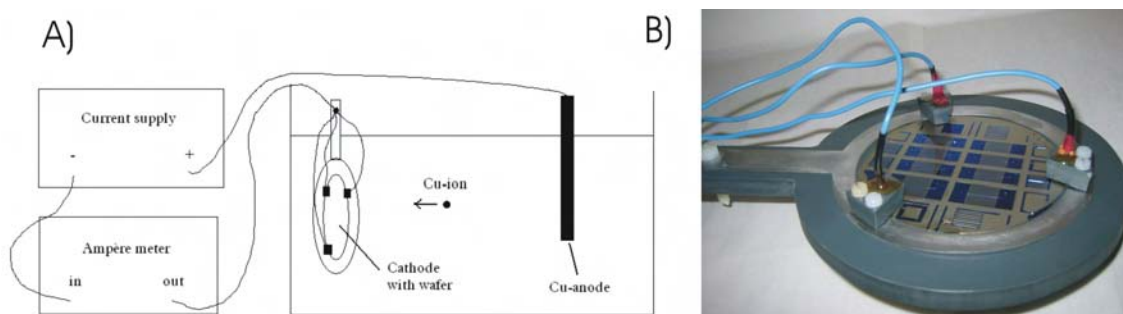

Figure 7.12: *A) A schematic for the setup used to electroplate Cu. B) A picture of a wafer mounted in the holder used for electroplating and with electrical contact to the seed layer in three places. Permalloy has been electroplated onto the wafer.*

When electrical potential is applied from the anode to the cathode a current of metal ions (in this case Cu^{2+}) will start flowing towards through the bath, and the following reaction will take place at the cathode:

$$Cu^{2+}(aq) + 2e^- \rightarrow Cu(s) \tag{7.1}$$

At the anode the reverse reaction takes place introducing new Cu^{2+} to the solution and electrons that will go through conductors to the cathode.

For any metal to be electroplated onto the wafers there has to be electrical contact from the places on the wafer where the metal is to be deposited, to the anode where the electrons for the reaction are produced. This is ensured by making electrical contact to a seed layer of metal on the wafer. This can be seen in Fig. 7.12. The trick is then to ensure that electrical contact only is present where deposition of metal is wanted.

I have found that when a thick layer of metal is to be electroplated, the seed layer should be removed everywhere except where metal is desired. This also has to be done even though there are steps in height so no electrical contact should be possible. The Au of the seed layer is removed with an Au etch, but then of course it is necessary to protect the areas where the seed layer should be kept. The protective layer for this etch is created by electroplating a thin layer of Cu onto the wafer.

Figure 7.13: *A short etch of Au is performed, followed by electroplating of* $2.5 - 4 \ \mu m \ Cu$.

This is followed by an Au etch in which all Au is removed from the top of the structures and from all places not directly connected to the conducting paths (e.g., the channels). The very thin layer of Ti has proven to be too thin to serve as a seed layer and is left on the wafer. Other work in the group has indicated issues with this, but I have not experienced any problems.

At this point it is possible to etch away the Cu, or to continue the process with the Cu still there.

Figure 7.14: *Au is etched away everywhere except where it is protected by Cu. If desired this can be followed by an etch of Cu.*

7.2.6   Electroplating of soft magnetic elements

In this step the magnetic structures are produced. This is done by electroplating permalloy onto the wafer. As mentioned in Chap. 5 permalloy is a soft magnetic material which consists of iron and nickel. The composition I try to reach is approximately 20% Fe and 80% Ni, which gives the lowest coercivity of the alloy (see Chap. 5).

The electroplating of permalloy is much more complicated than electroplating of eg. copper. This is because permalloy consists of two different metals [48]. When electroplating copper the wafer was kept as the cathode all the time. To reduce stress in the electroplated permalloy an alternating current with a period of 80 ms is used. See Fig. 7.16 for an example of how the driving signal could look. This means that the current supply in this case is controlled by a computer. A picture of a wafer after electroplating permalloy is shown in Fig. 7.17.

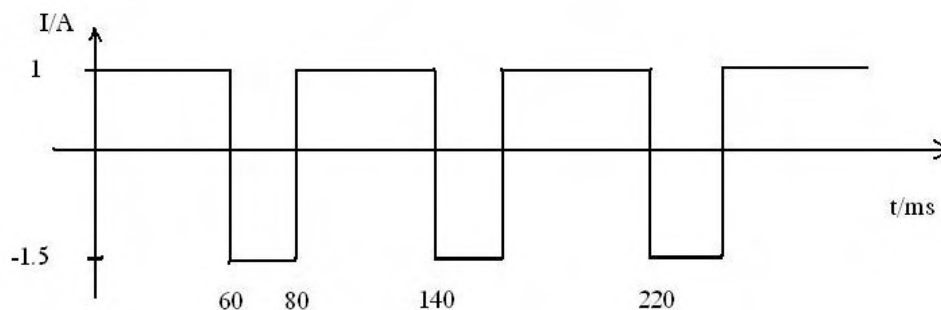Figure 7.15: *Permalloy is electroplated onto the electrically conducting structures.*

Figure 7.16: *Example of driving current for electroplating permalloy [48].*

7.2.7   Dicing of wafer to free chip area

In this step the wafer is diced to free the square center of the wafer containing the chips. No pictures are shown here, because nothing happens to the area containing the chips.

Optimally I would proceed straight to the next step without any dicing. This is because dicing is a dirty process, and the bonding process requires clean surfaces. It turned out, however, that stress in the permalloy made the wafer curve so much that anodic bonding was impossible. By removing the surrounding wafer the curvature is reduced and bonding is possible.
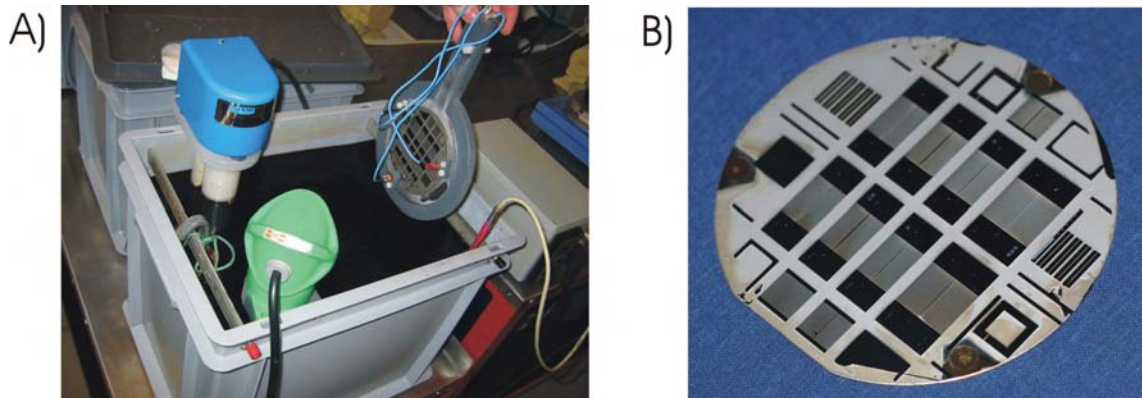
Figure 7.17: *A) A picture of the bath for electroplating permalloy. B) A picture of a wafer with electroplated permalloy.*

The dicing is done with a saw. The saw is a metal disc with diamonds in it and it is spinning at high speed.

7.2.8 Bonding of pyrex lid to wafer

In these steps the wafer and a new pyrex wafer are made ready for bonding and are subsequently bonded.

When the structures are finished it is necessary to bond a lid to the chips, to be able send fluid through the channels. This is done with anodic bonding. For anodic bonding clean surfaces are needed. This means that both the wafer and a new pyrex wafer have to be cleaned before bonding.

The first cleaning step is for both the processed wafer and the pyrex wafer. They are immersed into a sonic bath with water and Triton X100 soap to remove all dust and other particles.

On the processed wafer the oxide has to be etched, since the anodic bonding is performed between an Si surface and an SiO_2 surface. This also ensures a clean surface since the Si surface has been protected by the oxide since the RCA clean.

At the same time the pyrex wafer has to go through either a 7up cleaning or a Piranha cleaning, which should remove metals and other pollutants [39]. The piranha cleaning is better than the 7up, but the 7up is simpler. The piranha cleaning is performed in a fume hood, and a new solution is mixed each time. It consists of H_2SO_4 and H_2O in the ratio 4:1 and the temperature goes up to around 80°C. The 7up is located at a wet bench and consists of H_2SO_4 that is heated up to 80°C and then a spoon full of ammoniumpersulfate is added [5].

After cleaning the processed wafer and the pyrex wafer, the two wafers are pressed together (slight spontaneous bonding and Newton rings should be observed if the cleaning has been thorough enough), and they are now ready for anodic bonding.

Anodic bonding is performed by pressing the two wafers together between two plates. These plates are used as both heating plates and as electrical contact to the wafers.

Figure 7.18: *SiO₂ is etched from the wafer in BHF. This should also leave clean Si on the wafer.*

Figure 7.19: *A pyrex wafer is cleaned first with soap and water and subsequently by 7up or piranha clean.*

The chamber is vented and pumped out a few times, so that only N_2 is present. The temperature is then raised to 350°C, and an electric potential is applied between the plates. The mechanism of the bonding is not completely understood but an explanation given in Ref. [33] is as follows. The electric potential makes Na^+ ions, in the pyrex wafer, move away from the boundary between the wafers, while electrons in the silicon wafer also move away from the boundary. This creates a large electric field over the interface between the wafers, which results in an electrostatic force that pulls the wafers together. Because of the elevated temperature covalent bonds are then formed. The potential between the plates is slowly brought up to around 700-800 V and when the current is below 0.5 mA the process is finished. If parts on the wafer are higher than the silicon surface the wafers can not be pulled close enough together at those points. This means that they do not bond in a circle around that point, with a diameter depending on the height.
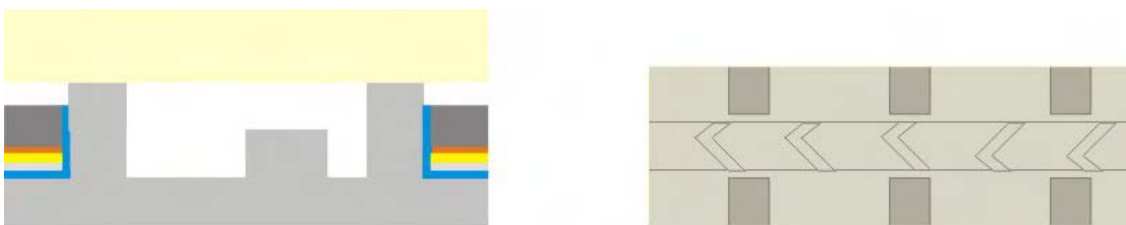

Figure 7.20: *The two wafers are pressed together and an anodic bonding is performed at 350° C.*

7.2.9 Dicing of wafer to release chips

The finishing step is to dice the wafer to release the chips and test structures. How the wafer is diced is explained earlier in the subsection "Dicing of wafer to free chip area" After this the only step left is to drill holes in the pyrex wafer for fluidic connections. See Fig. 7.21 for an example of how a finished chip might look.

Figure 7.21: *A finished microsystem for magnetic separation.*

7.3 Fabrication issues and critical steps

There are a few critical steps in the process sequence, that I will discuss below.

7.3.1 SiO$_2$ mask for DRIE

In this process a hard bake of the photoresist is carried out before the BHF etch. This is to enhance adhesion of the photoresist onto the wafer. When a photoresist mask is used in a long BHF etch it is often seen that a soft baked photo resist will detach itself from the wafer [5]. Since this BHF etch is fairly long a hard bake is applied to prevent this from happening.

7.3.2 Thermal oxide for electrical insulation

This step was not used in early attempts with the fabrication sequence. At that time the electrically conducting structures that are used as a seed layer were placed directly on top of the wafer. It turned out though, that the resistance of the wafers was not high enough to prevent electroplating of metal in other places (e.g., the channel). The solution to this

was to use an oxide to insulate the deposited metal from the silicon wafer. This is done by growing a thermal oxide of around 0.1 μm.

7.3.3   Deposition of electroplating base

This part of the process sequence has gone through many iterations. At one point I was using 30 nm Cr instead of 5 nm Ti between the wafer and Au. This was because Ti has to be etched in HF which was not present at IPL where the electroplating took place. It turned out though that the Cr etch (consisting of H_2O, HNO_3 and $CeSO_4 \cdot 4H_2O$) is quite unreliable unless you produce a new one every time. I then tried with a very thin layer of Ti and wanted to see if it was possible to leave the Ti layer on the wafer during the electroplating. It turned out that even though overplating was present, which means that the permalloy made contact to the top surface, plating of permalloy would not spread across the entire top surface. This means that the Ti layer is so thin that it cannot function as a seed layer.

Initially when electroplating Cu, Au was still present on the top surfaces. This meant that when an electrical contact was made from the bottom to the top surface, electroplating of Cu would spread to the entire top surface, and it often did. I tried to prevent this by performing an Au etch before electroplating Cu, to remove any traces of Au that might be present on the sidewalls. However, since the Au etch isn't uniform a short etch is desirable. In the first attempts 500 nm Au was deposited. Cycles of Au etching were performed while measuring the resistance from bottom to top of the structures. The necessary Au etch times almost removed the Au in places. The thickness of Au was then changed to 200 nm and it turned out that with a very short etch of Au (50 s) large resistances from bottom to top of the structures were achieved. The result was a uniform Au layer and fewer problems with this process step.

7.3.4   Electroplating of soft magnetic elements

This step has caused many problems. The main problem has been that the electroplated material seems to climb up the walls (see Fig. 7.22) causing the metal in some places to grow above the structures while still far below the top of the structures in other places. This seems to increase with increasing current density. On the other hand the ratio between Fe and Ni is also affected by the current density. The ratio of Fe becomes larger with increasing current density. This means that it does not work just to lower the current density, without changing the composition of the electroplating bath.

Also the large variations in current density are present on the wafer. Close to areas where no material is electroplated the current density is higher than in places where material is electroplated all around. This results in composition variations across the wafer. I have measured on wafers where the the amount of iron varied from 15 to 30 percent. The variations aren't as large around the chips, but can still vary up to around 5 to 10 percent. This will be further discussed in Sec. 8.1.
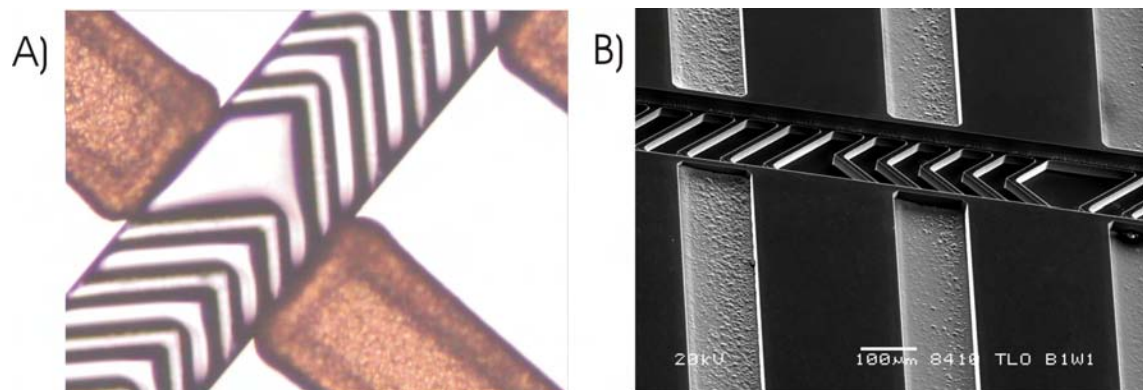
Figure 7.22: *A) A micrograph of a 200 µm wide channel with overplated elements. B) A SEM picture of a similar structure. Here the elements aren't overplated, but it is easy to see that the permalloy sort of climbs up in some of the corners and sides.*

7.4 Discussion

A process sequence was developed, that enabled me to successfully produce functional systems, however electroplating of permalloy is a problematic process in which not all effects are understood.

This process can be optimized by performing a series of experiments where the current density is varied. Preferably it should also be done with two different iron contents in the bath. The composition and magnetic properties of the electroplated permalloy as well as the height variance should be determined across the wafer. This would provide a better background for choosing electroplating parameters.

This should be combined with simulations of the electric field. It is very likely that the difference in electroplating height and composition, could depend mainly on the electric field (though we also have indications that stirring could have an affect). It should be possible to perform calculations of the electric field, and this could be compared to the results. If this can explain the variations, then simulations could be used in the future when designing masks.

Chapter 8

Characterization of systems

There are many different elements to a characterization of the fabricated systems. One way to characterize them is by measurement of dimensions and composition and magnetic properties of the electroplated structures. In the first part of the chapter the characteristics of the electroplated structures are presented.

Another way characterize the systems is by their ability to capture magnetic beads. To do this a set-up was designed. The design of the electromagnet and a chipholder is presented together with a general description of the set-up enabling me to control and repeat the experimental conditions like, e.g., sample volume.

For a thorough characterization of the systems I wanted to do quantitative measurements. To do this a way to measure small amounts of magnetic beads had to be devised. The method is presented together with the measurements performed to validate the method.

This is followed by a section about the experiments performed that is split into a few parts. The first part is about the capture of beads and a qualitative characterization of the systems based on these observations. The next part is about the release of beads and the collecting of samples for quantitative measurements, and the results and observations deduced from these experiments.

In the last part of this chapter initial biological experiments performed on the systems are presented. This is followed by a summary of the chapter, and a discussion of the results.

8.1 Composition of magnetic elements

As explained in Chap. 7 the composition of the electroplated structures varied significantly across the wafer. The systems used for experiments in this project come from two different wafers. The approximate composition of the magnetic elements on those chips can be found in Table. 8.1. The measurements of the composition were performed using the Scanning Electron Microscope on IPL. It has an added module for Energy Dispersive X-ray analysis system (EDX). With that spectra can be measured, that can be related to the composition of the material analyzed. The time available to me with this equipment was limited. This

means that the number of measurements were limited and some values are approximated.

Wafer4			
Place on wafer	Near channel and inlet or outlet	Near channel in the middle of chip	away from channel
Fe content in %	29 ± 1	25 ± 1	21 ± 1
Wafer5			
Place on wafer	Near channel and inlet or outlet	Near channel in the middle of chip	away from channel
Fe content in %	17 ± 1	-	12 ± 1

Table 8.1: *The composition of the magnetic elements on the chips. Measurements were only performed on one of the chips for each wafer, The numbers are based on three to four measurements.*

8.2   Magnetic measurements

A few magnetic hysteresis measurements were performed on some of the fabricated test structures. Fig. 8.1 shows a hysteresis curve from a test structure of magnetic fingers comparable to a system. From this curve it is seen that the magnetic structures are saturated at an external magnetic field of $\mu_0 H \sim 20$ mT, and $\mu_0 H_c \sim 0.5$ mT. The composition is not the same as for the systems used, but systems of similar composition to the systems used were not available. This is because the test structures created for this purpose were located near the rim of the wafer with different surroundings. The result was a different composition of the electroplated structures on the chips and the test structures.
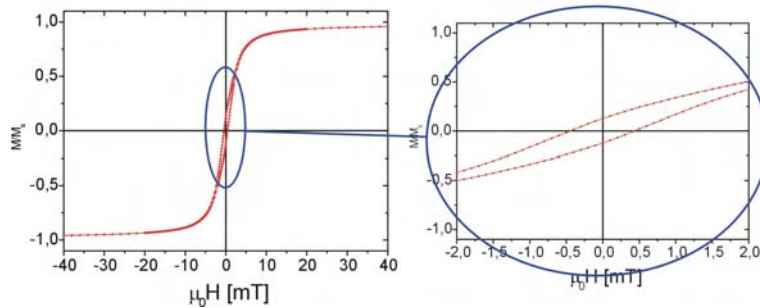
Figure 8.1: *Hysteresis curve from magnetic measurement on magnetic system from chip with 200 μm wide channel. The chip came from wafer3 and the composition was around $17 - 21\%$.*

The thin magnetic test structures were fabricated to measure the intrinsic susceptibility of the permalloy. Measurements, however, did not produce reproducible data and were

therefore discarded. We do not known what happened, but I assume it is due to some effects occurring during the electroplating of the very narrow structures (10 μm).

8.3 Chipholder

The chipholder serves two purposes. It has to fix the system so that it is possible to handle, and it has to provide fluidic interconnection between the external tubes and the fluidic channel/channels of the system. In appendix B a workshop drawing of the chipholder with two inlets is presented. In Fig. 8.2 a photograph is seen of the same chipholder with system mounted. The design was made to avoid dead volumes to the extent possible since magnetic beads tend to get caught. Also the access holes in the chipholder are made as smooth as possible. In Fig. 8.3 two micrographs are shown of caught magnetic beads in a design where channel smoothness and diameter was a problem. The fittings used to attach the external tubes to the chipholder are Lee fittings type 062 MINSTAC [6].
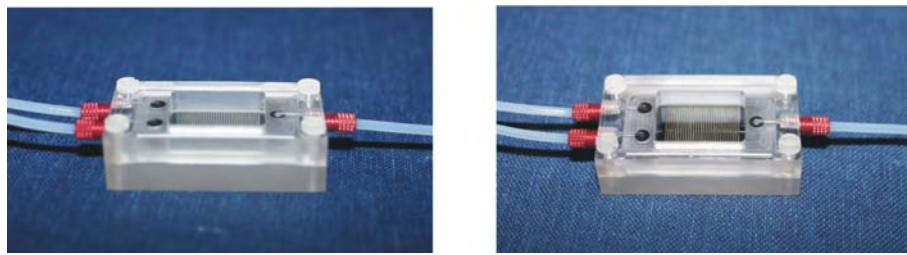
Figure 8.2: *Photographs of a chipholder with two inlets and a system mounted.*
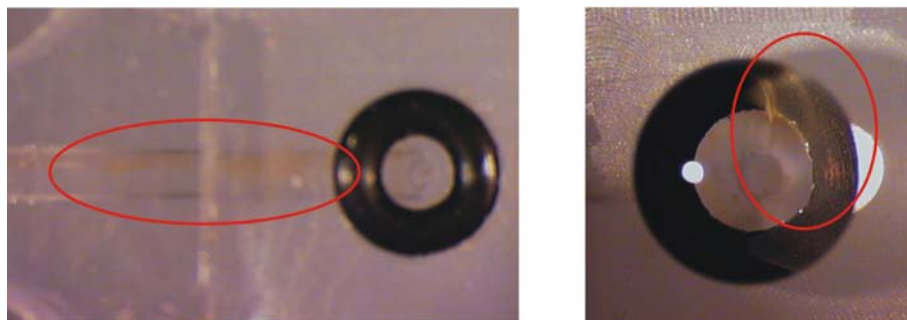
Figure 8.3: *Micrographs from an experiment where beads got caught in the chipholder. The brown haze with circles around it is the magnetic beads. In the left micrograph they are seen in the channel, and in the right micrograph they are being pumped out of the channel using a higher flow rate than in the experiment.*

8.4   Electromagnet

The electromagnet serves the purpose of producing a homogeneous external magnetic field. A picture of the fabricated electromagnet can be seen in Fig. 8.4. In Fig. 8.5 sketches and explanation of the working principle of the electromagnet can found.
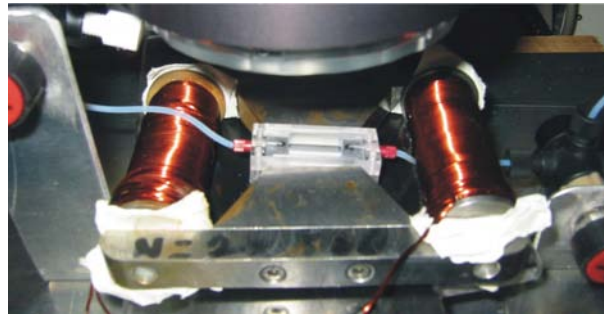

Figure 8.4: *Photograph of the electromagnet placed under the microscope. In the middle of the electromagnet a chipholder with mounted system is seen. During experiments this was fixed horizontally in the electromagnet.*
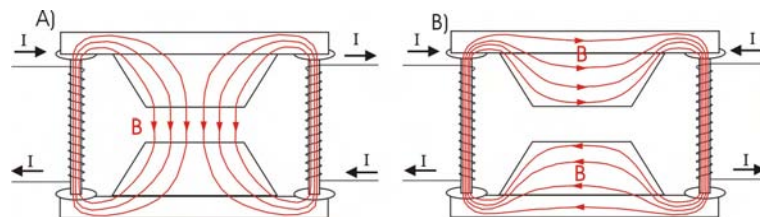

Figure 8.5: *Sketches of the electromagnet. A) The currents through both coils creates magnetic flux in the upwards direction forcing the magnetic field lines to move across the air gap, and thus creating a homogenous magnetic field in the air gap. B) the currents in the two coils create magnetic flux in the opposite direction, and thus they magnetize the pole shoes perpendicular to the direction across the air gap. This removes the magnetic field from the air gap.*

8.5   Set-up

The set-up has to ensure that controllable, and reproducible amounts of sample can be introduced to the system. In Fig. 8.6 a sketch, and a photograph of the part of the set-up used for isolating a controllable amount of sample can be found. This did enable me to control the amount of bead solution introduced to the system, but I had problems with beads getting stuck in the set-up. The parabolic flow profile in the tubes means that close to the surface of the tubes the velocity of the fluid is very slow. This means that the water used to push the sample will push the sample in the middle of the tube in front

of it, while "overtaking" the sample close to surface. Therefore a lot of water has to be pushed through, before all of the sample is introduced to the system. The differences in the dimensions of the tubing and valves of the set-up and the system channels makes the fluid velocity in the set-up so slow, that sedimentation of the magnetic beads becomes a problem. The diameters of tubes and valves in the set-up are up to 1 mm.
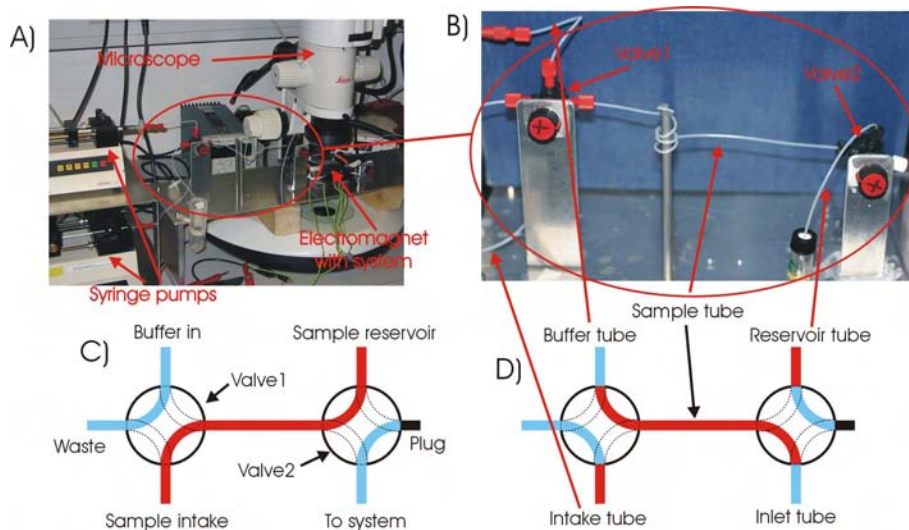

Figure 8.6: *A) Picture of most of the set-up, including microscope, and syringe pumps. B) An enlargement where only the sample control system can be seen. C) and D) Schematics of the sample control system. C) is after intake of sample. In D) the valves have been turned and the set-up is ready for pumping the sample into the system. There are two ways to control the sample volume. The main parameter is the length and/or inner diameter of the sample tube. This way large sample variations are controlled. The other parameter is the way the valves are turned after sample intake, and this has an effect of ~ 5 or 10µL. In D) they have been turned counterclockwise, which means that the inner volume of the valves is also pushed into the system. In my experiments I have had problems with beads getting stuck in the tubing. In the experiments presented here the inner diameter of sample tube, inlet tube and buffer tube were 800 µm and the diameter of the reservoir tube was 250 µm. The inner diameter of the valves is 1 mm, which is why I have chosen to let the sample go down through the valves.*

In Fig. 8.7 a schematic of the entire setup can be seen including microscope, electro-magnet, chip, and collecting point.

8.6 Choice of magnetic beads

In Table. 8.2 data for the beads used in this project is found. The beads chosen were MyOne beads from Dynal Biotech. Other beads (e.g. M280 from Dynal Biotech) were tested but the larger beads, though easier caught in the systems, were also easier caught
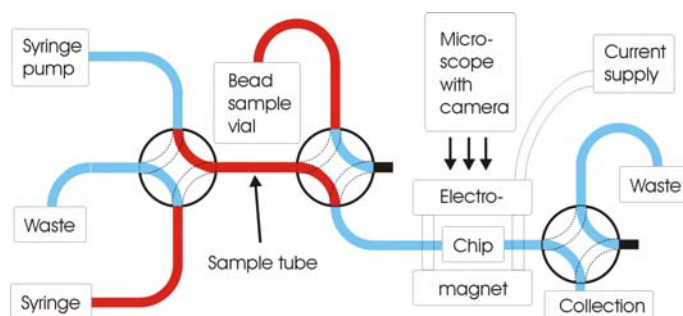
Figure 8.7: *Schematic of the entire set-up.*

in the setup.

Bead	Diameter [μm]	Density [g/cm^3]	Iron [mg/g]	χ	M_s [kA/m]
MyOne	1.05	1.7	255	1.38	40

Table 8.2: *Data for MyOne beads from Dynal [21]*

8.7   VSM determination of bead amount

If a quantitative characterization of the systems should be performed a way to reliably and accurately measure the amount of beads before and after the experiments had to be found. This proved quite a challenge.

Two methods were considered. One was to count the number of beads in known volumes under a microscope, and the other method was to measure the magnetic moment of the samples in the vibrating sample magnetometer (VSM) (see Fig. 8.8). The method chosen ended up being the VSM method. The sample was collected in 250 μL PCR tubes and placed on top of permanent magnets to collect the magnetic beads at the bottom of the tube. The supernatant was then removed and after the sample had dried, superglue was added to fix the beads at the bottom of the tube. The tube was mounted in the VSM using the sample holder seen in Fig. 8.9.

The problem with this method turned out to be the considerable background signal. The nonlinear part of the background signal was changing once in a while. This problem was solved by measuring the background signal often. Examples of the measured background signal can be seen in Fig. 8.10. Here it is seen that the measurements can be very similar, but as mentioned they could suddenly change. The next challenge was to test whether it was possible to measure the amounts of beads I was working with. Initial calculations had shown that it should be possible, since the measuring limit of the VSM should be 1 nAm^2 and the amounts I was working with had a magnetic moment of 20 - 60 nAm^2. All quantitative experiments were performed with the same solution. Examples of reference curves measured for different amounts of sample can be seen in Fig. 8.11.

These reference curves were used to conclude that the method gave reliable results. Reference measurements were also performed on clean deionized water and deionized water run through a system after cleaning, to test whether the handling of the samples influenced the measurements, and to test whether the systems were cleaned sufficiently. Curves for these measurements can be seen in Fig. 8.12. From all of these measurements it was concluded that the VSM method can be used for measuring the magnetic moment of samples with an uncertainty of approximately 2 nAm^2 based on 20 measurements. It is important though to be careful in the handling of samples, since a single dust particle can have a magnetic moment of 4-5 nAm^2. It is also important to measure the background signal often since it can change (e.g., because of dust).

8.8 Experimental conditions

All experiments presented were performed using a 500 times diluted solution of streptavidin coated MyOne beads from Dynal [2]. The original solution was bought with a mass concentration of 1% beads. The physical data for the beads can be found in Table. 8.2.

A number of experiments were performed on different systems using flow rates between 5 μL/min and 40 μL/min. In the experiments presented here the width of the channels were 400 μm, the external magnetic field was 55 mT, the release flow rate was 40 μL/min, and the systems were from wafer4, unless otherwise specified. The sample volume was
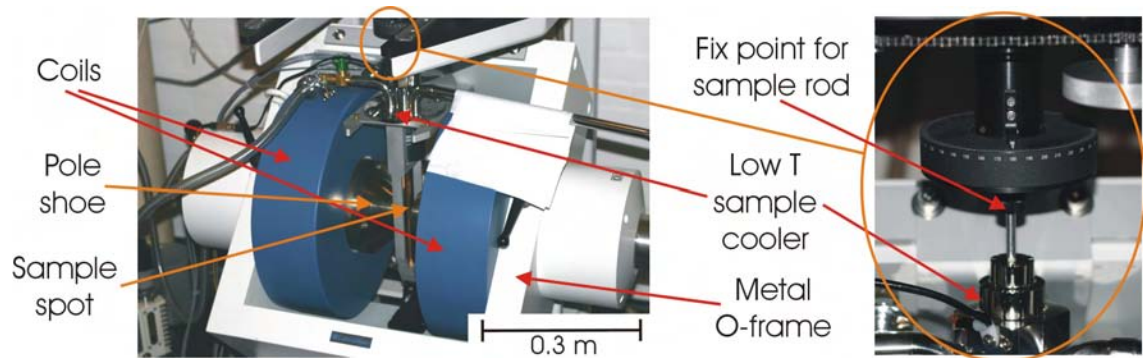

Figure 8.8: *To the left is a photograph of the electromagnet in the VSM. The VSM electromagnet is very like to the one I fabricated (see Sec. 8.4), except that the coils are placed on the pole shoes in stead of on the metal O-frame. In this picture a low T sample cooler is mounted. The measurements in this project were performed at room temperature with the sample rod hanging freely. To the right a closeup of the point where the sample rod is fixed. The fix point vibrates, thus making the sample vibrate in the magnetic field between the pole shoes. This means that the sample is magnetized and is vibrating, thus inducing a voltage in small coils placed on the pole shoes. The voltage is measured by the VSM and is used for calculating the magnetic moment of the sample. A large power supply can supply currents in the range $\pm100A$ making the VSM able to create magnetic fields of up to 2.3 T.*
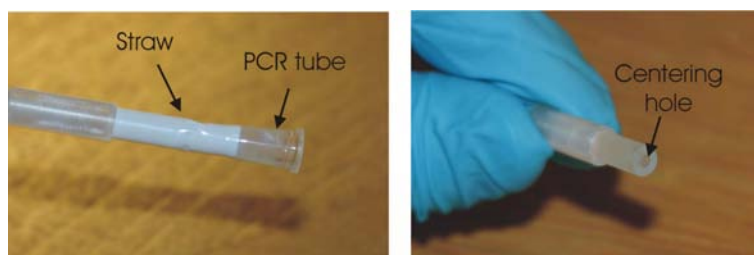
Figure 8.9: *To the left a photograph of the sample holder with a piece of straw and a PCR tube attached. To the right the sample holder without straw and PCR tube. The centering hole is what ensures that the PCR tube is placed with the bottom (where the sample is) in the same position each time.*
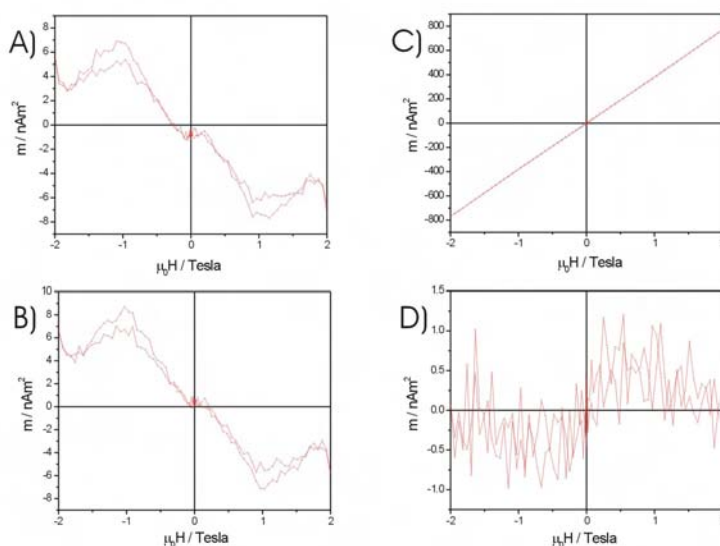

Figure 8.10: *In C) a measured hysteresis curve for the sample holder with straw can be seen. A) and B) are two measurements following each other, where the linear slope has been subtracted. The linear slope was calculated from the measurements between -2 to -1.5 T and between 1.5 to 2 T. In D) the two measurements are subtracted from each other. It is seen that the difference is within the detection limit of the VSM.*

≈ 110 μL, and to make sure the conditions were the same each time, a thorough cleaning of the set-up and system using a 2% NaOH-solution followed by deionized water was performed between each experiment. The release flow rate was used for 5 min before releasing the beads. This is because a shift to a higher flow rate might release beads that have escaped the system, but are stuck in the set-up. I only wanted to collect beads that had been caught in the system, not the ones that had escaped. The disadvantage of this is that caught beads could be torn free and escape the system. An experiment was performed as follows:
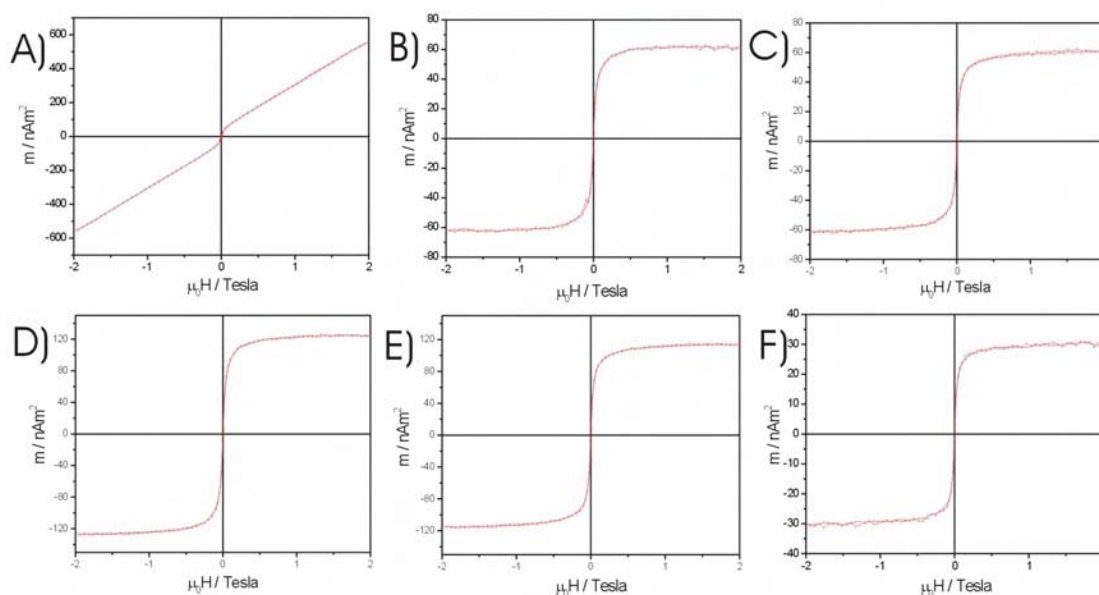
Figure 8.11: *A) is the raw measurement of a sample using* 100 *μL of sample solution. B) and C) are two similar measurements where the background signal and the linear slope has been subtracted. D) and E) are measurements using* 200 *μL of sample. It is seen that they are slightly different but that the average* M_s *is the double of the curves from the measurements using* 100 *μL of sample. D) and E) are included, even though I have curves matching each other, to show the amount of fluxuation sometimes encountered. This is probably due to sample handling, and not because of the measurements. F) is a curve from a measurement using* 50 *μL of sample solution.*

- Bead solution was sucked into the setup
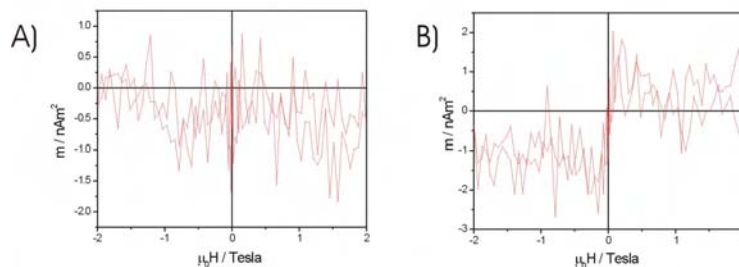
Figure 8.12: *A) is the curve from a measurement using* 250 *μL of deionized water, and B) is the curve from* 250 *μL deionized water run through the cleaned set-up and system. It is seen that both curves are very close to zero signal.*

- Switch valves were turned thus isolating a controlled sample volume

- Electromagnet and syringe pumps were turned on

- Bead capture was continued until 500 μL buffer was pushed through

- Flow rate was raised to flush flow rate (40 μL/min)

- After 4-5 min the electromagnet was turned off, thus releasing the beads

- Samples were collected in plastic PCR tubes

The visible aspects of the experiments were straightforward. As long as no air bubbles entered the systems and the washing of the systems after the NaOH-solution was sufficient these experiments were easily reproducible. When releasing and collecting the beads for quantitative measurements, however, a lot of problems were encountered. It turned out a lot of care had to be taken for the experiments to be reproducible. I will take the problems one at a time. Explain what the problem was, why it was experienced, and how it was solved.

In some experiments the beads would stick to each other more than usually. This turned out to be due to insufficient washing after the use of the NaOH solution.

In experiments on systems with mixers it was seen that almost all beads were collected in the first PCR tube. This was assumed to be the same for experiments on systems without microfluidic mixer. The amount of beads collected from these experiments, however, was a lot smaller and varied a lot. For a time this led me to believe that there was something wrong with the measurements. The reason, however, turned out to be that for experiments on systems without mixers, the beads would sometimes, but not always, reach the collecting point in the set-up later than the time used to fill the PCR tube. I will get back to the reason for this in Sec. 8.10. This caused large fluxuations in the results and I ended up collecting 3 PCR tubes for these experiments and 2 PCR tubes for systems with mixer.

Tests were performed to see what magnetic moment was measured on samples where no capturing of the beads was performed. Samples were collected where the inlet tube is normally connected (see Fig. 8.6) and on samples run through the system without applying the magnetic field. In the last case the measured magnetic moment corresponded to a little under 100 μL of sample, and for the for the first case it corresponded to a little over 100 μL of sample. These experiments however, were performed with flow rates higher than 40 μL/min. I have indications that some beads always stick in the set-up, and that the amount depends on the flow rate. Therefore magnetic measurements to investigate this further have to be performed. This should be done by running samples through at flow rates comparable to the experiments. The time limit, however, did not permit this, since I focused on being able to perform reproducible efficiency measurements for the systems. The efficiency numbers given in this chapter are in percent compared to 100 μL of sample (a magnetic moment of 60 nAm^2).

8.9 Bead Capture

Experiments showed that beads could be caught and released in the systems for flow rates ranging from at least $5 - 60 \ \mu$L/min. For a comparison of the systems with and without integrated microfluidic mixer, however, a more thorough characterization of the capturing efficiency was necessary. For different experiments to be comparable, micrographs were taken during experiments.

In Fig. 8.13 micrographs for two experiments with $Q = 40 \ \mu$L/min on a system with integrated micromixer is seen. In Fig. 8.14 micrographs from a similar experiment, on a similar system, but without integrated microfluidic mixer is seen. From the micrographs in Fig. 8.13 it is easy to see that the experiments were reproducible. When compared to the micrographs in Fig. 8.14 it is seen that the beads are caught more efficiently in the system with the integrated microfluidic mixer, than in the system without integrated microfluidic mixer.

This is even more obvious in experiments with $Q = 20 \ \mu$L/min. In the system with the mixer all beads seem to have been caught in less than 2/3 of the channel (see Fig. 8.15. For the system without the mixer, beads can be seen caught on all elements (that is the entire length of the channel) (see Fig. 8.16). Furthermore when looking into the microscope during the experiment, beads could be seen leaving the channel without being caught. This could not be seen in the experiment with mixer.

For experiments with $Q = 10 \ \mu$L/min, it is a little more difficult to see. For the system with the integrated microfluidic mixer all beads seem to be captured in the first third of the channel (see Fig. 8.17). For the system without mixer, most beads also seem to be captured in the first third of the channel, but traces of beads are seen almost all the way down the channel, and some beads were also seen exiting the channel during the experiment. When comparing these micrographs to micrographs from experiments with higher flow rates it looks as if fewer beads have entered the system.

In Table. 8.3 different observables from the experiments performed are presented.

With mixer			Without mixer		
Q μL/min	Beads visibly caught till element	Beads not caught	Q μL/min	Beads visibly caught till element	Beads not caught
10	8-12	no	10	24-28	few
20	18-20	no	20	30	yes
40	27-28	few	40	30	yes

Table 8.3: *Table listing visible characteristics from experiments on systems with* 400 μm *wide channels. Systems are from wafer4.*

Some experiments were also performed on systems with a 200 μm wide channel and two inlets. These systems came from wafer5. The visible characteristics can be found in Table. 8.4.
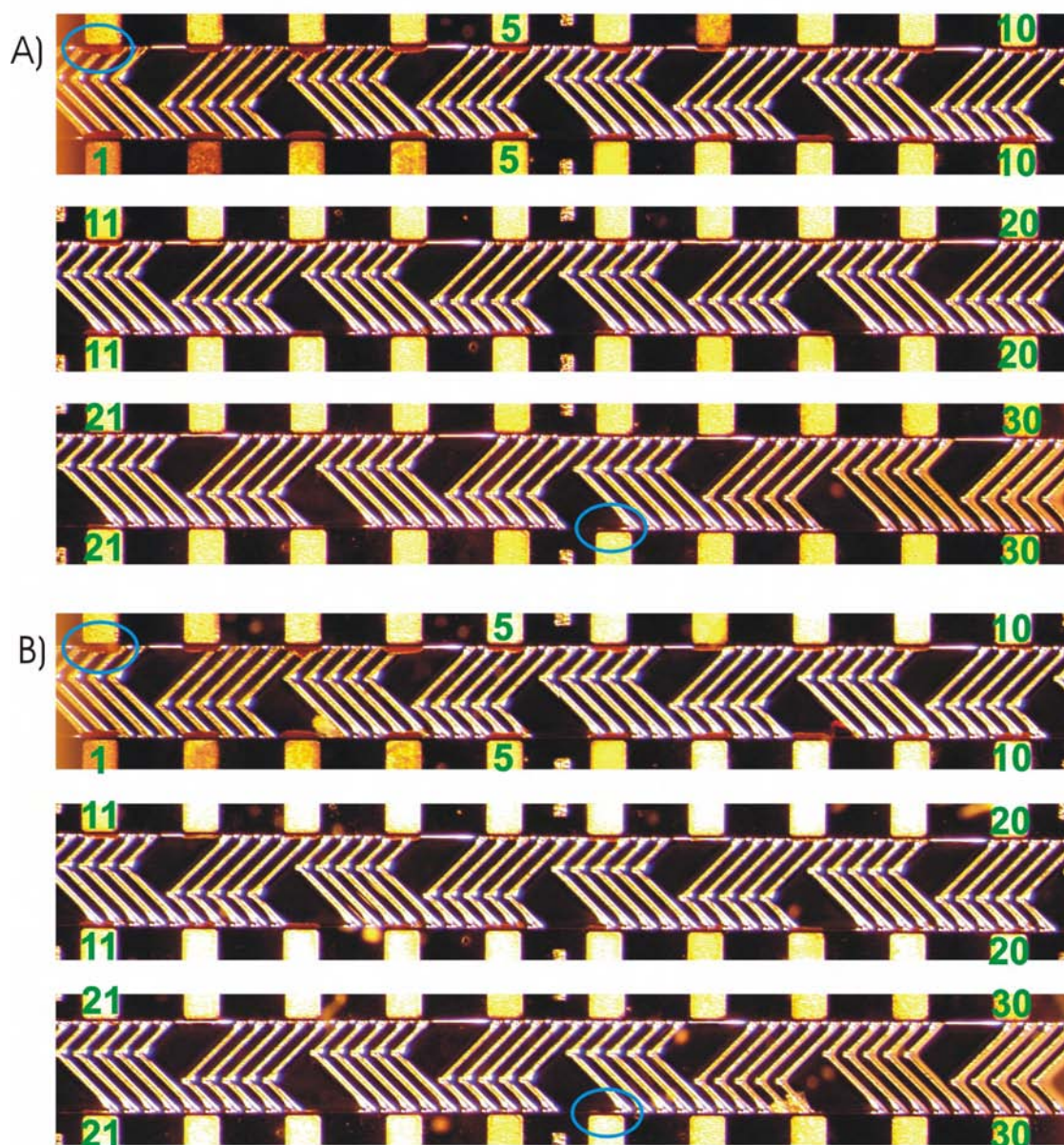
Figure 8.13: *Micrographs from two similar experiments with $Q = 40\mu L/min$. For each experiment 3 lines of micrographs displays the entire channel after bead capture. The blue circles are around places where beads are caught. I have placed two circles for each experiment: One at the first element where many beads are caught, and one at element 26 where only a few beads are caught. The last element where beads are visible is element 28 for both experiments, but it is difficult to see in the picture.*

8.10   Bead release and quantitative measurements

Bead release and sample collection did not have an influence on the qualitative characterization of the capturing efficiency. However they had a huge effect on the quantitative
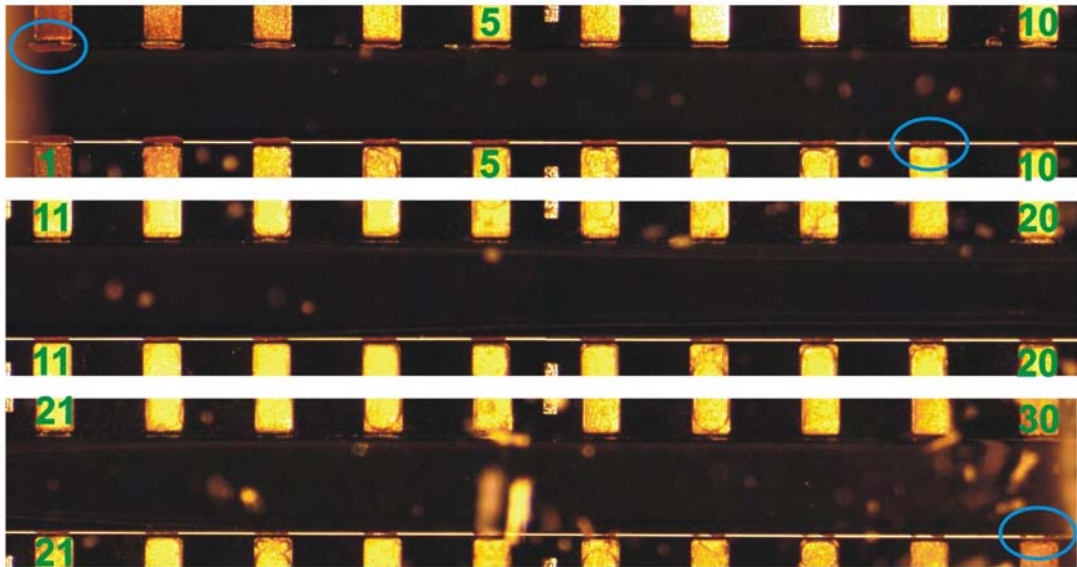
Figure 8.14: *Micrographs for an experiment similar to the experiments shown in Fig. 8.13. Again blue circles are placed around a few of the places where beads are caught. In this experiment it is easy to see that beads are caught on all elements, and when looking in the microscope during the experiment it was also easy to see that many beads left the channel without being caught. When compared to the micrographs from Fig. 8.13 it is seen that the amount of beads on the first element is comparable, but while the amount of beads caught on each element decreases rapidly in this experiment it only decreases slowly in the experiment on Fig. 8.13.*
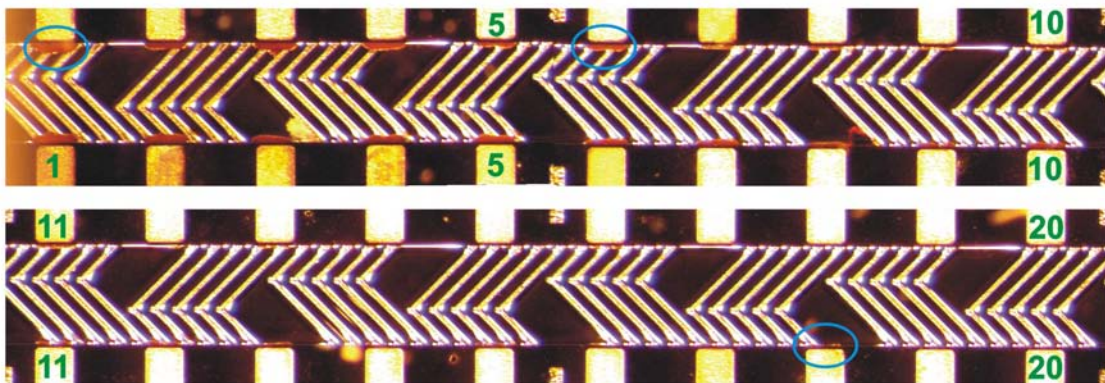
Figure 8.15: *Micrographs from an experiment with $Q = 20$ $\mu L/min$. In this experiment beads can be seen caught till element 18 (the last place with a blue ring), which is between 1/2 and 2/3 of the channel.*
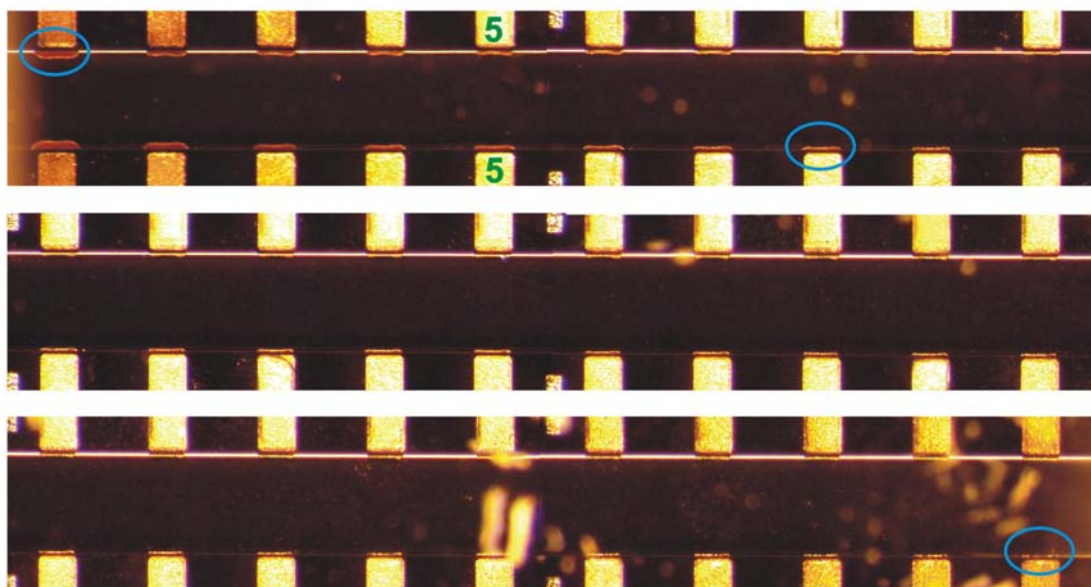
Figure 8.16: *Micrographs from an experiment with $Q = 20$ $\mu L/min$. In this experiment beads can be seen caught on all elements, and during the experiment beads were seen escaping the channel.*

With mixer			Without mixer		
Q $\mu L/min$	Beads visibly caught till element	Beads not caught	Q $\mu L/min$	Beads visibly caught till element	Beads not caught
10	-	-	10	25-27	few
20	14-15	no	20	30	yes
30	30	few	30	30	yes

Table 8.4: *Table listing visible characteristics from experiments on systems with 200 μm wide channel. Systems are from wafer5.*

characterization. I will start by mentioning what was seen when releasing the beads. In doing this the reason why more PCR tubes had to be collected for experiments on systems without mixer than with mixer is explained.

When releasing the beads in the systems with the microfluidic mixer, it is seen that the mixer makes certain that the beads get evenly distributed in the cross section of the channel, whereas when releasing the beads in the systems without the mixer the beads stay close to the sides of the channel where the fluid flow is slow (see Fig. 8.18). This means that it takes longer for the bulk of the beads to reach the collecting point, and also that the sample collection is stretched out in time and hence the sample is diluted more. For experiments with mixers almost all beads were collected in the first PCR tube, while it would vary a lot for experiments without mixers. This is an unexpected but welcome effect of integrating the magnetic separator with a microfluidic mixer.
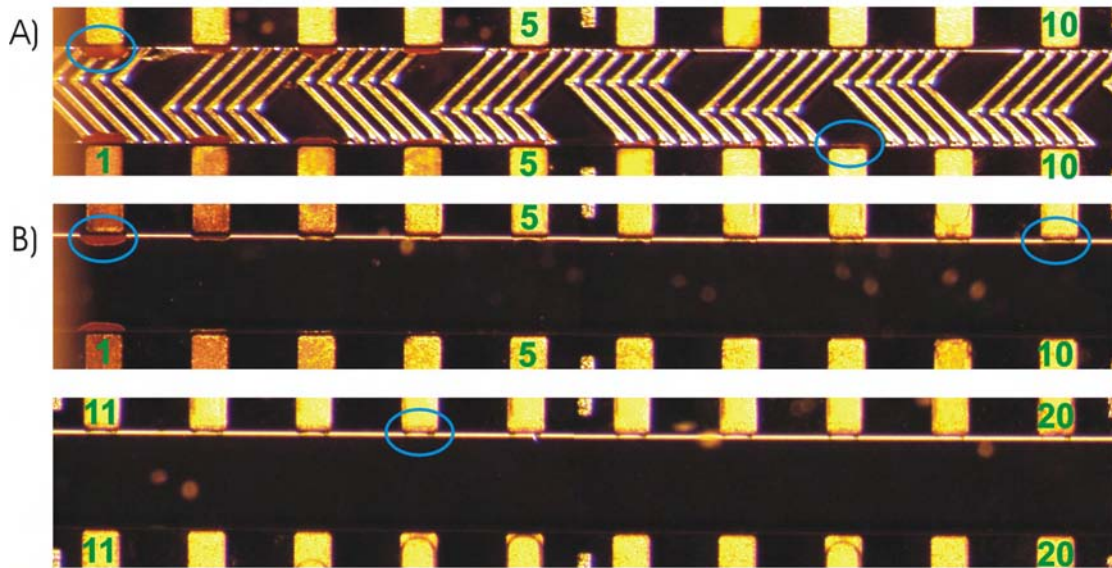
Figure 8.17: *Micrographs from experiments with $Q = 10$ $\mu L/min$. A) In this experiment beads can be seen caught till element 8 (the last place with a blue ring), which is between 1/4 and 1/3 of the channel. B) In this experiment traces of beads can be seen caught till element 26 (out of 30) but only the first 2/3 of the channel are shown, since it is only shadows like the last elements visible here, that can be seen. During the experiment beads were seen escaping the channel, but I believe it is only a very small amount compared to the entire sample.*
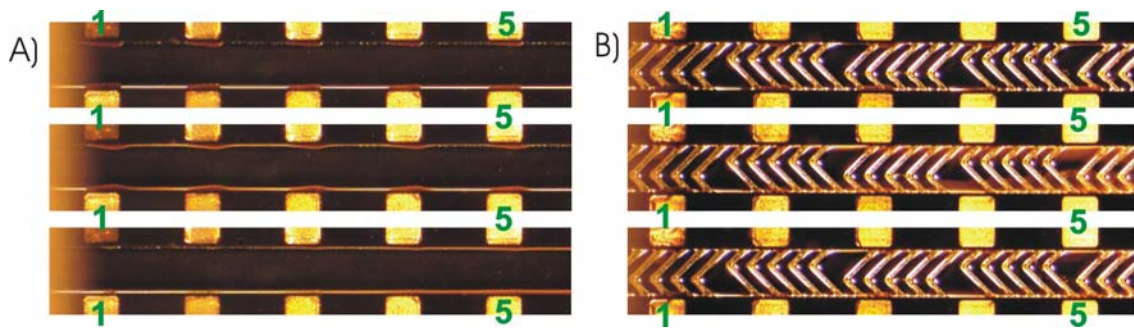
Figure 8.18: *Micrographs of the release of beads. Both systems come from wafer5 and have 200 μm wide channels. The parameters used in the experiments were $Q = 40$ $\mu L/min$, $Q_{release} = 50$ $\mu L/min$, and the external field was 40 mT. A) Micrographs after 0 s, 0.2 s, and 0.6 s. It is seen that the beads stay close to the side of the channel. B) Micrographs after 0 s, 0.2 s, and 0.4 s. In the right side on the micrograph after 0.2 s the brown haze shows that the beads move away from the sidewall and into the channel.*

Another thing noticed when releasing the beads is that it is not always all beads

that are released. Traces still stick to the top, side and bottom of the channel where beads had been caught. In Fig. 8.19 micrographs after release of the beads from one of the experiments in Fig. 8.13 can be seen. In this experiment it is seen that quite a few beads were not released, but this varied from experiment to experiment. Generally though it seemed that a few more beads were stuck in systems with an integrated mixer. Experiments were performed for systems both with and without integrated mixer though, where all beads were released. In Fig. 8.20 micrographs from before and after bead release are presented from an experiment where all beads seemed to be released. Also it seemed that I had more problems with the systems from wafer4. This was also the wafer with the highest iron content. Together this shows that this is an effect we should be able to minimize, with the right composition of magnetic elements and handling of the systems (like the buffer used to push the beads and to clean the system).
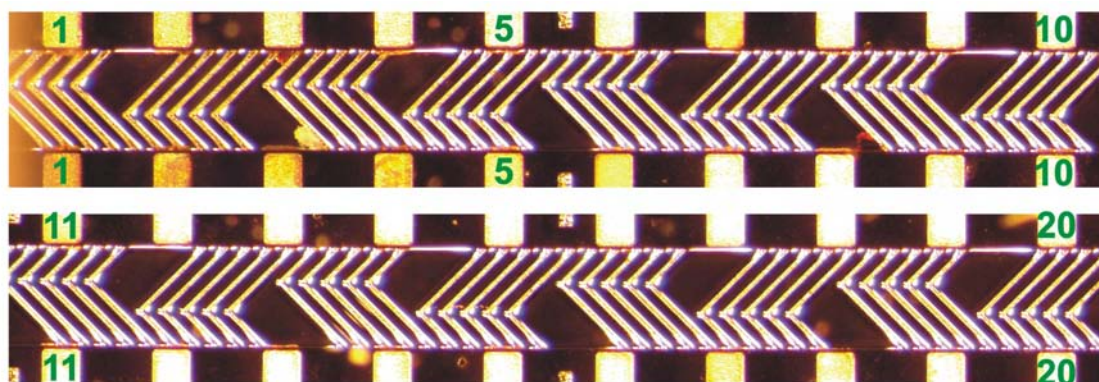
Figure 8.19: Micrographs of the channel after bead release from one of the experiments shown in Fig. 8.13. It looks like quite a few beads are sticking.

Quantitative measurements were performed of experiments on systems with 200 μm wide channels from wafer5. At the time of these experiments I had doubts about whether or not the method was working and therefore high flow rates were chosen. It turned out however that the flow rates were so high that the beads, at least for the system with integrated mixer, had difficulties sticking to the elements. In Fig. 8.21 micrographs of the bead capture can be seen. The experiments however gave me reproducible results. The efficiency obtained in two consecutive measurements for a system with mixer was 39 and 44% and for a system without mixer it was 33 and 38%. The curves measured are shown in Fig. 8.22. These measurements cannot reliably tell us that the systems with mixer are more efficient, but as mentioned this is probably due to the high flow rate. They indicated, however, that the measurement method worked.

For the 400 μm wide systems the same experiments used for the qualitative characterization in Sec. 8.9 were used for quantitative measurements. However, the only flow rate for which I have reliable quantitative experiments is 40 μL/min. I have made a table where also 10 and 20 μL/min are present, but these come from single experiments or early experiments in which not everything worked perfectly (see Table. 8.5).

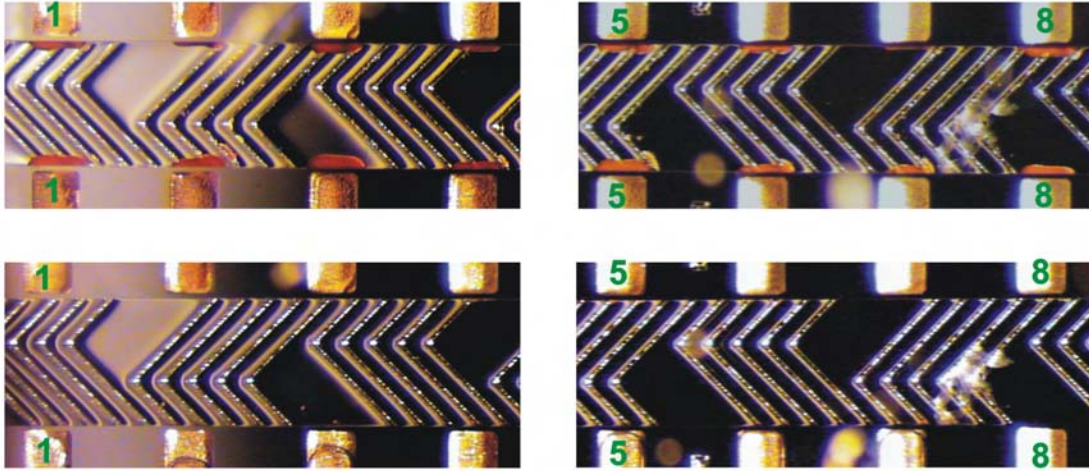Figure 8.20: *Micrographs from an experiment with a 400 μm wide system system with integrated mixer from wafer5. Q = 40 μL/min. Here no beads can be seen after release.*
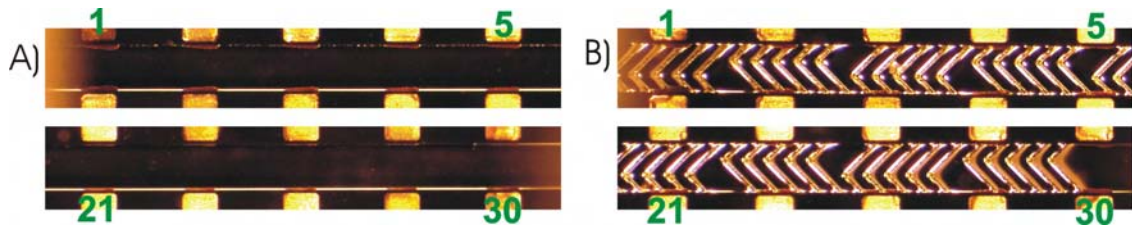

Figure 8.21: *Micrographs after capturing of beads. Both systems come from wafer5 and have 200 μm wide channels. The parameters used in the experiments were Q = 40 μL/min, $Q_{release}$ = 50 μL/min, and the external field was 40 mT. A) and B) Micrographs of the first five and last five elements of the system for both experiments. In B) it is seen that no beads stick above the ridges, since the ridges are visible with beads on each side. It is also seen that the amount of beads is almost the same everywhere. For the system without the mixer it is obvious that the amount of beads on the last five elements is much less than on the first five. This indicates that the system with the mixer was limited by what could stick to the elements, but the system without mixer was not.*

The measurement uncertainty was determined to be $\approx$ 2 nAm^2 which corresponds to $\approx \pm 3\%$ for my measurements. These measurements were after optimization of the experimental conditions, and as was the case for the 200 μm wide systems no far off measurements were encountered. I therefore find the measurements reliable. Within the measuring uncertainty of the VSM method they show the systems with integrated mixer to be more efficient.

While optimizing the experiments to make the quantitative measurements reliable many measurements were made. Although fluxuations in the measurements have made them less reliable a significant difference in capture efficiency was seen. The measured
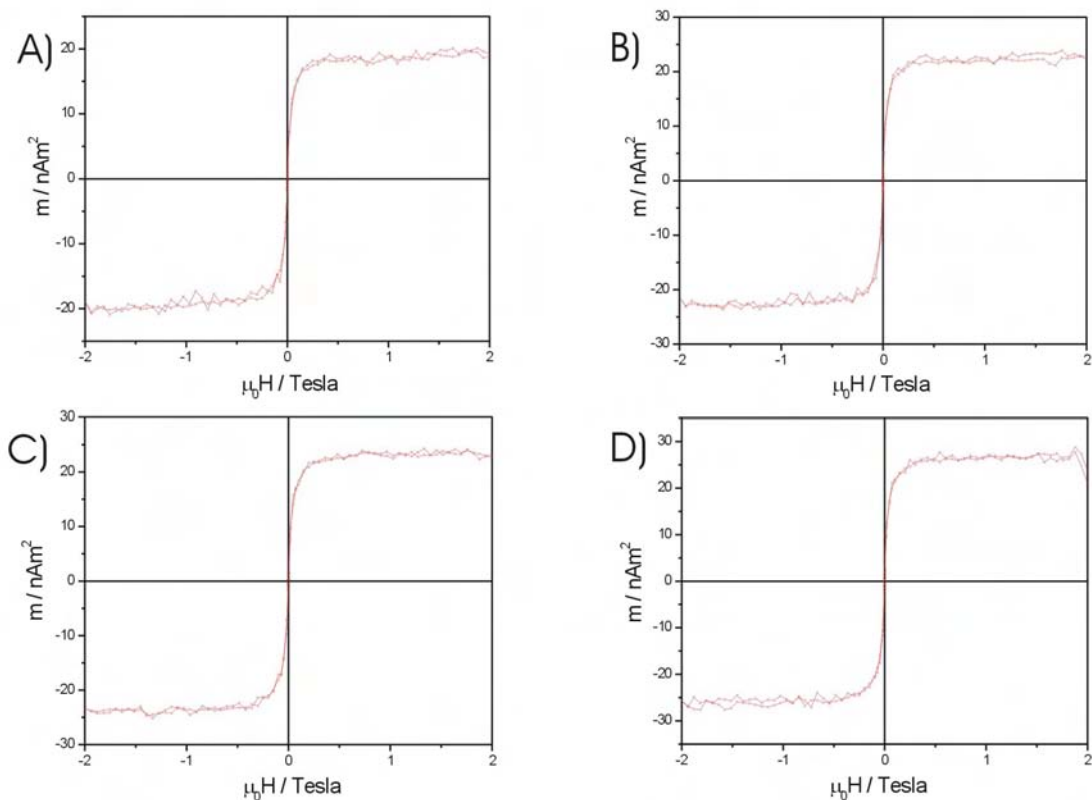
Figure 8.22: *The measurements used for quantitative results of the experiments shown in Fig. 8.21.*

With mixer			Without mixer		
Q	Beads visibly	Quantitative	Q	Beads visibly	Quantitative
μL/min	caught till element	measure	μL/min	caught till element	measure
10	8-12	(45, 50%)	10	24-28	(55%)
20	18-20	(57, 62%)	20	30	-
40	27-28	68, 70, 73%	40	30	52, 54%

Table 8.5: *Table listing characteristics from experiments performed on systems with* 400 μm *wide channels. Every number represents one measurement. Bead capture is relative to* 100 μL *of bead solution (see). The lower capturing efficiency for lower flow rate could be explained by more beads getting caught in the set-up at lower flow rates. That this effect is not seen for systems without mixer could be because at the higher flow rates many beads escape the channel, and this weighs up with the fewer beads entering the system*

efficiency for the systems with mixer was generally between 50 and 80%. No measurement on systems without mixer gave an efficiency above 55%, and in most measurements the

efficiency was around 20 to 30%. Some of it may come from beads being delayed or getting caught because they stay near the side wall when released, but this also is a quality that makes the systems with mixer better. They are more reliable.

8.11 Summary and discussion

In this chapter the main results for the project were presented, and here I will sum up the results.

Magnetic measurements

Only a few measurements of magnetic properties were performed. For this there are several reasons. When these measurements were performed I had already designed my systems and finished the magnetic simulations. These measurements therefore were not as important as other aspects of the project. The measurements performed, however, showed that the magnetic elements are most likely saturated in the experiments.

Future work would be to perform measurements of the magnetic susceptibility for a range of compositions to have curves to use as input in magnetic simulations. These measurements would also provide information on the coercivity of the electroplated elements, and I would like to minimize this parameter.

Set-up

A set-up for the experiments was fabricated. The chipholder was designed and optimized, and an electromagnet that works well was also designed. A sample introduction system consisting of tubes and valves was designed and fabricated, and this enabled me to introduce controllable amounts of sample to the system. However, the main problem with the set-up seems to be the tubing and switch valves. The dimensions of these are quite large (up to a mm in diameter), and this causes beads to get stuck in the set-up due to low fluid velocities.

A characterization of this problem for different flow rates is necessary, and also a better set-up would be desirable.

VSM bead measurements

A way to do reproducible measurements on small amounts of magnetic beads was developed. This included the use of a VSM and PCR tubes. This method proved to work.

Characterization of systems

Qualitative experiments were performed for flow rates between 10 μL/min and 40 μL/min for both 400 μm and 200 μm wide channels. All of these experiments showed the systems with the mixer to be more efficient magnetic separators than the equivalent systems without mixers. These experiments also indicate that the capture efficiency is close to 100% up to 40 μL/min for the systems with mixer and up to 10 μL/min for systems without

mixer. This, however, could not be confirmed by the quantitative measurements. This is probably due to beads getting stuck in the set-up, and could have been resolved had I had more time.

If the qualitative indications are true the systems fabricated are effective compared to what is presented in the literature. Most articles only present a proof of concept with no details on flow rates and capture efficiencies and hence no direct comparison can be made to these systems. In articles where further information is given the presented data shows the systems to be less effective than the indications for my systems. In the ref. [17] they present a system of similar channel dimensions to my systems where more than 95% of the magnetic beads entering the system are caught (they do not, however, characterize the amount of beads stuck in the set-up and system). This is performed at a flow rate of 2 μL/min. In this article problems with beads sticking to the magnetic elements was encountered. In another article a flow sorter is presented, where a flow rate of 1 μL/min is used [41]. In Ref. [18] and Ref. [43] much larger systems than mine are used with flow rates of $3 - 7$ and $1 - 2$ μL/min respectively, without giving proof that all beads are captured.

Quantitative measurements for experiments on the systems were also performed. To the best of my knowledge this is not done by anyone before us. Most of the experiments were used as iterations toward a working solution, but in the end I was able to perform reproducible experiments. These showed that the system with mixer is most effective. They also showed, however, that the amount of beads escaping the channel in the systems without mixer is small.

As mentioned the qualitative characterization indicated that all beads are captured, but the efficiencies measured in the quantitative experiments are not as high as the qualitative experiments predict. The experiments indicate, however, that much of this effect comes from beads sticking in the set-up. This of course has to be investigated, and also further efficiency measurements should be performed to be able to do statistics on the results.

It also seemed that the mixer is a plus not only when capturing the beads but also when releasing the beads. The mixer helps get the beads away from the sides of the channel, and thus they are flushed out of the system faster and also the spreading of the sample is smaller.

When releasing the beads, however, more beads tended to stick for systems with mixer than systems without mixer.

Chapter 9

Conclusion

In this project passive microsystems for magnetic separation have been fabricated and characterized.

Simulations of the fluid flow in diagonal mixers and staggered herringbone mixers have been performed. To validate the simulations a comparison of simulations to an analytical solution and an experiment was performed. The simulation and the analytical solution agreed well, and qualitative agreement was found between the simulation and the experiment.

In the simulations many parameters have been varied, and on the basis of these simulations some design rules were developed for maximizing the effectiveness of the mixers. These can be found in Sec. 4.8.

The theory of magnetostatics has been studied, and this has been used to understand the systems, and the parameters affecting the magnetic properties of the magnetic elements.

A process sequence for the fabrication of my systems has been designed and improved to the point where systems can be fabricated in a short period of time. It should be possible to fabricate functioning magnetic separators in less than a week.

A chipholder, electromagnet and sample introduction system were designed for the set-up. These were used for experiments. The set-up produced reproducible results, though problems were encountered in the form of beads sticking in the set-up.

Qualitative characterization at several flow rates for both 200 μm and 400 μm wide systems were performed. These experiments showed the systems with the microfluidic mixer to be the most effective separator. They also showed, however, that more beads tended to stick in the channel after bead release for systems with mixers than for systems without mixer. Compared to the current literature, the systems have been characterized very thoroughly. Compared to the systems in the current literature where some kind of characterization is present, both types of systems were shown to be very effective magnetic separators.

A method for doing quantitative measurements on very small amounts of beads was developed. This method gave reproducible measurements of reference samples. The measured background signal, however, would change once in a while. Probably due to dust

particles with a magnetic moment. This problem was solved by measuring the background signal often.

The method was used for doing quantitative measurements of the experiments performed. Initial problems were encountered, but in the end reproducible measurements were performed. These measurements, like the qualitative characterization, showed the system with the mixer to be the most effective magnetic separator. They also indicated that not all beads entered the systems, but that some were caught in the set-up. To the best of my knowledge this type of measurements has not been performed before.

Experiments were performed which showed that the mixer helps release the beads in a faster and more controlled fashion. They can be collected during a shorter time interval than for systems without mixer, and hence are not diluted as much.

Chapter 10

Outlook

In this thesis many possible improvements have been mentioned, and in this chapter I will write about some of the most important ones. I will finish by prioritizing the work if a few months were left of the project, but more importantly what the long term goals are.

10.1   Microfluidic simulations

I would like to do simulations for optimizing the asymmetry and staggering period with respect to mixing efficiency. Also experiments to validate the parameter optimizations presented in this thesis should be performed.

10.2   Fabrication of systems

The basic fabrication sequence works, but problems with the electroplating of permalloy should be investigated. This includes electroplating in baths with different iron content for different current densities. The results should be tested with respect to composition across a wafer, the plating height across a wafer, and measurements of the magnetic properties like coercivity and susceptibility.

Simulations of the electric field could help us design structures in which the problems with overplating are minimized.

Fabrication where the overplating problems are on the backside of the wafer could improve fabrication success rate and capturing efficiency. Another aspect of the fabrication would be to transfer the process to, e.g., SU8 technology, to make the fabrication faster and cheaper.

The systems could be integrated with other functionalities like a PCR chamber or waveguides for spectrophotometry, or a long mixing channel for incubation of biological samples with magnetic beads directly in the system. The incubation in system would mean that beads and sample are introduced through two different inlets. Running through the mixing channel the incubation is performed, and then the beads are caught in a magnetic separator. In this way incubation and separation is performed in one step.

10.3   Set-up and experimental conditions

It is obvious that the set-up causes problems. There are many things that can be done about this, however. First of all the research into and commercial possibilities of microfluidic interconnections and devices has to be investigated. What are the possibilities?

With the current set-up, however, some things can also be done. One very simple thing is to work with a higher concentration of beads, and smaller sample volumes. This would reduce the length of tubing, and hence could reduce the amount of beads sticking in the tubes. Another possibility is to use water with detergents like Triton X100 in stead of clean deionized water. This is done in [17] and could reduce sticking between beads, and between beads and surfaces. I do not know, however, if this is compatible with biological experiments.

10.3.1   Experiments

The qualitative characterization of the systems generally worked very well. There was one problem, however. In some of the experiments not all beads were released during bead release. This problem might be minimized by using other buffers in stead of deionized water, as mentioned above. Another solution could be to increase distance between magnetic elements and channel. This should reduce the sticking problems, but also reduce capturing efficiency of the systems.

The quantitative characterization of the systems was not as easy as the qualitative. I succeeded in performing reproducible experiments, but due to lack of time the systems were not thoroughly characterized. It is therefore desirable to perform more experiments. It also has to be investigated how many beads stick in the set-up at different flow rates, to be able to give the true separation efficiencies.

10.4   Future work prioritized

If a few months were still left of the project the main goal would be to finish the quantitative characterization of the systems. This means that many experiments should be performed for different systems, and it should be investigated how many beads enter the system for different flow rates. An extension would be to look at the effect of different buffers possible to use in biological experiments.

The most important result from this project, however, is that effective microscale magnetic separation systems were fabricated, and that the fabrication sequence is simple. This means that the most important future challenge is to find applications for the magnetic separator. As mentioned initial biological experiments were performed with the systems. The plan is in cooperation with a group doing stem cell research at Oslo university, to design a microchip in which incubation, separation, and PCR can be performed.

With that project many of the other areas of improvement also become important, like transferring the fabrication process to SU8, where work on PCR is extensive, and optimizing mixing efficiency in the incubation channel etc.

Appendix A

Fabrication recipe with notes

In this appendix the recipe used in the fabrication of my systems is presented along with the notes made during the fabrication.

On the first page specifics is given of the machines and other equipment used during fabrication.

In the next three pages the first part of the fabrication sequence, which is performed in the cleanroom, is presented. In this part of the fabrication, all three wafers presented in this thesis had the same treatment. After seed layer deposition the wafers were investigated using DEKTAK. It turned out that the ridges were approximately 30 μm high and the channels around 80 μm deep.

On the fifth page the fabrication sequence for the electroplating performed on IPL is presented. The notes for the three different wafers presented in this thesis are included. The wafer processed first was W3. W5 was processed before W4. The same current density was used, but extra iron was added to the bath before the electroplating of W4.
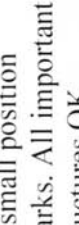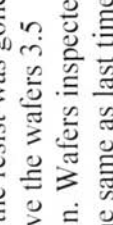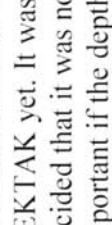
After electroplating of permalloy the wafers were investigated using DEKTAK. For all wafers the thickness of the permalloy was changing a lot at different places. Generally the thickness was between 15 μm and 25 μm along the rim of the wafer and on the wide conducting paths. On the chips the thickness was around 30 μm to 50 μm close to the channels, and 20 μm to 30 μm further away from the channels. Composition measurements was also performed using SEM. The most important results are given in Chap. 8.

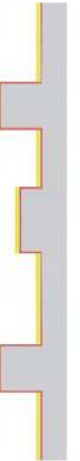On the sixth page the last part of the fabrication consisting of dicing and bonding is presented. W3 went through a special treatment in this part of the fabrication. I first tried to bond the wafer without dicing the chip area out. This turned out to be impossible because of the curvature of the wafer. Some of the chips were diced out and bonded subsequently, but the bonding was not so good. This was because of dirty surface, since it was not protected by the oxide during dicing.

- **Spin-on of resist**
  SSI spin coating and baking track
  Track 1: AZ 5214 positive resist (thin resist)
  Track 2: AZ 4562 positive resist (thick resist)
- **HMDS-treatment**
  Imtec Star 2000, recipe 4, 32.5 min
- **EV-alligner**
  Electro Vision Contact Alligner
  Hard contact mode: 1/10 N, light integration on
- **Deep reactive ion etching**
  Advanced Silicon Etcher: STS MESC Multiplex ICP serial no. 30343
  Standard "Deepetch" from manual:
  http://labmanager.danchip.dtu.dk/upload/3.2_Manual_ASE_UK_20050217.pdf
  Etch cycle: Etch: 8 s, 230 sccm SF_6, 23 sccm O_2. Passivation: 6s, 120 sccm C_4F_8
- **Seed layer deposition**
  Alcatel SCM 600 E-beam metal deposition system
- **Dektak**
  Dektak 8 stylus profiler
- **Au etch**
  Entreat 25g/L, old solution, etch rate not as high as expected
- **Electroplating of permalloy**
  Patented process: United States Patent: 6,036,833
  NiFe bath: 0.200 M $NiSO_4$, 0.200 M $NiCl_2$, 0.500 M H_3BO_3
  0.0070 M NTS, 0.026 M $FeSO_4$, 0.0035 M $FeCl_2$, 0.035 M 5-sulfolsalicylsyre
  0.060 M NaOH. Iron is consumed during electroplating, so bath content changes
  0.100 M $FeSO_4$ added between electroplating of wafer5 and wafer4
  Electroplating cycle: 60 ms: 2×average current density×area
  20 ms: −3×average current density×area
  Electroplating area calculated as 36 cm^2. Probably closer to 45 cm^2
- **Electroplating of Cu**
  Cu Bath (IPL), Current: 0.9 A

Table A.1: Description of equipment and solutions used in the fabrication process

Process Step	Description	Notes	Comments
	Starting wafers: 25 Single Polished Si Wafer OP88, Resistivity 1-20 Ohm cm.		
	Grow 1200 nm thermal oxide: Oven 1100°C: Time + 200 min	Measure oxide thickness with Spectrometer	1100 nm oxide
	5 wafers HMDS treatment: program 4, 30 min		
	Spin-on of 1500 nm AZ5214 positive resist. Track 1, recipe: pr1_5.	Remember test wafers Air Humidity: 45.6 Temperature: 22.1	3 test wafers
	Pattern transfer for trenches and magnetic elements: Exposure: EV-aligner: Exposure time 9 s. Development: Developer AZ531B (Check if new is necessary) for 60 s.	Air Humidity: 45.6 Temperature: 22.1	Inspected wafers. Important structures OK. Maybe a little resist left in small position marks.
	Etching SiO2: Buffered HydroFluoric acid for 15 minutes (etching rate 70-100) nm/min. DI-water with bubbles for 5 minutes Dry wafers	Etch time: 13 min Is the wafer hydrophobic? Then the SiO_2 is gone.	

Process Step	Description	Notes	Comments
	Strip Resist: First acetone bath 1 min. Second acetone bath 2 min. DI-water with bubbles 2 min. Dry wafers	Inspect wafers afterwards. Does it look right.	A little bit of oxide left in small position marks. All important structures OK
	HMDS-treatment Program 4: 30 min.		
	Spin-on of 6200 nm positive photo resist AZ4562: Track 2. Recipe PR_6_2	Remember test wafers Air Humidity: 44.4 Temperature: 21.9	3 test wafers
	Pattern transfer for channels and magnetic elements: Exposure: EV-aligner: Exposure time 60 s. Development: Developer AZ531B (Check if new is necessary) for 4 min.	Air Humidity: 44.4 Temperature: 21.9	After 2.5 min. it looked as the resist was gone. I gave the wafers 3.5 min. Wafers inspected. The same as last time.
	Deep Reactive Ion Etch: 40 mu Recipe: TLO_DEEP	From tests with old mask a number of 33 etch cycles was calculated.	Was not allowed to use DEKTAK yet. It was decided that it was not important if the depth was exactly 40 mu.

Process Step	Description	Notes	Comments
	Strip Resist: First acetone bath 2. min. Second acetone bath 6 min. DI-water with bubbles 2 min. Dry wafers	Inspect wafers afterwards.	Wafers inspected. The oxide looked weird. Especially in the rim of the wafer. It was a little white.
	Deep Reactive Ion Etch: 60 mu Recipe: TLO_DEEP	From tests with old mask a number of 50 cycles was calculated.	Still not allowed to use DEKTAK.
	Etch SiO_2: Buffered HydroFluoric acid for 10 minutes DI-water with bubbles for 5 minutes Dry wafers	Time in BHF: $7.5 + 3$ min. Inspect wafers afterwards.	Wafers inspected. All important structures looked OK.
	Grow oxide (wet oxidation 1000°C): RCA clean: $50 + 40$ min Oven 120 min. + 10min (~100 nm)	Measure oxide thickness with Spectrometer	120 nm oxide
	Seed-layer Deposition: Alcatel: 5 nm Ti and 200 nm Au	Inspect wafers afterwards.	Wafers looked OK

Process Step	Description	Notes	Comments
	Etch Au: Submerge in Entreat until large resistance from bottom to top.	Time: 50 s. Resistance at end time: Generally > 20 MOhm	Resistance was less on some test structures.
	Electroplate Cu: Current density 2.5 A/dm^2. Growth rate 0.5 i m/min.	Plating time: W3 and W4: 5.5 min. W5: 6 min.	On W3 and W5 a little Cu was present on some structures, and was removed by short Cu etch.
	Strip Au: Submerge in Entreat until all gold is etched away.	Etch time: W3: 18 min. W4: 14 min. W5: 12 min.	The etch is very uneven. It takes a lot longer to remove the Au in some places than in other.
	Strip Cu:	Etch time: W3 and W5: long time W4 skipped	Something weird happened tp W3 and W5 and the Cu was difficult to remove. On W4 the Cu was nice, and the step was skipped.
	Electroplate Ni$_x$Fe$_{1-x}$: Average current density: W3: 2 A/dm^2. W4 and W5: 1.5 A/dm^2	Plating time: W3: 97 min W4: 127 min. W5: 140 min.	Successfull electroplating for all three wafers. Only little overplating in some places. Iron content in bath changed between W5 and W4.

Process Step	Description	Notes	Comments
	Inspect in microscope, Dektak, and SEM (Scanning Electron Microscope) to characterize the chips.		Results are summarized in the start of the appendix.
	Dicing of chip area		
	Preparation of Glass Wafers: Wash Glass Wafers in sonic bath with Triton X100 and water. Clean Wafers in 7up or piranha	10 min. in sonic bath.	
	Preparation silicon wafer: BHF 2 min to etch SiO_2. DI-water 2 min. DI-water with bubbles 5 min. Dry wafers	15 min. BHF	
	Sealing of Channels: Anodic Bonding	Bonding parameters	800 V
	Dicing of Chips		

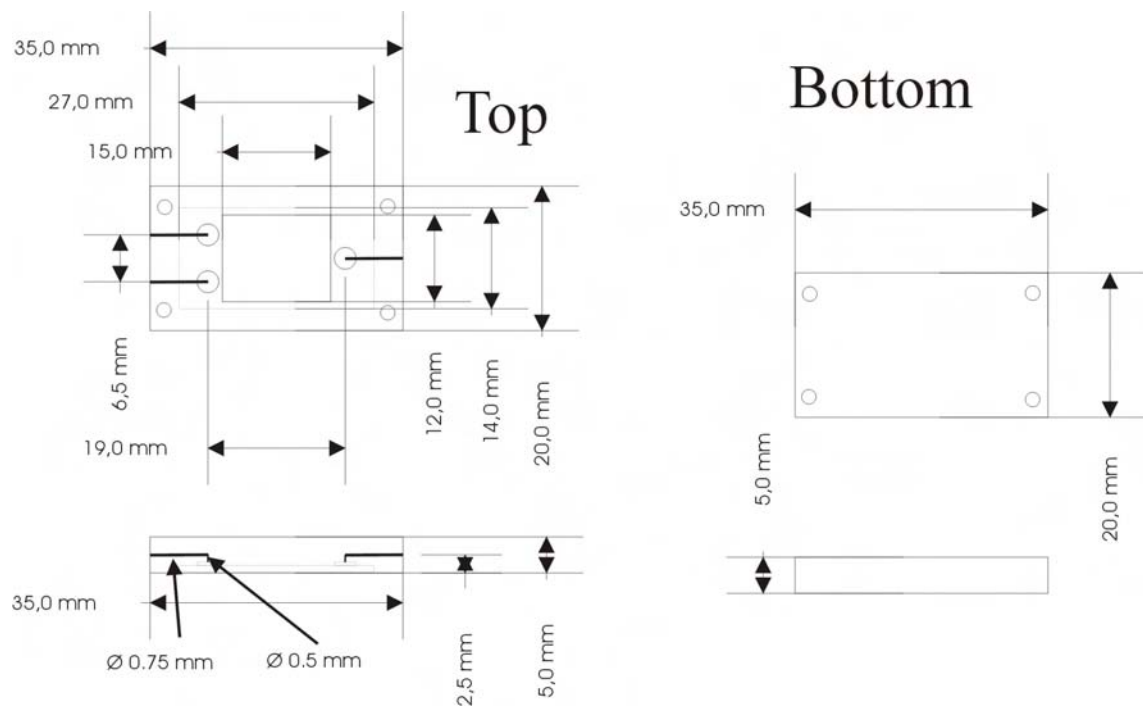# Appendix B

Workshop drawing of chipholder

Figure B.1: *Drawing of the chipholder with two inlets. Delivered to the workshop at MIC for fabrication in PC.*

Bibliography

[1] From a presentation made by Mikkel F. Hansen.

[2] For an overview of bead manufacturers see http://www.magneticmicrosphere.com.

[3] http://www.spherotech.com.

[4] Delta Mask, Tankelanden 3, 7542 DR Enschede, The Netherlands, www.deltamask.nl/.

[5] Personal communication, Yvonne Gyrsting, lab technician, Danchip, Tecnical University of Denmark.

[6] http://www.theleeco.com.

[7] C. H. Ahn and M. G. Allen. A fully integrated micromachined magnetic particle manipulator and separator. In *Proceedings IEEE Micro Electro Mechanical Systems An Investigation of Micro Structures, Sensors, Actuators, Machines and Robotic Systems*, pages 91–96. IEEE, 1994.

[8] C. H. Ahn, M. G. Allen, W. Trimmer, Y.-N. Jun, and S. Erramilli. A fully integrated micromachined magnetic particle separator. *J. Microelectromech. Syst.*, 5:151–158, 1996.

[9] Armand Ajdari. Transverse electrokinetic and microfluidic effects in micro-patterned channels: lubrication analysis for slab geometries. *Phys. Rev. E*, 65:016301, 2002.

[10] J. Aubin, D. F. Fletcher, J. Bertrand, and C. Xuereb. Characterization of mixing quality in micromixers. *Chem. Eng. Technol.*, 26:1262–1270, 2003.

[11] R. M. Bozorth. *Ferromagnetism*, volume 1. John Wiley & sons, inc., Hoboken, New Jersey, 2003.

[12] H. Bruus. *Lecture notes, Theoretical microfluidics*. DTU (MIC), 2004.

[13] J.-W. Choi, C. H. Ahn, S. Bhansali, and H. T. Henderson. A new magnetic bead-based, filterless bio-separator with planar electromagnet surfaces for integrated bio-detection systems. *Sens. Actuators B*, 68:34–39, 2000.

[14] J.-W. Choi, T. M. Liakopoulos, and C. H. Ahn. An on-chip magnetic bead separator using spiral electromagnets with semi-encapsulated permalloy. *Biosens. Bioelectron.*, 16:409–416, 2001.

[15] J.-W. Choi, K. W. Oh, A. Han, C. A. Wijayawardhana, C. Lannes, S. Bhansali, K. T. Schlueter, W. R. Heineman, H. B. Halsall, J. H. Nevin, A. J. Helmicki, H. T. Henderson, and C. H. Ahn. Development and characterization of microfluidic devices and systems for magnetic bead-based biochemical detection. *Biomedical Microdevices*, 3:191–200, 2001.

[16] J.-W. Choi, K. W. Oh, J. H. Thomas, W. R. Heineman, H. B. Halsall, J. H. Nevin, A. J. Helmicki, H. T. Henderson, and C. H. Ahn. An integrated microfluidic biochemical detection system for protein analysis with magnetic bead-based sampling capabilities. *Lab Chip*, 2:27–30, 2002.

[17] T. Deng, M. Prentiss, and G. M. Whitesides. Fabrication of magnetic microfiltration systems using soft lithography. *Appl. Phys. Lett.*, 80:461–463, 2002.

[18] J. Do, J.-W. Choi, and C. H. Ahn. Low-cost magnetic interdigitated array on a plastic wafer. *IEEE Trans. Magn.*, 40:3009–3011, 2004.

[19] L. Ejsing, M. F. Hansen, A. K. Menon, H. A. Ferreira, D. L. Graham, and P. P. Freitas. Planar hall effect sensor for magnetic micro- and nanobead detection. *Appl. Phys. Lett.*, 84:4729–4731, 2004.

[20] Z. H. Fan, S. Mangru, R. Granzow, P. Heaney, W. Ho, Q. Dong, and R. Kumar. Dynamic dna hybridization on a chip using paramagnetic beads. *Anal. Chem.*, 71:4851–4859, 1999.

[21] G. Fonnum, C. Johansson, A. Molteberg, S. Mørup, and Elin Aksnes. Characterisation of dynabeads by magnetization measurements and mössbauer spectroscopy. *J. Magn. Magn. Mater.*, in print, 2005.

[22] C. B. Fuh, J.Z. Lai, and C. M. Chang. Particle magnetic susceptibility determination using analytical split-flow thin fractionation. *J. Chromatogr. A*, 923:263–270, 2001.

[23] S. Fukui, Y. Takahashi, M. Yamaguchi, T. Sato, H. Imaizumi, M. Oizumi, S. Nishijima, and T. Watanabe. Study on open gradient magnetic separation using superconducting solenoid magnet. *IEEE Trans. Magnetics.*, 14:1568–1571, 2004.

[24] D. J. Griffiths. *Introduction to Electrodynamics.* Prentice Hall, New Jersey, 3rd edition, 1999.

[25] M. F. Hansen. *Notes, Magnetism and magnetic materials.* DTU (MIC), 2005.

[26] A. M. Hynes, H. Asraf, J. K. Bhardwaj, J. Hopkins, I. Johnston, and J. N. Shepherd. Recent advances in silicon etching for mems using the ase^{TM} process. *Sens. Actuators*, 74:13–17, 1999.

[27] D. Jiles. *Introducion to Magnetism and Magnetic Materials.* CRC Press LLC, New York, 2nd edition, 1998.

[28] T. J. Johnson and L. E. Locascio. Characterization and optimization of slanted well designs for microfluidic mixing under electroosmotic flow. *Lab on a chip*, 2:135–140, 2002.

[29] T. J. Johnson, D. Ross, and L. E. Locascio. Rapid microfluidic mixing. *Anal. Chem.*, 74:45–51, 2002.

[30] T. G. Kang and T. H. Kwon. Colored particle tracking method for mixing analysis of chaotic micromixers. *J. Micromech. Microeng.*, 14:891–899, 2004.

[31] D. S. Kim, S. W. Lee, T. H. Kwon, and S. S. Lee. A barrier embedded chaotic micromixer. *J. Micromech. Microeng.*, 14:798–805, 2004.

[32] T. M. Liakopoulos, J.-W. Choi, and C. H. Ahn. A bio-magnetic bead separator on glass chips using semi-encapsulated spiral electromagnets. In *Proceedings of International Solid State Sensors and Actuators Conference (Transducers '97)*, pages 485–488. IEEE, 1997.

[33] M. Madou. *Fundamentals of microfabrication*, volume 1. CRC Press, Boca Raton, 1997.

[34] G. S. May and S. M. Sze. *Fundamentals of semiconductor fabrication*, volume 1. Wiley, New York, 2004.

[35] L. R. Moore, A. R. Rodriguez, P. S. Williams, K. McKloskey, J. J. Bolwell, M. Nakamura, J. J. Chalmers, and M. Zborowski. Progenitor cell isolation with a high-capacity quadropole magnetic sorter. *J. Magn. Magn. Mater.*, 225:277–284, 2001.

[36] N-T Nguyen and Z. Wu. Micromixers-a review. *Eur. Phys. J. E*, 9:387–399, 2002.

[37] R. C. O'Handley. *Modern Magnetic Materials. Principles and applications.* John Wiley and Sons, Inc., New York, 5th edition, 1999.

[38] Q. A. Pankhurst, J. Connolly, S. K. Jones, and J. Dobson. Applications of magnetic nanoparticles in biomedicine. *J. Phys. D: Appl. Phys.*, 36:R167–R181, 2003.

[39] J. D. Plummer, M. D. Deal, and P. B. Griffin. *Silicon VLSI technology*, volume 1. Prentice Hall, Upper saddle river, NJ 07458, 2000.

[40] Q. Ramadana, V. Samperb, D. Poenara, and C. Yub. On-chip micro-electromagnets for magnetic-based bio-molecules separation. *J. Magn. Magn. Mater.*, 281:150–172, 2004.

[41] R. Rong, J. W. Choi, and C. H. Ahn. A functional magnetic bead/biocell sorter using fully integrated magnetic micro/nano tips. In *Proceedings IEEE Sixteenth Annual International Conference on Micro Electro Mechanical Systems*, pages 530–533. IEEE, 2003.

[42] R. Rong, J. W. Choi, and C. H. Ahn. A novel magnetic chaotic mixer for in-flow mixing of magnetic beads. In *7th International Conference on Miniaturized Chemical and Blochemlcal Analysts Systems*, pages 335–338. IEEE, 2003.

[43] K. Smistrup. *M. Sc. E. thesis, Integrated micromachined magnetic bead separator.* DTU (MIC), 2003.

[44] K. Smistrup, O. Hansen, P. T. Tang, and M. F. Hansen. Selective magnetic bead capture using an adressable on-chip electromagnet array. In *Micro Total Analysis Systems 2004*, pages 509–511. The royal society of chemistry, 2004.

[45] A. D. Stroock, S. K. W. Dertinger, A. Ajdari, I. Mezic, H. A. Stone, and G. M. Whitesides. Chaotic mixer for microchannels. *Science*, 295:647–651, 2002.

[46] Abraham D. Stroock, Stephan K. Dertinger, George M. Whitesides, and Armand Ajdari. Patterning flows using grooved surfaces. *Anal. Chem.*, 74:5306–5312, 2002.

[47] E. Svensson. *Thesis for the degree of licentiate of engeneering, From Eulerian to Lagrangian Viewpoints in Fluid Flows.* Chalmers, 2003.

[48] P. T. Tang. *Ph. D. thesis, Fabrication of Micro Components by Electrical Deposition.* DTU (IPL), 1998.

[49] M. Tondra, M. Granger, R. Fuerst, M. Porter, C. Nordman, J. Taylor, and S. Akou. Design of integrated microfluidic device for sorting magnetic beads in biological assays. *IEEE Trans. Magn.*, 37:2621–2623, 2001.

[50] W. Zhang and C. H. Ahn. A microfabricated planar magnetic particle separator with optically inspectable flow channel. In *Engineering in Medicine and Biology Society, 1996. Bridging Disciplines for Biomedicine., 18th Annual International Conference of the IEEE*, pages 252–253. IEEE, 1997.

[51] Y. Zhu and S. Granick. Limits of the hydrodynamic no-slip boundary conditions. *Phys. Rev. Lett.*, 88:106102–1–106102–4, 2002.